COMILLAS
UNIVERSIDAD PONTIFICIA
ICAI

MÁSTER UNIVERSITARIO EN INGENIERÍA INDUSTRIAL

TRABAJO FIN DE MÁSTER

Impact of viscous stress relaxation on the residual stress of a W-Cu joint component designed for the high-heat-flux targets of a nuclear fusion reactor

Autor: Fernando Oleo Blanco

Director: Jeong-Ha You

Madrid

Agosto de 2022

Declaro, bajo mi responsabilidad, que el Proyecto presentado con el título

Impact of viscous stress relaxation on the residual stress of a W-Cu joint component designed for the high-heat-flux targets of a nuclear fusion reactor

en la ETS de Ingeniería - ICAI de la Universidad Pontificia Comillas en el curso académico 2021-22 es de mi autoría, original e inédito y no ha sido presentado con anterioridad a otros efectos. El Proyecto no es plagio de otro, ni total ni parcialmente y la información que ha sido tomada de otros documentos está debidamente referenciada.

Fdo.: Fernando Oleo Blanco Fecha: 12/ 08/ 2022

Autorizada la entrega del proyecto

EL DIRECTOR DEL PROYECTO

Fdo.: Jeong-Ha You Fecha: 12/ 08/ 2022

J.H. You

COMILLAS
UNIVERSIDAD PONTIFICIA
ICAI

MÁSTER UNIVERSITARIO EN INGENIERÍA INDUSTRIAL

TRABAJO FIN DE MÁSTER

Impact of viscous stress relaxation on the residual stress of a W-Cu joint component designed for the high-heat-flux targets of a nuclear fusion reactor

Autor: Fernando Oleo Blanco

Director: Jeong-Ha You

Madrid

Agosto de 2022

IMPACTO DE LA FLUENCIA EN LA RELAJACIÓN DE ESTRESES RESIDUALES DE UN COMPONENTE UNIDO W-CU DISEÑADO PARA EL ESCUDO DE ALTA POTENCIA DE UN REACTOR NUCLEAR DE FUSIÓN

Autor: Oleo Blanco, Fernando.

Director: You, Jeong-Ha.

Entidad Colaboradora: Max-Planck Institute für Plasmaphysik.

RESUMEN DEL PROYECTO

Introducción

El diseño actual del escudo del divertor propuesto para ITER-DEMO está compuesto por una armadura de tungsteno, la tubería de refrigeración de CuCrZr y una capa intermedia entre las dos partes de OFHC-Cu; indicado en la Figura 1.

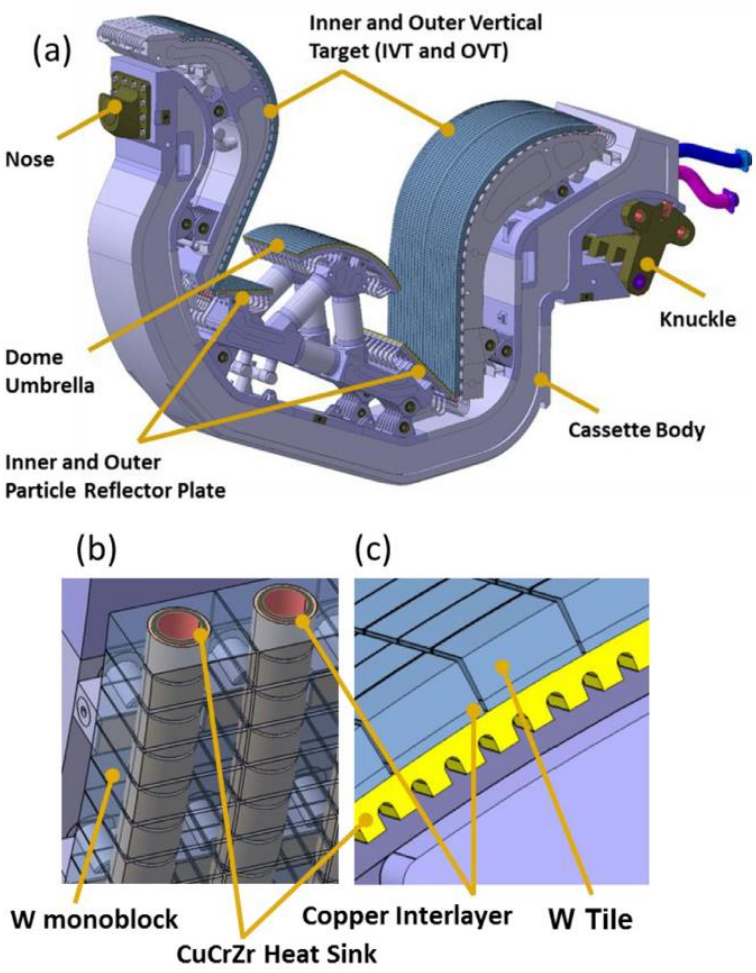

Figura 1: Visualización esquemática del divertor de ITER. Imagen tomada de Takeshi Hirai et al. 'Use of tungsten material for the ITER divertor'.

El escudo será producido por el método HRP (Hot Radial Pressing), el cual utiliza altas temperaturas (580 ºC) y altas presiones (hasta 60 MPa) para unir los distintos materiales. El historial de temperaturas y presiones del proceso está indicado en la Figura 2.

Debido a la notable diferencia en las propiedades termomecánicas de los materiales, ver Tabla 1, y el gran transitorio térmico que tiene lugar durante HRP, hay una generación de estreses residuales en el escudo.

Estudios anteriores (1, 2) analizaron el aumento de estreses durante el proceso de HRP con modelos elasto-plásticos, mientras que los efectos viscosos se trataron de forma puntual. Li (2) analizó el impacto de los estreses residuales usando dos casos extremos:

1) El escudo se encuentra en un estado libre de estreses a temperatura ambiente. Este caso suele ser el más común para análisis sencillos y directos.
2) El escudo se encuentra en un estado libre de estreses al principio del enfriamiento durante la fabricación, indicado en la Figura 2 a las 18h, que corresponde a 580 ºC. Este caso representa el aumento más severo del incremento de estreses.

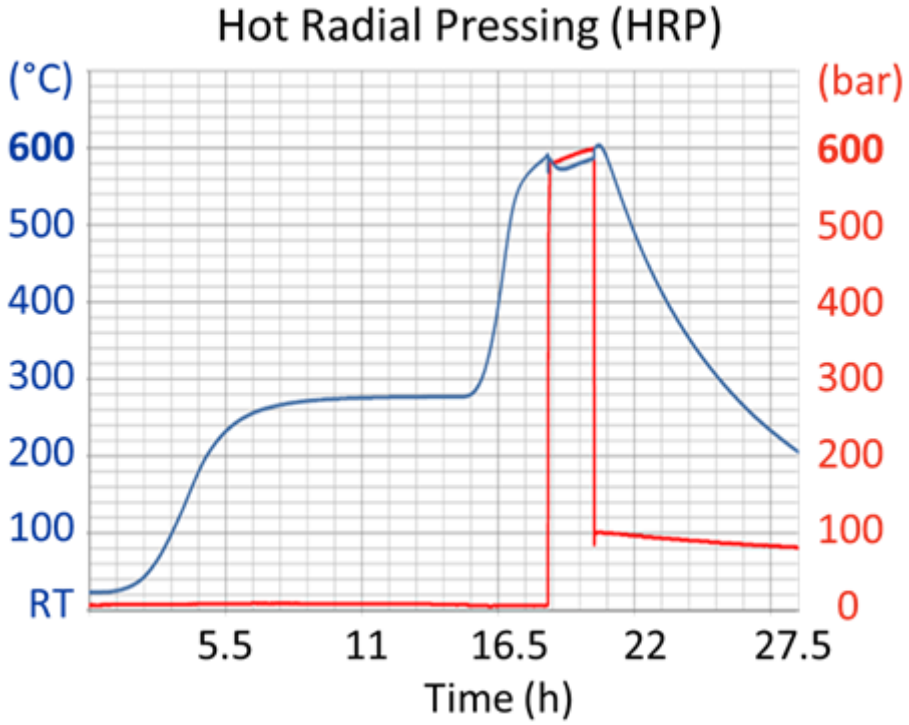

Figura 2: Evolución de la temperatura y de la presión durante el proceso HRP. Información proporcionada por el fabricante (ENEA).

Material	E [GPa]		α [K^{-1}]		λ [$W\,K^{-1}\,m^{-1}$]		σ_Y [MPa]	
	297 K	873 K	297 K	873 K	297 K	873 K	297 K	873 K
W	398	387	4.5×10^{-6}	4.72×10^{-6}	173	128	1350	764
OFHC-Cu[a]	117	81.3	1.68×10^{-5}	1.88×10^{-5}	401	360	3	3
CuCrZr	127.5	95	1.67×10^{-5}	1.86×10^{-5}	218	346	280	190[b]

[a] The yield stress for the material has been set to 3 MPa since casted copper is a very soft material that mostly behaves plasticly.
[b] At 350 °C.

Tabla 1: Selección de propiedades mecánicas de los materiales del divertor en función de la temperatura.

Los resultados de ambas suposiciones se presentan en la Figura 3. Dependiendo de la temperatura seleccionada, el escudo puede invertir su historial de estreses durante la operación del reactor. Esto indica que hay una gran incertidumbre del estado de la pieza dependiendo del caso seleccionado.

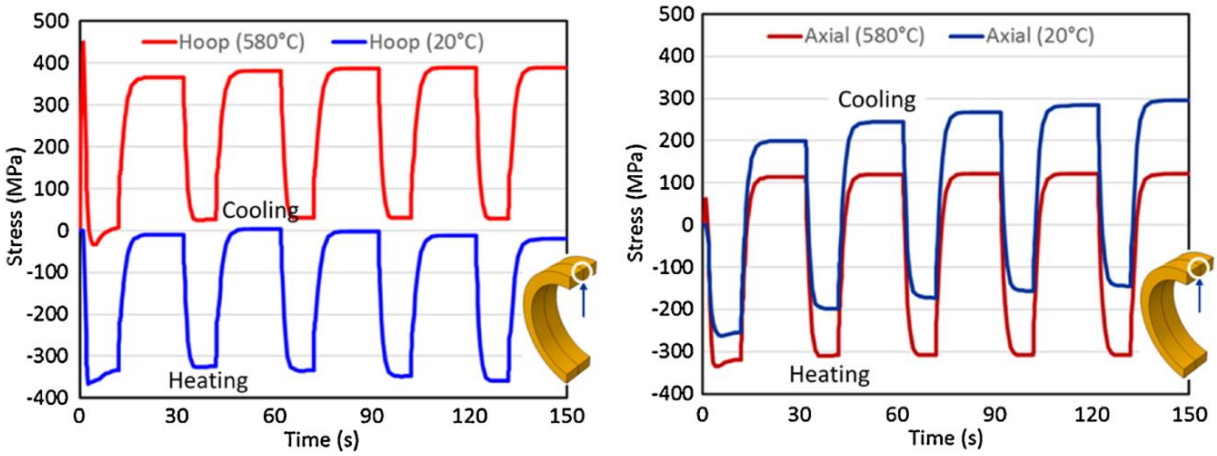

Figura 3: Diferencia de estreses entre los dos casos límites de la temperatura libre de estreses: 580 ºC y 20 ºC. Los estreses se seleccionan en el punto central más cercano al plasma del tubo de refrigeración. Imagen tomada de (1).

Introducción a la viscoplasticidad

Los efectos viscoplásticos se refieren al fuljo plástico (deformación permanente) que los materiales sufren cuando están bajo estreses. La viscoplasticidad se suele estudiar en aplicaciones de alta temperatura y altos estreses, ya que el flujo es muy dependiente de estos dos parámetros. La Figura 4 resume el impacto de la fluencia en el material.

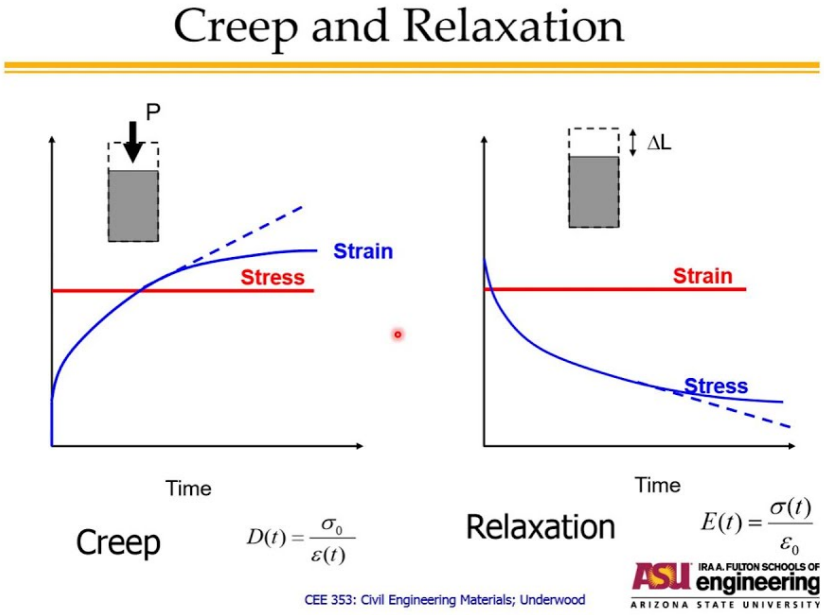

Figure 4: Relajación por fluencia en función de los estreses (izquierda) o por deformación (derecha). Imagen tomada de Arizona State University (ASU), course CEE 353.

Durante el proceso de fabricación por HRP, la temperatura es suficientemente alta para que haya fluencia en OFHC-Cu y CuCrZr. El trabajo actual se fija en mejorar la incertidumbre

indicada por Li (2) centrándose en la adición de la fluencia para la predicción de los estreses residuales durante HRP. Este enfoque debería predecir estreses que están entre las dos suposiciones de temperatura libre de estreses presentadas anteriormente al mejorar los modelos físicos de los materiales.

Metodología

Para entender el aumento de estreses residuales durante el proceso HRP, el enfriamiento de la armadura es analizado mediante la técnica de elementos finitos (FEM). Dos casos fueron simulados, en uno la fluencia del material no se tuvo en cuenta, mientras que en el segundo sí. Este método permite comparar directamente el impacto de la fluencia.

Preparación FEM

El modelo FEM explota la simetría del bloque, por lo que solo un cuarto de la geometría es simulada. La descripción del modelo, del mallado y de las condiciones de contorno del problema se indican a continuación.

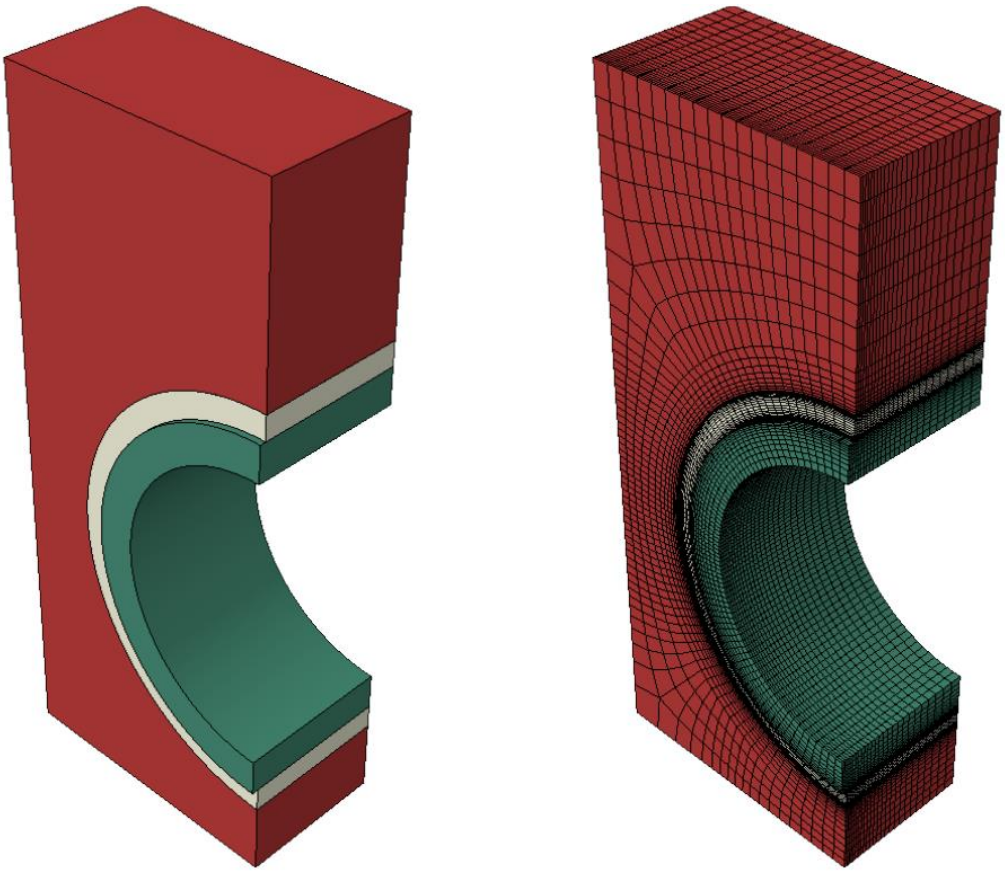

(a) Divertor monoblock, FEM distribution of the materials. Tungsten in red, OFHC-Cu in beige, CuCrZr-IG in green.

(b) Overview of FEM mesh used for the final analysis.

Figura 5: Cuarto de modelo usado en la simulación.

El descenso de la temperatura que tiene lugar durante HRP se da como dato de entrada en todo el dominio ya que se asume una temperatura homogénea en toda la parte. El enfriamiento es definido con dos funciones:

1) Enfriamiento exponencial hasta los 76 ºC. Este modelo fue seleccionado para modelar de forma precisa el enfriamiento de HRP.
2) Ya que el efecto de la fluencia a temperaturas bajas es despreciable, se define un enfriamiento linear desde 76 ºC hasta 20 ºC en un periodo corto. Esto permite acelerar la simulación.

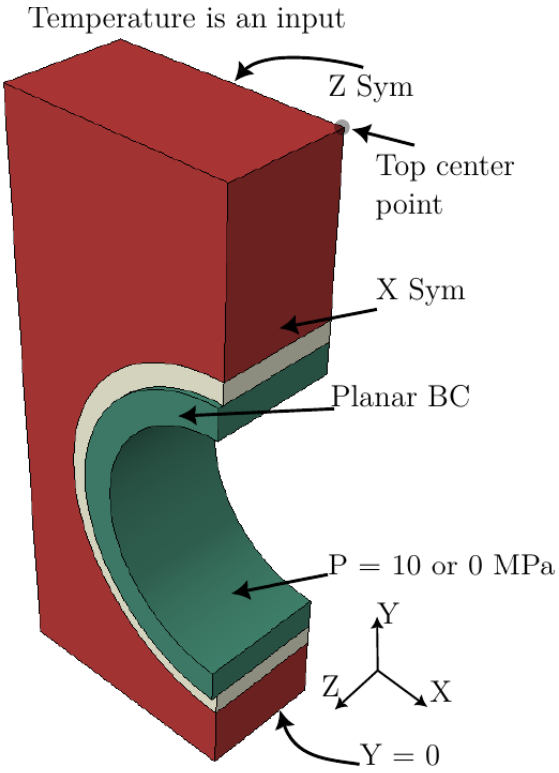

Figura 6: Definición de condiciones de contorno.

	Pressure increase	Exponential drop of temperature	Rapid drop of temperature	Cutting of cooling pipe	Cutting of the part
Duration	10 s	55 000 s	1000 s	1 s	1 s
Temperature	580 °C	580 to 76 °C	76 to 20 °C	20 °C	20 °C
HRP pressure	0 to 10 MPa	10 MPa	10 to 0 MPa	—	—
Tie constrains	✓	✓	✓	✓	✓
X Symmetry plane	✓	✓	✓	✓	✓
Z Symmetry plane	✓	✓	✓	✓	✓
Y = 0 bottom plane	✓	✓	✓	✓	—
Planar BC	✓	✓	✓	—	—
Vertical fix of top and bottom center point	—	—	—	—	✓

Tabla 2: Secuencia de etapas y sus condiciones de contorno.

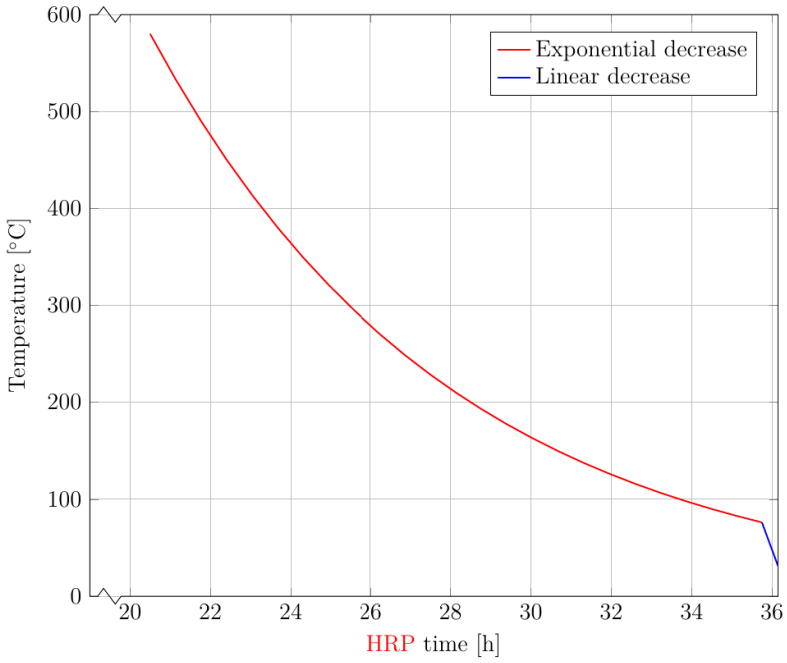

Figura 7: Definición del perfil de enfriamiento.

Varias piezas son producidas a la vez, todas conectadas a la misma tubería. Por lo tanto, la condición de planitud/Bernoulli es aplicada a la cara de en medio entre el espacio de los bloques

Propiedades de los materiales

Las propiedades de los materiales son tomadas del manual de EUROfusion (MPH) (3) con la excepción de la fluencia, ya que no está incluida en el manual y se discute más adelante.

Diseño de la malla

Las tres partes del bloque: escudo de tungsteno, entrecapa de cobre y tubería de CuCrZr fueron malladas de forma independiente. Las mallas fueron ensambladas en un solo cuerpo usando el método de conexión de Abaqus. La malla fue refinada como se indica a continuación.

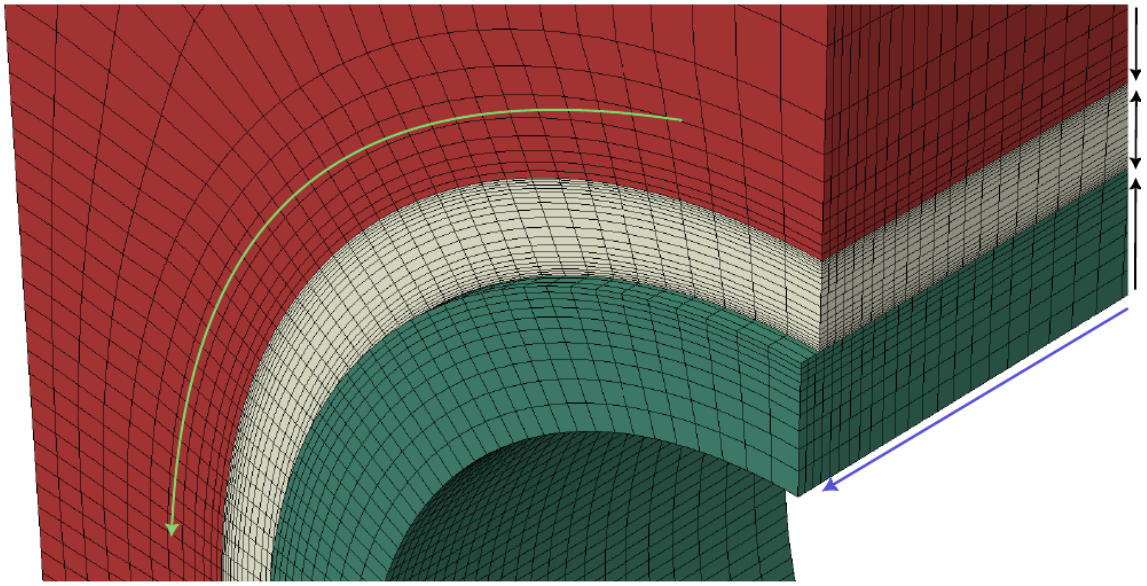

Figura 8: Refinamiento del mallado.

El mallado fue seleccionado después de un análisis de sensibilidad usando tres refinamientos: bruto (143E3 nodos), medio (415E3) y fino (1.52E6). El refinamiento medio obtuvo resultados muy similares al fino y por lo tanto fue seleccionado para el estudio.

Modelado de fluencia

Las propiedades del cobre y sus aleaciones han sido estudiadas durante más de un centenario. Existen estudios avanzados de fluencia desde los 1950s. Li en (4) realizó una compilación de la literatura sobre fluencia en el cobre para una gran selección de aleaciones. No existen modelos de fluencia primaria para OFHC-Cu. Para CuCrZr existe un modelo de fluencia primaria y secundaria. Sin embargo, el rango de validez de temperaturas y estreses no es adecuado para el presente estudio. Con los modelos actualmente disponibles, se tomó la decisión de modelar solo la fluencia secundaria para OFHC-Cu. El modelo sigue la ley de Norton-Bailey, indicada a continuación.

$$\dot{\epsilon}^{cr} = \dot{\epsilon}_{sd} = 38.8 \cdot \tilde{\sigma}^{4.8} \cdot e^{-\frac{197\,000}{\Re \cdot T_{abs}}}$$

$$\frac{\delta \dot{\epsilon}^{cr}}{\delta \tilde{\sigma}} = 38.8 \cdot 4.8 \cdot \tilde{\sigma}^{3.8} \cdot e^{-\frac{197\,000}{\Re \cdot T_{abs}}}$$

$$400\,^{\circ}\mathrm{C} \leq T \leq 700\,^{\circ}\mathrm{C}$$

$$15\,\mathrm{MPa} \leq \tilde{\sigma} \leq 105\,\mathrm{MPa}$$

La ley de fluencia se implementó usando la subrutina CREEP de Abaqus. En el futuro, una vez que se obtengan datos de fluencia primaria, el modelo y la subrutina podrán ser adaptados.

Predicción de estreses residuales en pruebas experimentales

Los resultados obtenidos mediante FEM serán comparados con mediciones experimentales. Sin embargo, para poder ejecutar las mediciones, los bloques de la armadura se tienen que separar primero. Después, debido al espacio limitado en la máquina para FIB-DIC, el bloque ha de ser seccionado en dos.

Las operaciones de corte cambiarán la estructura del bloque lo cual cambiará su estado tensional. Por lo tanto, para interpretar de forma correcta los resultados de las mediciones que se van a realizar, es necesario simular estas operaciones de corte. En el trabajo, se realizó tanto el corte de la tubería de CuCrZr como el seccionamiento de la pieza.

Resultados

Impacto de la fluencia

Comparando los resultados de las simulaciones, con y sin fluencia, resulta que el modelo de fluencia secundaria tiene un impacto mínimo en la reducción de los estreses residuales. Una tercera simulación fue realizada con el exponente de estreses igual a 7, ya que en la literatura se presenta como un límite superior.. Esta nueva simulación no demostró cambio substancial en los resultados. A continuación, se incluyen los resultados obtenidos.

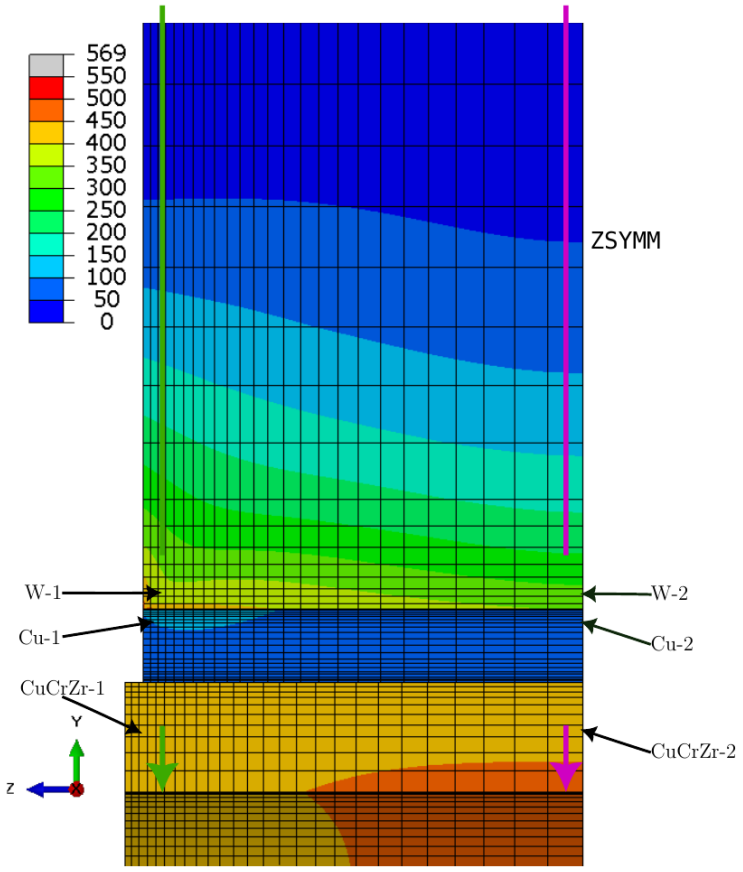

Figura 9: Selección de los perfiles de estreses.

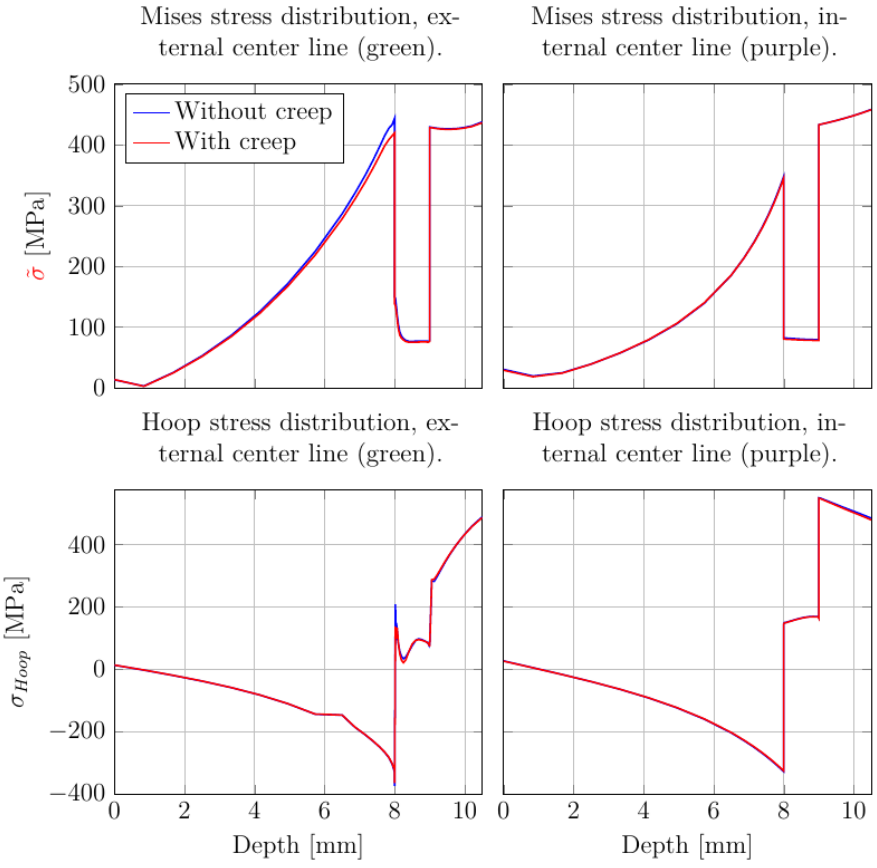

Figura 10: Comparación de distribución de estreses entre el modelo con fluencia y sin.

Cambio de estreses después del seccionamiento

La simulación de los cortes demuestra un cambio substancial en la distribución de estreses.

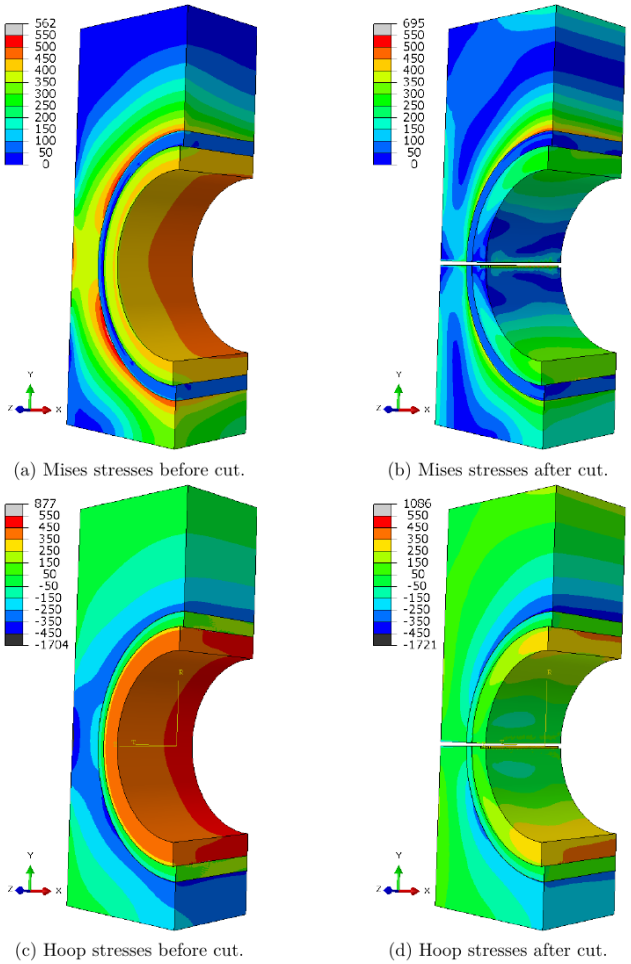

(a) Mises stresses before cut. (b) Mises stresses after cut.

(c) Hoop stresses before cut. (d) Hoop stresses after cut.

Figura 11: Cambio de estreses después del seccionamiento.

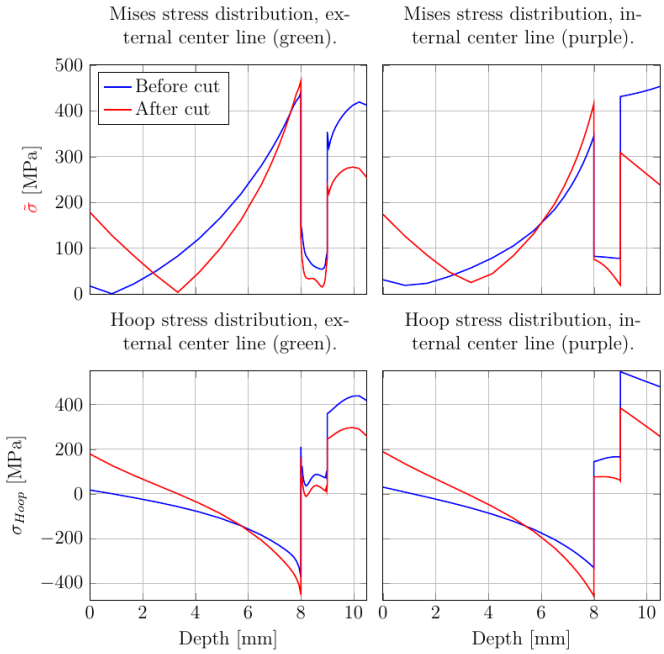

Figura 12: Distribución de estreses antes y después del corte.

La simulación del corte consigue mostrar la evolución y concentración de estreses que tiene lugar durante la operación, como se visualiza a continuación.

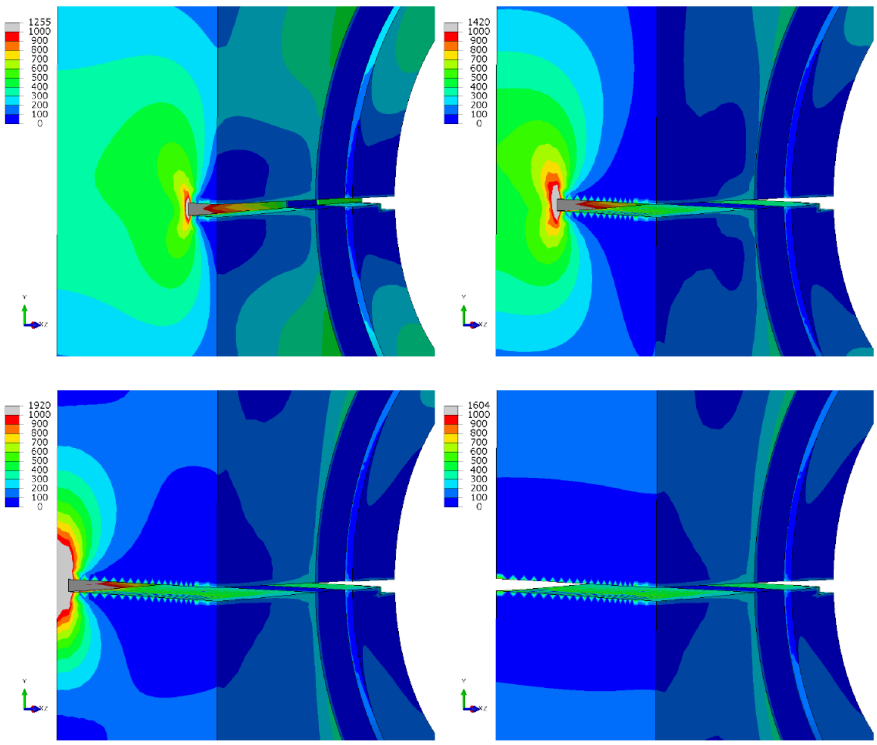

Figura 13: Concentración de estreses durante la operación de corte.

Conclusión

Los resultados obtenidos demuestran que la fluencia, con el modelo seleccionado, no tiene impacto en la reducción de estreses residuales en comparación con la suposición elasto-plástica.

Los resultados de la operación de corte demuestran un cambio substancial en los estreses de la pieza. Esto indica que los resultados de las mediciones experimentales no representan directamente el estado de la pieza después de su producción.

Los resultados obtenidos en este trabajo han servido como referencia para nuevas pruebas de materiales y la interpretación de los resultados experimentales.

IMPACT OF VISCOUS STRESS RELAXATION ON THE RESIDUAL STRESS OF A W-CU JOINT COMPONENT DESIGNED FOR THE HIGH-HEAT-FLUX TARGETS OF A NUCLEAR FUSION REACTOR

Introduction

The current divertor target design proposed for ITER and DEMO makes use of tungsten as the Plasma Facing Material (PFM), CuCrZr for the cooling pipe and OFHC-Cu as the interlayer between the other two materials. The design and material distribution is shown in **Fehler!**

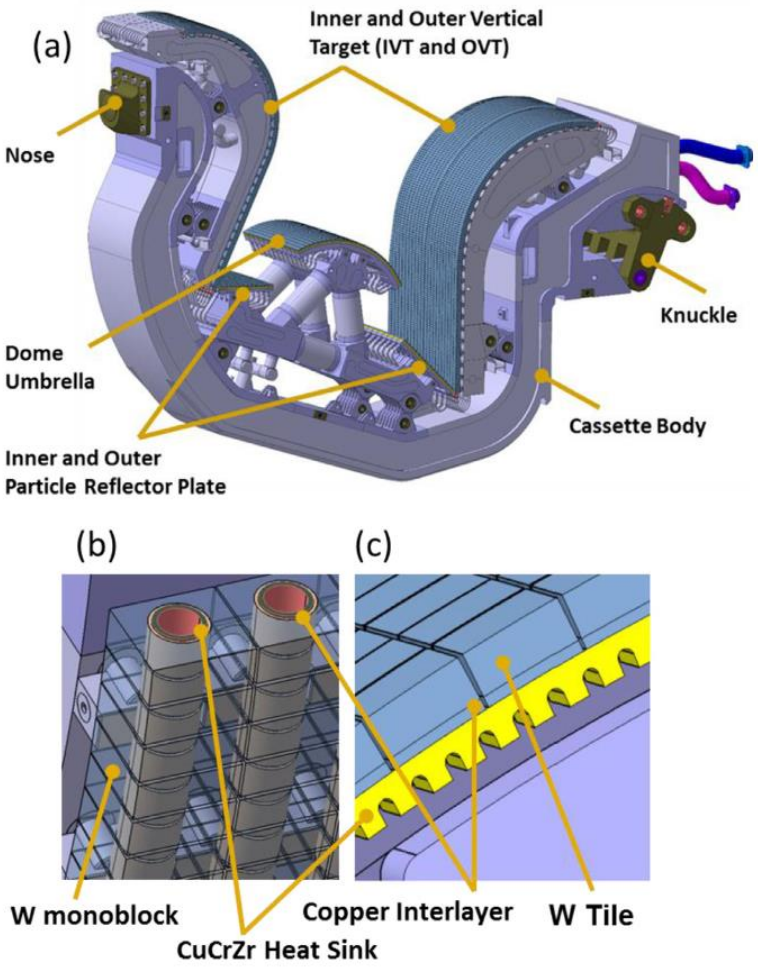

Figure 14: Schematic view of ITER divertor. Figure taken from Takeshi Hirai et al. 'Use of tungsten material for the ITER divertor'

Verweisquelle konnte nicht gefunden werden..

The divertor target shall be produced with the Hot Radial Pressing (HRP) method. The HRP process utilizes high temperatures (580 ºC) and high pressure (up to 60 MPa) to join the different parts. The temperature and pressure histories used in the HRP process are indicated in Figure 15. Due to the substantial differences in thermomechanical properties between the materials, see Table 3, and the large thermal transient that takes place during HRP, residual stresses build up in the divertor monoblock.

Previous studies (1, 2) analysed the residual stress build-up that takes place during HRP under the elasto-plastic assumption, with viscous effects being treated as a special case. Li (2) analysed the impact of residual stresses by taking two extreme cases:

1) The monoblock is in a stress-free-state at room temperature. This case tends to be the most common for simple, direct analysis.
2) The monoblock is in a stress-free-state at the beginning of the cooling period in HRP, shown in Figure 15 at ~18h, which corresponds to 580 ºC. This case represents the most severe build-up of residual stresses.

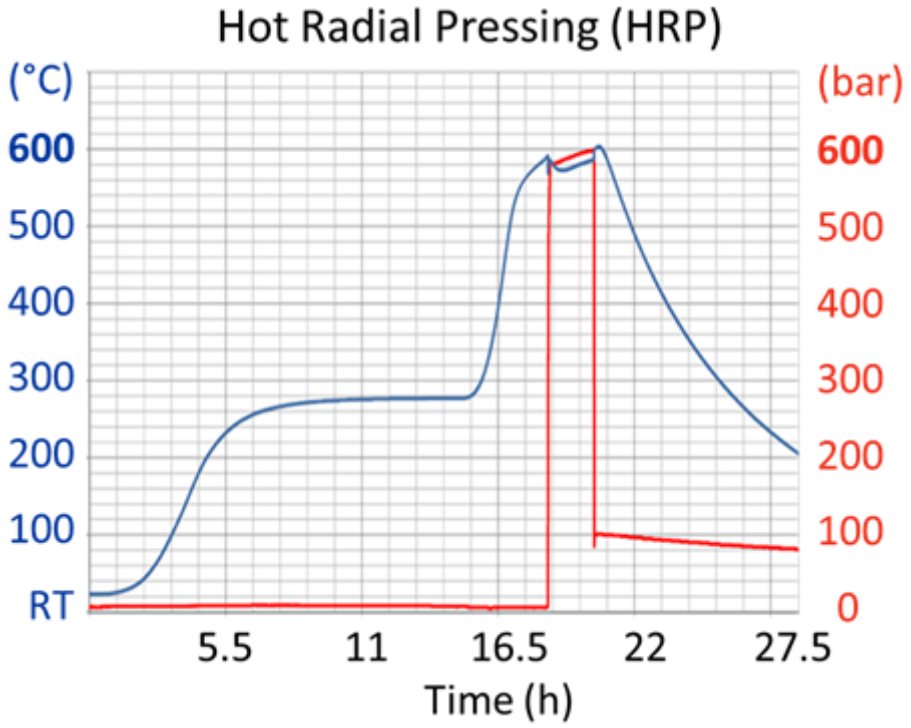

Figure 15: Temperature and pressure evolution during the HRP joining process. Data provided by the manufacturer (ENEA)

Material	E [GPa]		α [K^{-1}]		λ [$W\,K^{-1}\,m^{-1}$]		σ_Y [MPa]	
	297 K	873 K	297 K	873 K	297 K	873 K	297 K	873 K
W	398	387	4.5×10^{-6}	4.72×10^{-6}	173	128	1350	764
OFHC-Cu[a]	117	81.3	1.68×10^{-5}	1.88×10^{-5}	401	360	3	3
CuCrZr	127.5	95	1.67×10^{-5}	1.86×10^{-5}	218	346	280	190[b]

[a] The yield stress for the material has been set to 3 MPa since casted copper is a very soft material that mostly behaves plasticly.
[b] At 350 °C.

Table 3: Selected mechanical properties of the relevant materials as a function of temperature.

The results of both assumptions is shown in Figure 16. Depending on the stress-free-temperature, the divertor monoblock may see an inversed stress history during operation. This indicates that there is a large uncertainty of the state of the part during operation depending on the assumed stress-free-temperature.

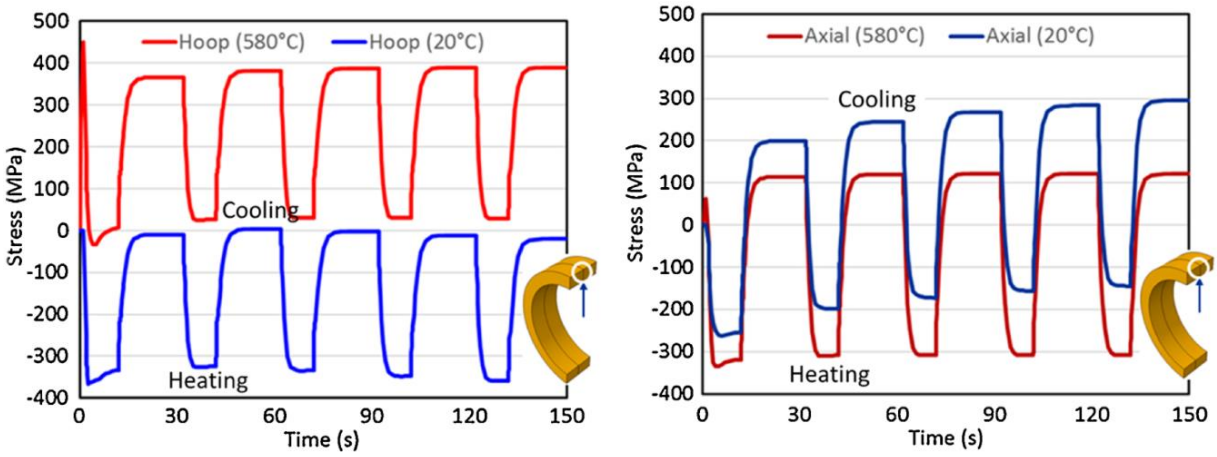

Figure 16: Stress history difference between limiting cases for stress relaxation. The stress is taken from the uppermost position of the pipe for the two limiting cases: null relaxation at 580 °C and perfect relaxation at 20 °C. Image taken from (1).

Introduction to viscoplasticity

Viscoplastic effects refer to the plastic (non-recoverable deformation) flow that materials suffer while stressed. Viscoplasticity tends to be studied in high temperature applications and highly stressed parts, as viscoplasticity is highly dependent on those two parameters. Figure 17 summarizes the impact of creep on the material (another term for viscoplasticity in solids).

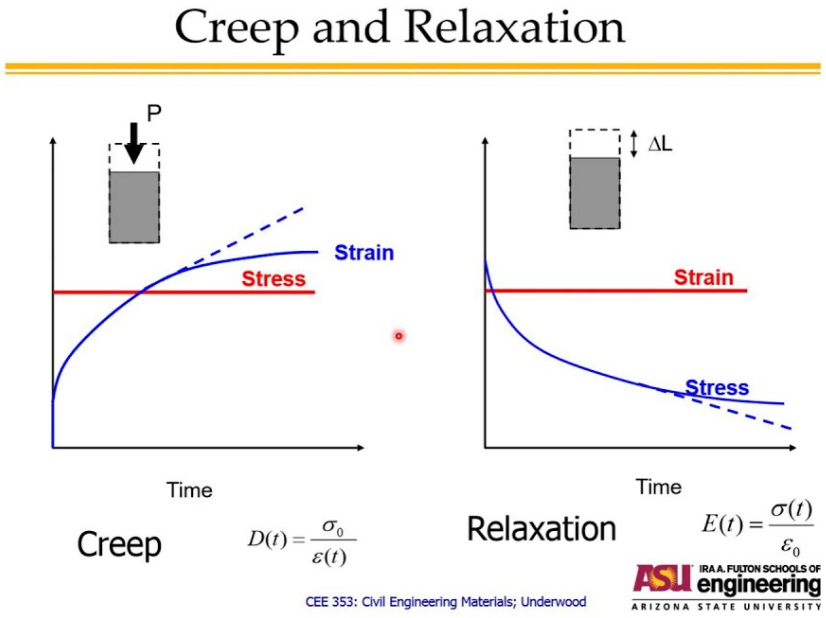

Figure 17: Creep relaxation as a function of stress (left) and as a function of deformation (right). Taken from Arizona State University (ASU), course CEE 353.

During the monoblock's production with HRP, the temperature is high enough that creep is expected to take place for OFHC-Cu and CuCrZr. The present work tackles the uncertainty indicated by Li (2) by focusing on the addition of viscoplastic effects that take place during the cooldown of the part. This approach should yield a result that is between the two stress-free-temperatures presented earlier by providing a more physically accurate material model.

Methodology

In order to understand the residual stress build-up generated by HRP, the cooling of the monoblock is analysed using Finite Elements (FEM). Two simulations are performed, one where creep is taken into account and another without creep. This approach allows the comparison between the two cases and isolates the effect of creep.

FEM setup

The FEM model exploits the symmetry of the monoblock and therefore a quarter model is simulated. An overview of the model, the mesh used and the corresponding boundary conditions are included below.

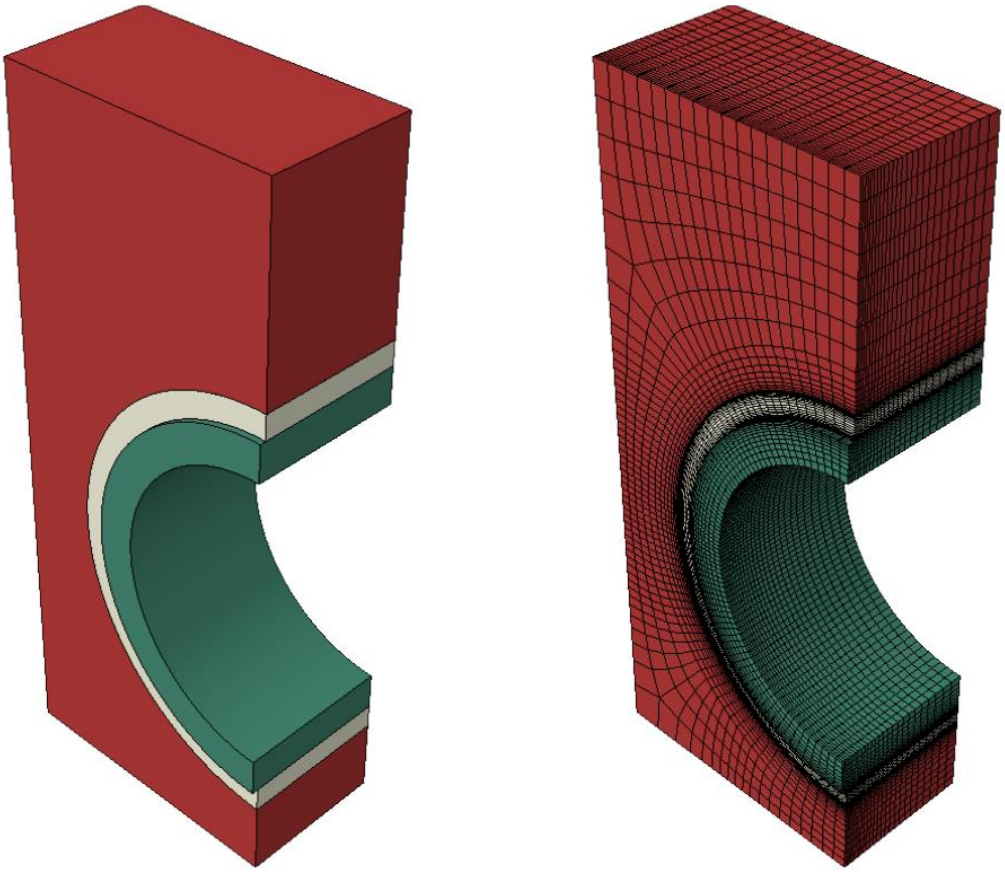

(a) Divertor monoblock, FEM distribution of the materials. Tungsten in red, OFHC-Cu in beige, CuCrZr-IG in green.

(b) Overview of FEM mesh used for the final analysis.

Figure 18: Quarter model used for FEM simulations.

The temperature decrease that takes place during HRP is given as an input on the whole domain, as we assume that the temperature is homogeneous in the monoblock. The decrease is modelled with two functions:

1) Exponential decay up until the temperature is 76 ºC. The decay is selected in order to follow the HRP temperature decrease more accurately.
2) Linear decrease from 76 ºC to 20 ºC in a short period of time. As the temperature is low enough that no more creep is expected, therefore the simulation is sped up.

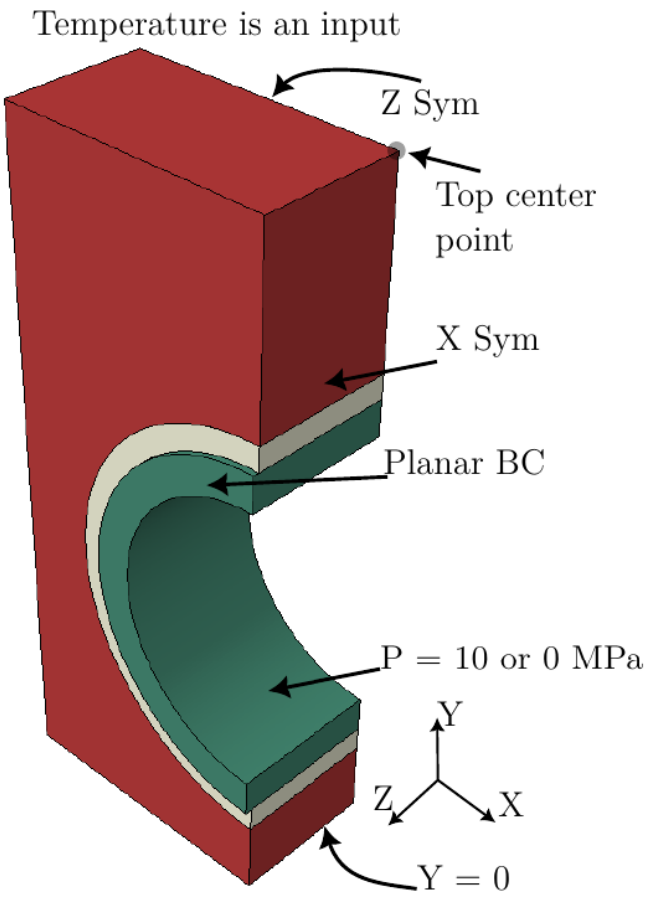

Figure 19: Applied boundary conditions.

	Pressure increase	Exponential drop of temperature	Rapid drop of temperature	Cutting of cooling pipe	Cutting of the part
Duration	10 s	55 000 s	1000 s	1 s	1 s
Temperature	580 °C	580 to 76 °C	76 to 20 °C	20 °C	20 °C
HRP pressure	0 to 10 MPa	10 MPa	10 to 0 MPa	—	—
Tie constrains	✓	✓	✓	✓	✓
X Symmetry plane	✓	✓	✓	✓	✓
Z Symmetry plane	✓	✓	✓	✓	✓
Y = 0 bottom plane	✓	✓	✓	✓	—
Planar BC	✓	✓	✓	—	—
Vertical fix of top and bottom center point	—	—	—	—	✓

Table 4: Simulation steps and their boundary conditions.

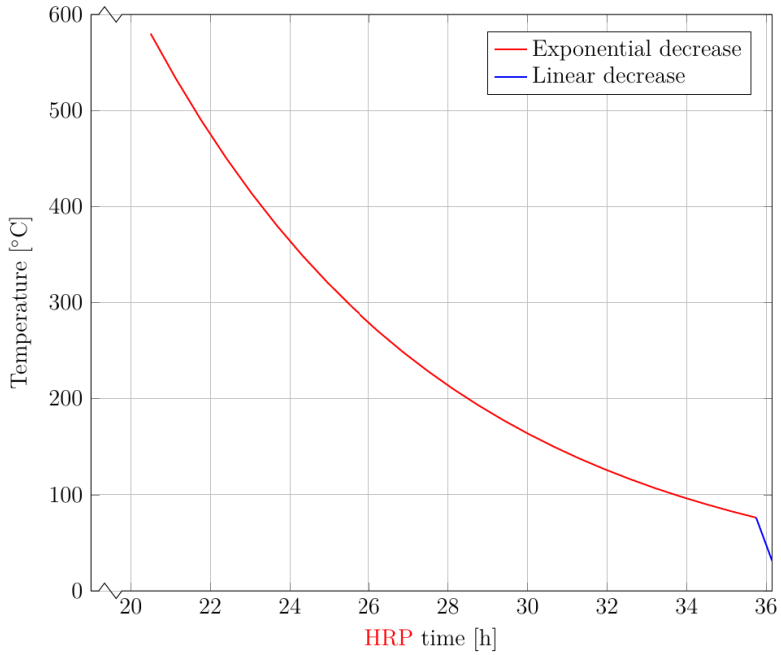

Figure 20: Simulated temperature decrease.

The planar boundary condition is added as several monoblocks are produced at the same time and there is a small gap between them. Therefore, we apply Bernoulli's assumption to the "middle" CuCrZr face.

Material data

The material property data is taken from EUROfusion's Material Property Handbook (MPH) (3) with the exception of creep as it is not included in the MPH and is discussed later.

Mesh design

The three different parts of the monoblock: tungsten armour, copper interlayer and CuCrZr pipe; were meshed independently. The meshes were then assembled into a single body using Abaqus' tie method. The meshes were refined as indicated below.

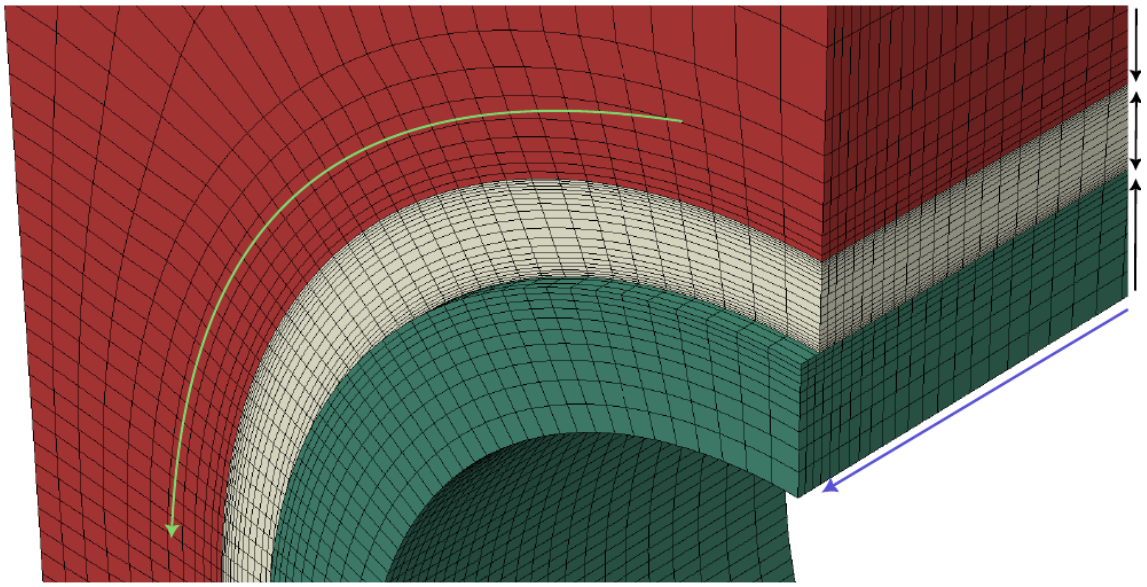

Figure 21: Mesh refinement controls.

The mesh was selected after doing a sensibility analysis using three different qualities: coarse (143E3 nodes), medium (415E3 nodes) and fine (1.52E6 nodes). The medium mesh obtained very similar results to the fine mesh and therefore was chosen for further analysis.

Creep modelling

The properties of copper and its alloys have been studied for over a century. Thorough studies of creep can already be found since the 1950s. Li in (4) did a literature review of the available primary and secondary creep models for a large selection of copper alloys. No primary creep model is present for OFHC-Cu. For CuCrZr there is a primary creep model available and several secondary models. However, the temperature-stress range for these models is out of the scope of the current analysis. It was decided that due to a lack of models in the literature, only the secondary creep model for OFHC-Cu would be used. The model follows the Norton-Bailey (also known as Power decomposition) law, indicated below.

$$\dot{\epsilon}^{cr} = \dot{\epsilon}_{sd} = 38.8 \cdot \tilde{\sigma}^{4.8} \cdot e^{-\frac{197\,000}{\Re \cdot T_{abs}}}$$

$$\frac{\delta \dot{\epsilon}^{cr}}{\delta \tilde{\sigma}} = 38.8 \cdot 4.8 \cdot \tilde{\sigma}^{3.8} \cdot e^{-\frac{197\,000}{\Re \cdot T_{abs}}}$$

$$400\,^{\circ}\mathrm{C} \leq T \leq 700\,^{\circ}\mathrm{C}$$

$$15\,\mathrm{MPa} \leq \tilde{\sigma} \leq 105\,\mathrm{MPa}$$

The creep model was implemented in Abaqus using its CREEP subroutine. In the future, once primary creep data is available, the subroutine could be modified to also model primary creep.

Prediction of residual stresses in experimental tests

The results obtained by the FEM simulation will be compared to experimental residual stress measurements of the monoblock. However, in order to carry out the experiments, the monoblock first has to be taken out of the assembly. Afterwards, due to the limited sample volume of the FIB—DIC machine, the monoblock has to be cut in two.

The cutting operations will change the structure or the monoblock and will change the residual stresses. Therefore, in order to correctly interpret the experimental measurements, the change in stresses has to be quantified first. In the present work, the cutting of the CuCrZr pipe and the cutting of the monoblock were also simulated.

Results

Impact of creep in the residual stresses

Comparing the predicted residual stresses between the simulation with creep and the one where creep was not taken into account, shows that the selected secondary creep model had little to no impact on the predicted stresses. A third simulation was done where the creep stress exponent was set to 7, which is regarded as a high value in the literature. This third simulation also showed very little change in the predicted residual stresses. Below are the obtained results.

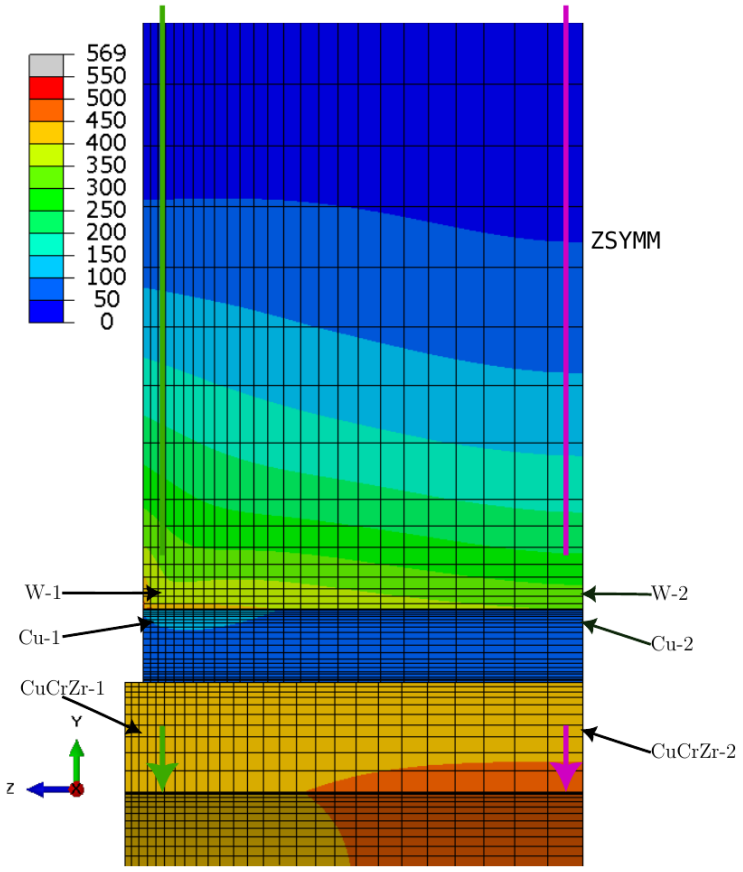

Figure 22: Selected stress distribution paths, green and purple.

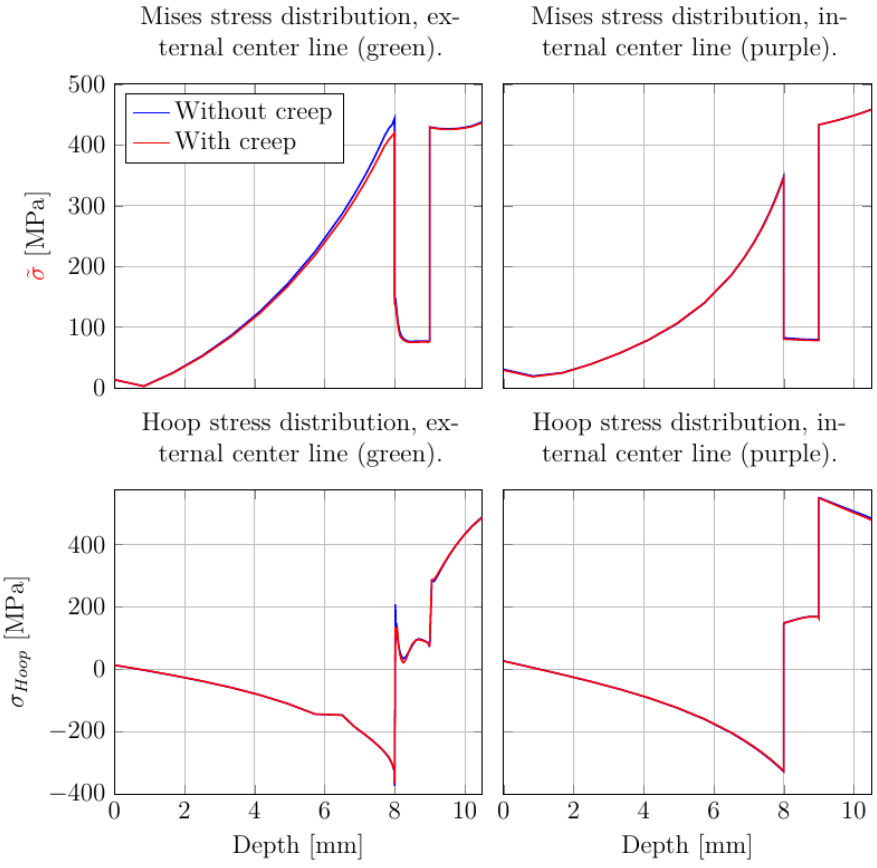

Figure 23: Stress distribution comparison between the simulation with creep and without.

Stress change after cutting operations

The simulated cutting operations show a major change in the distribution of residual stresses.

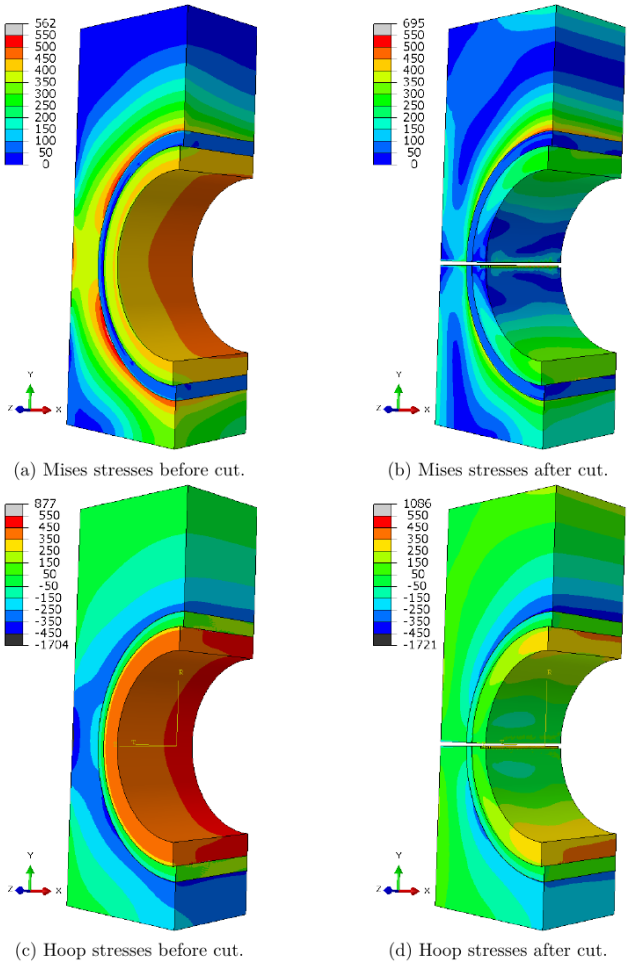

(a) Mises stresses before cut. (b) Mises stresses after cut.

(c) Hoop stresses before cut. (d) Hoop stresses after cut.

Figure 24: Stress change after the cutting operation.

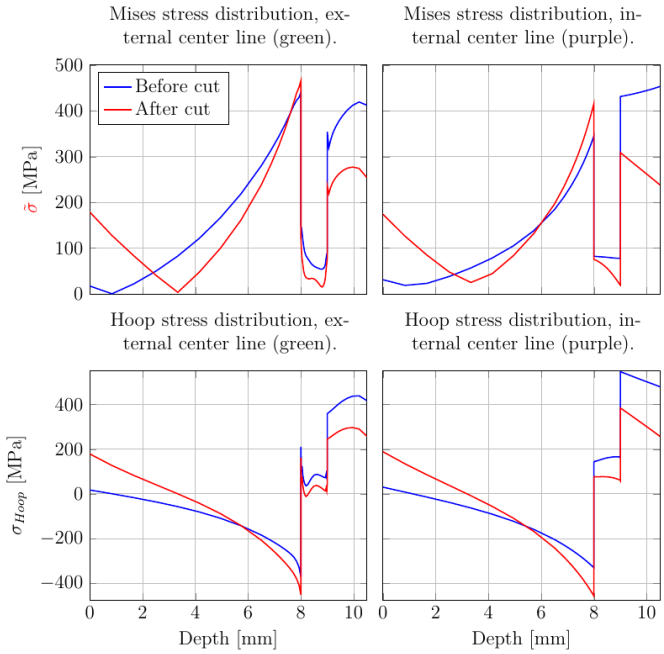

Figure 25: Stress distribution after cutting operation.

The simulation is able to show the stress evolution and concentration that takes place during the cutting operation as shown below.

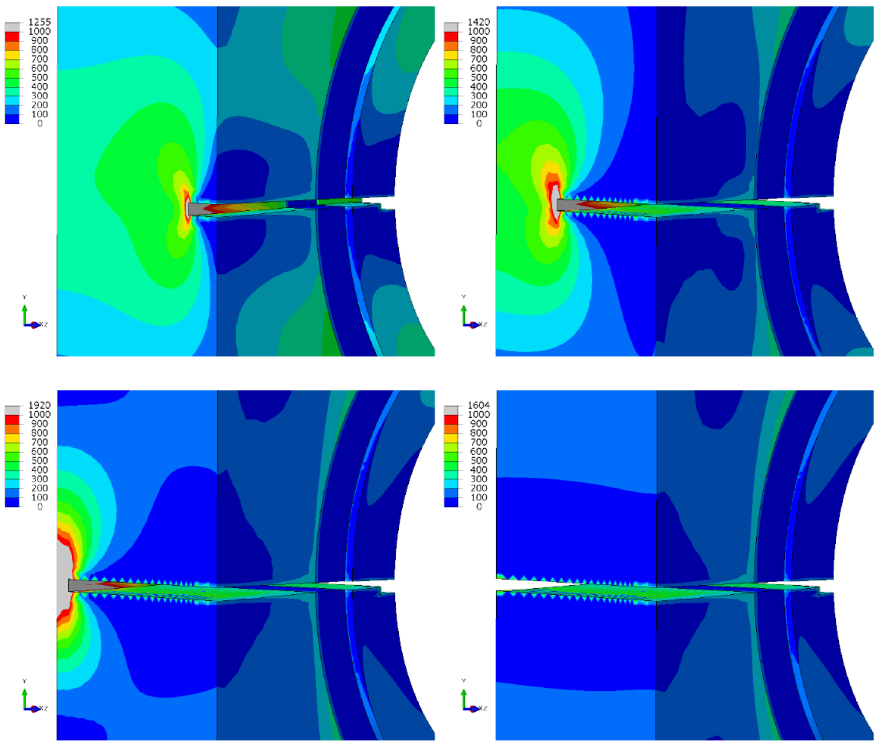

Figure 26: Stress concentration during the cutting operation.

Conclusion

The obtained results show that creep, with the selected creep model, has no impact on the predicted residual stresses when compared to the elasto-plastic assumption.

The results from the cutting operation show a major change in the stresses of the monoblock. This indicates that experimental measurements will produce results that are not directly representative of the state of the monoblocks after production.

The results obtained from this work have served as a reference for further material testing and the interpretation of experimental residual measurements.

Referencias - References

1. YOU, Jeong-Ha, LI, Muyuan and ZHANG, Kuo. Structural lifetime assessment for the DEMO divertor targets: Design-by-analysis approach and outstanding issues. *Fusion Engineering and Design*. 2021. Vol. 164, p. 112203. DOI https://doi.org/10.1016/j.fusengdes.2020.112203.

2. YOU, Jeong-Ha, LI, Muyuan and ZHANG, Kuo. Structural impact of creep in tungsten monoblock divertor target at 20 MW/m2. *Nuclear Materials and Energy*. 2018. Vol. 14, p. 1–7. DOI https://doi.org/10.1016/j.nme.2017.12.001.

3. GORLEY, Michael, DIEGELE, Eberhard, GAGANIDZE, Ermile, GILLEMOT, Ferenc, PINTSUK, Gerald, SCHOOFS, Frank and SZENTHE, Ildiko. The EUROfusion materials property handbook for DEMO in-vessel components—Status and the challenge to improve confidence level for engineering data. *Fusion Engineering and Design*. 2020. Vol. 158, p. 111668. DOI https://doi.org/10.1016/j.fusengdes.2020.111668.

4. LI, G., THOMAS, B. G. and STUBBINS, J. F. Modeling creep and fatigue of copper alloys. *Metallurgical and Materials Transactions A*. October 2000. Vol. 31, no. 10, p. 2491–2502. DOI 10.1007/s11661-000-0194-z.

Dedicated to my family
and all the wonderful people at IPP.

This work was produced using LuaLaTeX, Fortran 77–08, Abaqus CAE, (Wx)Maxima, TeXstudio, Emacs, Inkscape and Python.

Abstract

The W-Cu divertor target shall be produced using the HRP (Hot Radial Pressing) method, which utilizes high temperatures (580 °C) and pressures (60 MPa). The process produces a strong joint between the tungsten armor, the copper interlayer and the copper alloy cooling pipe. Due to the substantial mismatch in thermomechanical properties of the materials and the thermal transient that takes place in HRP, residual stresses build-up during production. Previous computational studies have analyzed the residual stresses of the parts after HRP under the elasto-plastic assumption, while viscous effects were only considered as a special case. Experimental studies, such as neutron diffractometry, were performed to measure the residual stresses and compare them with the computational results. Further experiments are to be performed which require computational models to aid in the interpretation of the measurements. However, non-trivial technical issues have to be solved first.

In this thesis, the impact of viscous stress relaxation is further analyzed using FEM (Finite Element Method) and the implementation of a cutting procedure is developed. In addition, the results are utilized to support experimental stress measurements, material testing and component design.

Resumen

El escudo del divertor compuesto por W-Cu será producido por el método HRP (Hot Radial Pressing), el cual utiliza altas temperaturas (580 °C) y presiones (60 MPa). El proceso genera una fuerte unión entre la armadura de tungsteno, la entrecapa de cobre y tubería de refrigeración, compuesta de una aleación de cobre. Debido a la notable diferencia en las propiedades termomecánicas de los materiales y al transitorio térmico durante HRP, se generarán estreses residuales. Estudios previos analizaron el aumento de estreses residuales que tiene lugar en la producción usando modelos elasto-plásticos, mientras que los efectos viscosos solo se consideraron de forma puntual. Se realizaron estudios experimentales, como difractometría de neutrones, para medir los estreses residuales y comparar los resultados con métodos computacionales. En el futuro se realizarán estudios experimentales que requiren de modelos computacionales para la interpretación de los resultados. Sin embargo, previamente ciertos retos técnicos tienen que ser resueltos.

En esta tesis se profudiza en el impacto de la fluencia usando la técnica de elmentos finitos. También se desarrolla una técnica para simular cortes. Los resultados obtenidos son utilizados para el apoyo de mediciones de estreses residuales, pruebas de materiales y diseño de componentes.

Contents

List of Figures

List of Tables

Listings

List of Algorithms

List of Symbols

Notation	Description
E_{ac} / Q / G	Activation energy for self-difussion, Gibbs free energy
E	Young modulus
G	Shear modulus
T	Temperature
α	Thermal expansion coefficient
$\dot{\epsilon}^{cr}$	Creep strain rate
$\dot{\epsilon}_{pr}$	Primary creep strain rate
$\dot{\epsilon}_{sd}$	Secondary creep strain rate
ϵ^{cr} / ϵ^{vp}	Creep/viscoplastic strain
ϵ^{el}	Elastic strain component
ϵ^{in}	Inelastic strain component
ϵ^{pl}	Plastic strain component
ϵ^{th}	Thermal strain component
ϵ^{tot}	Total strain
ϵ_{pr}	Primary creep strain
ϵ_{sc}	Secondary creep strain
λ	Thermal conductivity coefficient
$\mathfrak{R}$	Universal gas constant
σ_Y	Yield stress
$\tilde{\sigma}$	Deviatoric stress component. Mises criterion
t_d	Exponential decay time
t_n	Time-step n

Acronyms

Notation	Description	Page List
BC	Boundary Condition	12, 13, 15, 17, 18, 35, 39, 56
CuCrZr-IG	CuCrZr alloy ITER Grade	3, 6, 12, 18, 26, 73
DEMO	DEMOnstration Reactor	1, 9, 12, 66, 104
DIC	Digital Image Correlation	9, 11, 33, 34, 36, 37, 53, 61, 65, 87
FEM	Finite Element Method	8, 9, 11, 12, 23, 38, 48, 52, 64, 65
FGM	Functionally Graded Materials	86
FIB	Focused Ion Beam	9, 11, 33, 34, 36, 37, 53, 60, 61, 65, 87
GUI	Graphical User Interface	87
HHF	High-Heat-Flux	1
HIP	Hot Isostatic Pressing	4
HRP	Hot Radial Pressing	4, 5, 8, 11, 13, 15–17, 33, 63, 65
ITER	International Thermonuclear Reactor	1, 2, 9, 103
MPH	Materials Property Handbook	6, 18
OFHC-Cu	Oxigen Free, High Conductivity Copper	3, 4, 6, 9, 12, 18, 19, 24, 26, 31, 41, 43, 53, 63–65, 73, 83
OFP-Cu	Oxigen Free, Phosphorous-dopped Copper	24

Notation	Description	Page List
PFC	Plasma Facing Component	9
PFM	Plasma Facing Material	1
RP	Reference Point	18

Chapter 1

Introduction

Nuclear fusion reactors generate energy by merging light atoms into heavier elements. This process takes place in high vacuum and high temperature. The fusion process releases energy that has to be taken out of the reactor in order to cool it down. In the future, it is expected that the released heat from the reactor will drive a thermodynamic cycle in order to transform the energy released during fusion into electricity. Projects such as the International Thermonuclear Reactor (ITER) and DEMOnstration Reactor (DEMO) aim to get closer to fusion power.

1.1 Divertor design

One of the most critical components in Tokamak type reactors is commonly known as the divertor. In these reactors, the divertor is found at the bottom of the fusion chamber and it spans all the circumference, as it is shown in Figure 1.1, colored in gray. A schematic view of the divertor design to be used in ITER is shown in Figure 1.2. The divertor targets are a High-Heat-Flux (HHF) component, meaning they receive a large amount of heat that will need to be exhausted. In the case of reactors such as ITER and DEMO, the divertor will use tungsten as the Plasma Facing Material (PFM) and copper alloys as the material to carry the coolant. It was decided to use tungsten as PFM due to its excellent behavior under high temperatures, low erosion due to the high energy particles emitted from the plasma [3], low tritium retention and high melting point. Copper was chosen for its high thermal conductivity, ductility and oxidation resistance. A section of a divertor mock-up with the different materials can be seen in Figure 1.3.

Due to the critical role the divertor plays inside the reactor, great care has to be put in ensuring its structural integrity over its lifetime. A complete study of the structural lifetime assessment for DEMO divertor targets was already carried out [4–7, 43]. However, such studies did not take into account primary creep effects that occur in copper and copper based alloys due to a lack of available data and only used secondary creep models, which had no discernible effect in the residual stresses after the production of the divertor monoblocks. This results in a potentially conservative lifetime assessment, which is preferred from a safety point of view. However, viscous effects can have a measurable reduction on the stress of the material if it operates at high temperatures, specially due to primary creep during production and early life of the part. Without information on the

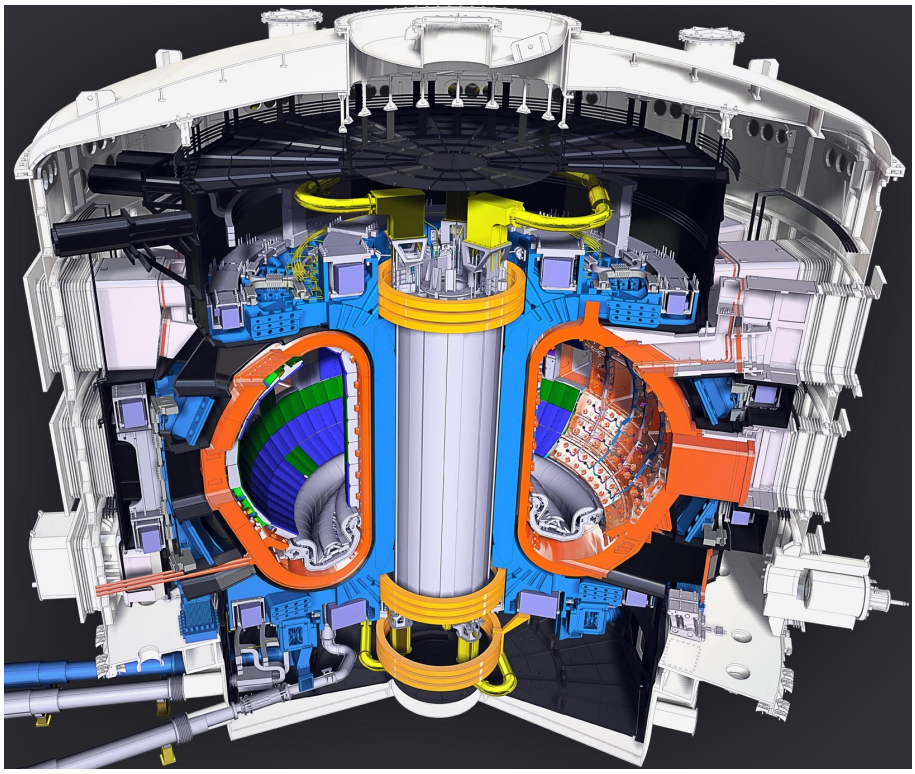

Figure 1.1: Design of ITER's Tokamak reactor, obtained from [1].

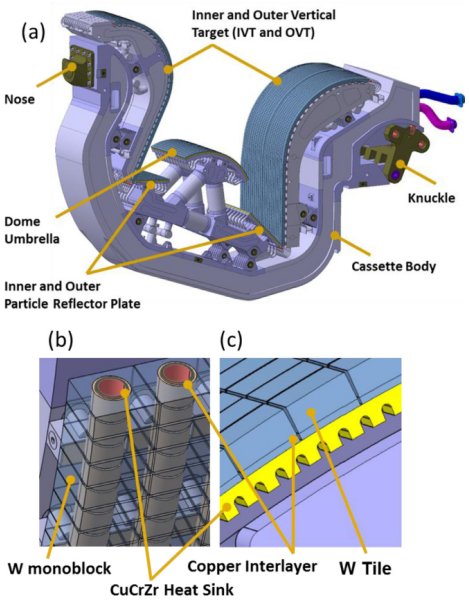

Figure 1.2: Diagram and description taken and quoted from [2]. (a) Schematic view of ITER divertor consisting of inner and outer vertical targets, dome umbrella, dome particle reflector plates and cassette body; (b) monoblock geometry at the inner and outer vertical targets; and (c) flat tile geometry at the dome umbrellas and particle reflector plates.

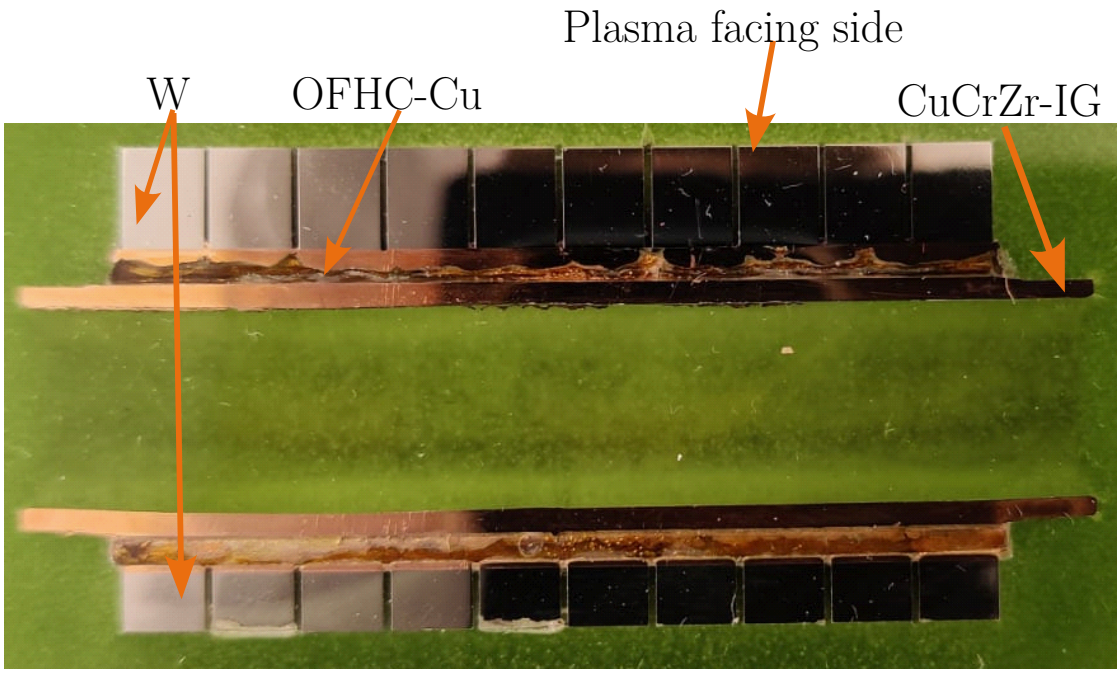

Figure 1.3: Cut along the axis of an array of divertor monoblocks.

initial material state, subsequent studies of the part may not accurately represent its real state during operation. Therefore, the goal of this study is to asses the impact of viscous stress relaxation that takes place during the production of the divertor components on the copper interlayer and cooling pipe.

1.2 Material properties and temperature induced stresses

Due to the different thermomechanical properties of the materials in the divertor target monoblock, stresses will build up during thermal loading. In Table 1.1 a summary of some temperature-dependent properties for tungsten, copper and its alloy are presented. The thermal expansion coefficient, α, of tungsten is one of the lowest for pure elements, while in copper, it is one of the largest. This property difference is the reason that a Oxigen Free, High Conductivity Copper (OFHC-Cu) interlayer was added between the tungsten monoblock and the CuCrZr pipe. The interlayer accommodates the differential thermal strain, ϵ^{th}, between the tungsten and CuCrZr allowing a softer joining between these two parts. A direct joining of the two materials would cause higher stresses that could affect the mechanical integrity of both the CuCrZr cooling tube and tungsten.

Material	E [GPa]		α [K^{-1}]		λ [$W K^{-1} m^{-1}$]		σ_Y [MPa]	
	297 K	873 K	297 K	873 K	297 K	873 K	297 K	873 K
W	398	387	4.5×10^{-6}	4.72×10^{-6}	173	128	1350	764
OFHC-Cu[a]	117	81.3	1.68×10^{-5}	1.88×10^{-5}	401	360	3	3
CuCrZr	127.5	95	1.67×10^{-5}	1.86×10^{-5}	218	346	280	190[b]

Table 1.1: Summary of thermomechanical properties of tungsten, pure copper and CuCrZr. The complete list is in Appendix A.

[a]The yield stress for the material has been set to 3 MPa since casted copper is a very soft material that mostly behaves plasticly.

[b]At 350 °C.

1.3 Production process of divertor monoblocks and consequent buildup of residual stresses

The production of divertor monoblocks starts by fabricating ingots of tungsten using the hot rolling method. These are then cut into blocks with the specified dimensions and a hole is cut in them. The hole is not positioned in the middle of the body but slightly offset, as shown in Figure 1.3. Then, molten OFHC-Cu is casted into the hole that was created in the tungsten and it is allowed to cool. Afterwards, a smaller hole is drilled concentrically to the first into the copper, generating the copper interlayer. Finally, a pipe made of a copper-chromium-zirconium (CuCrZr) alloy is inserted into the hole. However, there are small variations of the process between manufacturers. The process described above corresponds to monoblocks provided by A.L.M.T®, which also did the copper casting. The second manufacturer, AT&M®, already provided the finished copper interlayer, which was produced using Hot Isostatic Pressing (HIP).

In order to create a strong joint between the different materials that compose a divertor monoblock, the Hot Radial Pressing (HRP) process is utilized. HRP uses high temperatures in order to soften one or more materials and high pressures to diffuse the materials among themselves, generating a strong joint. For our case, the assembled monoblocks are heated up in a furnace under vacuum and then an inert gas is injected at high pressures into the CuCrZr tube to complete the joining process. Afterwards, the monoblocks are cooled down with some residual pressure inside the tube. The pressures, temperatures and timing of the HRP process are shown in Figure 1.4. The HRP process was carried out by ENEA.

A special mention has to be made regarding the bonding of tungsten and copper. These two elements barely diffuse into each other, which would nullify the goal of the HRP process. However, the wettability between these two materials is good enough to ensure a strong bond between the different parts after HRP [8].

1.3.1 Residual stresses buildup during production

As explained in section 1.2, temperature transients will generate stresses within the part. During the production process, a large thermal and pressure transient takes place due to the HRP joining technique as shown in Figure 1.4. At the end of the high pressure phase,

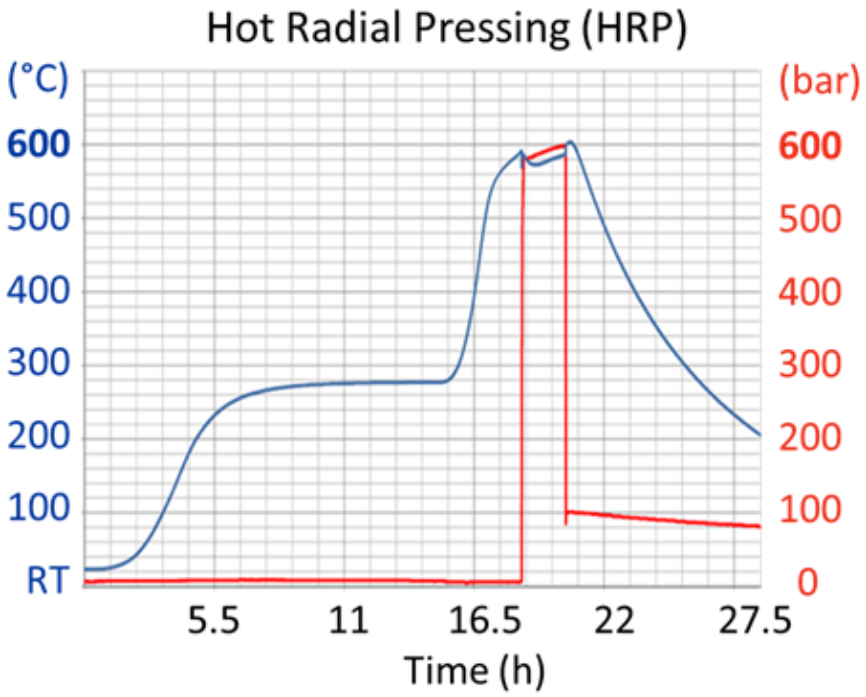

Figure 1.4: Pressure and temperature histogram of the HRP process. Image taken from the manufacturer (ENEA).

due to the prolonged high temperature, it could be assumed that the monoblock does not contain any residual stresses due to viscoplastic effects. However, as the part cools down, the thermally induced stresses build up. The end of the cooling period marks the initial state of the part once it starts operating in the reactor. Therefore, in order to carry out any subsequent analysis of the part in the reactor, its initial state needs to be defined.

1.4 A brief introduction to viscoplasticity and creep in solids

Viscoplasticity is the property that defines the flow of the material under some pressure and temperature difference which causes a permanent deformation of the part. The material flow can happen in solids under certain conditions, which tend to require high temperatures and stresses. When these two cases are present, the material may start to flow. The speeds at which solid materials flow tend to be very slow. For this reason, viscoplasticity in solids is usually referred as creep, the slow crawling of the material. Due to the nature of creep, it is mostly studied only on parts that withstand high stresses and high temperatures. The temperature threshold for the occurrence of creep is normally expressed with respect to the melting point of the material. Generally about 0.4 or 0.5 times the melting temperature is enough for the material to creep. Therefore, the effect of creep is taken into account for power generation facilities, turbines, the aerospace industry and plastics.

The presence of creep in a part indicates that the material will flow in favor of lowering

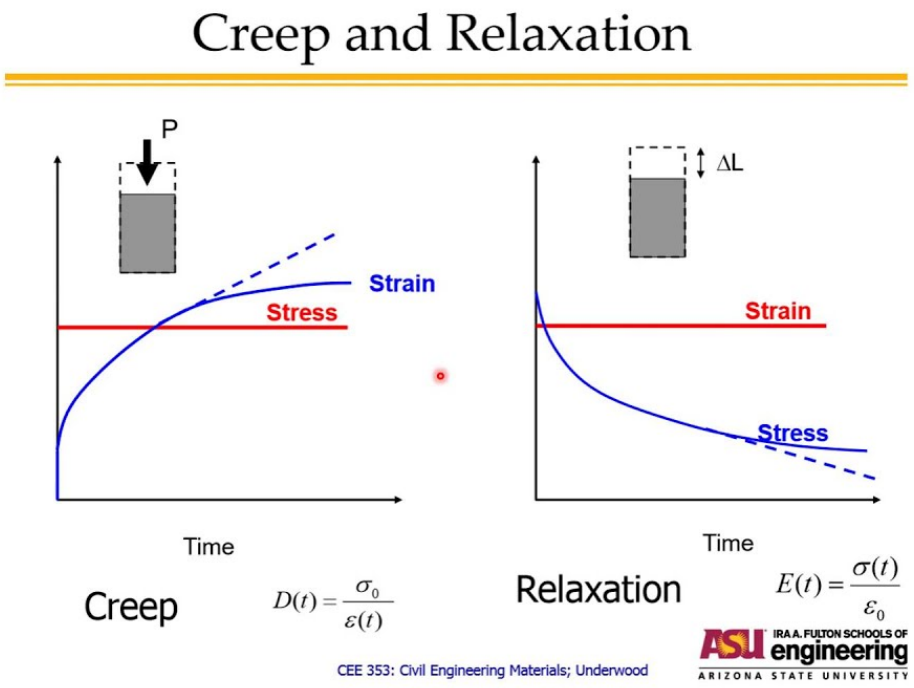

Figure 1.5: Creep relaxation as a function of stress (left) and as a function of deformation (right). Taken from Arizona State University (ASU), course CEE 353.

the stresses. This has a stress relaxation effect, since the material will be deformed in order to conform to and reduce the internal stresses. Figure 1.5 shows the evolution in time of the strain and stress that takes place under creep. As can be seen, on the right, for a fixed deformation, the stresses reduce over time; this is the creep/viscous relaxation effect. Therefore, **creep and other viscoplastic effects are time dependent,** which means their strain rate varies as time progresses.

The influence of creep is generally divided in three different regimes: primary, secondary and tertiary; see Figure 1.6. Primary creep is characterized by a high creep strain rate and takes place at the beginning of the loading. Secondary creep is differentiated by a constant creep strain rate and generally takes place during the operating life of the part. Tertiary creep is related to the damage of the material and shows a high strain rate up to rupture.

1.4.1 State of the art of viscoplastic analysis and modeling for OFHC-Cu and CuCrZr alloys

Viscous effects on solids have been studied for over a century as they can have a great impact on the stresses and lifetime of parts that operate at high temperatures [10]. However, for fusion materials, as can be seen in the EUROfusion Materials Property Handbook (MPH) [11], there is a noticeable lack of data when it comes to creep and creep-fatigue models for Cu and copper based alloys.

The relevant materials for the current study are OFHC-Cu and the selected CuCrZr alloy by EUROfusion, CuCrZr alloy ITER Grade (CuCrZr-IG). They are similar to industrially available alloys, but with a tighter control on the concentration of chromium,

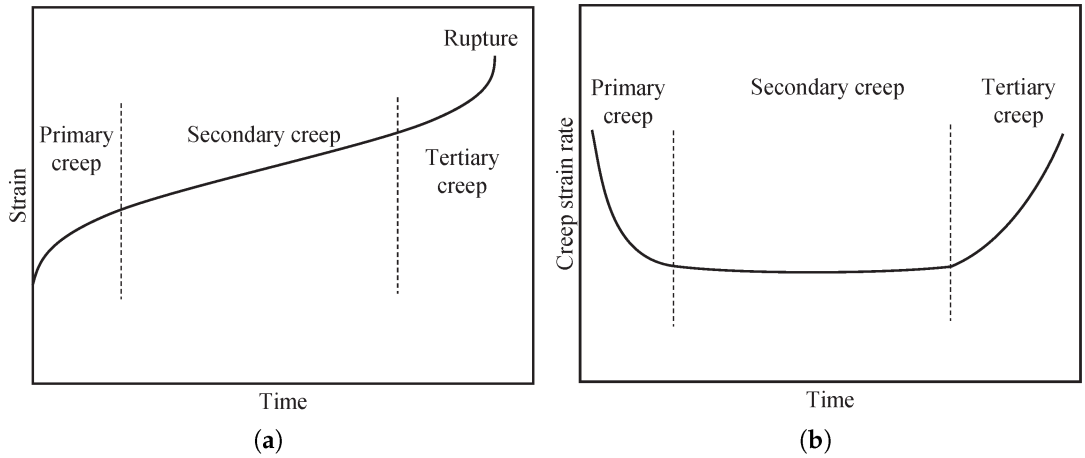

Figure 1.6: Strain deformation due to creep as a function of time (a). Creep strain rate (deformation velocity) for the three different regimes (b). Taken from [9].

zirconium and impurity elements. The viscoplastic properties of this alloy have been studied for decades [12–14]. However, the research has been focused mostly on secondary creep and generally covers a limited range of temperatures and stresses. Even though some studies have analyzed primary and tertiary creep [15, 16] and even creep-fatigue effects [17, 18]; the data quality, mathematical modeling or temperature-stress range fails to cover the needs of our study. For the task at hand, the relevant creep effect is primary creep, which is lacking on the literature.

Creep modeling has been mostly based on empirical testing and fitting the data to a predefined model. Throughout the study of viscous behavior in solids, different models have been developed that take into account various effects, such as temperature dependence [12] and specific cases, such as fracture dynamics using hyperbolic models. Depending on the material, different formulations have been proposed to better model and predict creep in them. In recent years physically-based models, sometimes referred to as non-parametric models, have been developed [19]. They have a great advantage over empirical formulations as they do not require any input from specific tests in order to fit parameters and they are much more general. However, non-parametric models require a thorough study of the crystalline properties of the material and its dislocation dynamics. The use of such models is not as direct when compared to empirical ones, as they require material properties that are not straight forward to obtain.

For the current study, a systematic analysis of the available data and viscoplastic models was performed for the pure copper and copper alloy. The discussion of the models and the selection of a final formulation is discussed in section 2.5.

1.5 Objective

The study carried out by You, Li and Zhang [4] analyzed the state of the divertor monoblock during its operation in the reactor. It was shown that there was a large uncertainty range between the calculated stress history of the divertor monoblocks depending on the assumed

stress-free temperature. The studied cases represented the two limiting cases:

- The part has no residual stresses after production. The stress-free temperature is 20 °C. This case tends to be the most common for simple analyses or those which can ignore residual stresses of parts after production.
- The part is assumed stress-free at the end of the high pressure transient during the HRP production process. In this case, the stress-free temperature is 580 °C. This assumes that the copper interlayer does not have residual stresses due to its softening at high temperatures and viscoplastic effects; whose impact was also partially studied in the study. However, stresses will build up during the cooling of the part.

Figure 1.7 summarizes the outcome of these two assumptions. The results show that depending on the stress-free temperature, parts of the monoblock could change its state from highly stressed to relaxed or from compression to tension. This study did not take into account primary creep and therefore the stress relaxation effect during production was limited. As it was already indicated, the omission of stress relaxation follows a conservative approach since it generates greater stresses, which would result in a lower lifetime expectancy.

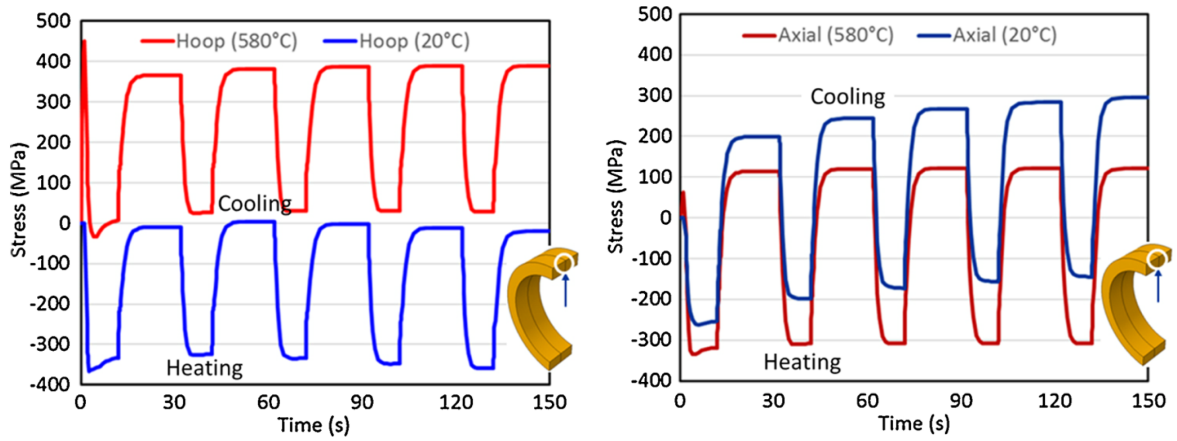

Figure 1.7: Stress history difference between limiting cases for stress relaxation. The stress is taken from the uppermost position of the pipe for the two limiting cases: null relaxation at 580 °C and perfect relaxation at 20 °C. Image and description taken from [4].

Nonetheless, the present study wants to focus on the impact of stress relaxation during the production of the divertor monoblocks, see Figure 1.8. The stresses, deformations and other material state changes that result from the production of the part represent the initial state once it starts operating in the reactor. Consequently, any subsequent in-reactor or after production studies or simulations rely on this information. Therefore, the full modeling of creep effects in the material produces a more realistic and accurate assessment of the initial state of the part, which lowers the uncertainty manifested by the gap between the two previously mentioned limiting cases.

The Finite Element Method (FEM) is used to predict and analyze the effect of creep in the materials. The material information that is currently available for the different

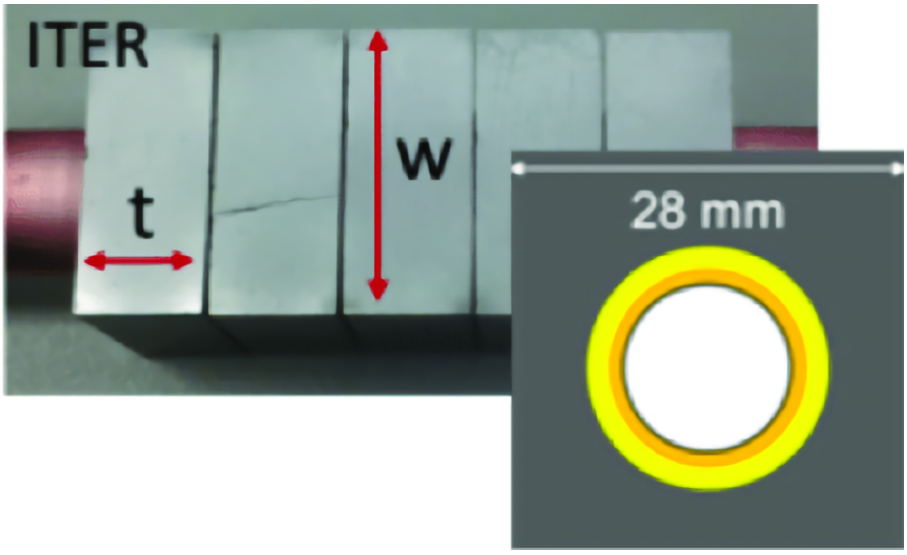

Figure 1.8: Plasma Facing Component (PFC) mock-up for the ITER divertor targets, similar to DEMO targets, taken from [20]. The actual geometry used for this study is not the one depicted in the image, but the one indicated in Appendix A.1.

sections is of high quality and can be trusted [11]. This allows the isolation of the effect of creep and allows a mostly direct review of the generated results.

As a result of the obtained conclusions, subsequent experimental studies and tests will be performed by third parties in order to asses the accuracy of the results. Primary creep characterization for OFHC-Cu and CuCrZr as well as residual stress analysis using the contour method, FIB–DIC (Focused Ion Beam–Digital Image Correlation) method and micro-indentations are among the proposed tasks to be performed by external research groups.

1.5.1 Employed resources

In order to carry out the study, the following resources were used:

Process and material information In order perform an analysis on the part, the information regarding the production process is required to correctly model the stress and deformation evolution. The data required to model the production process was by the Italian manufacturer. The material properties, with the exception of viscoplastic behavior, will be taken from the fusion material handbook [11] and previous studies.

Abaqus Abaqus [21] is the FEM software developed by Dassault Systems as part of their simulation suite. It is used as the simulation environment where the main results of the study were generated. As not all the functionality needed to perform the analysis is available by default, Abaqus' subroutines were deployed. The Fortran 77 subroutines allows the specification of complex operations and behaviors that are tailored to the needs of the project.

Fortran The programming language Fortran [22, 23] is used to describe and model the creep behavior of the materials that is used in Abaqus. The Fortran program is integrated into Abaqus using it's Fortran 77 interface for the `CREEP` and `USDFLD` subroutines. The compiler used is Intel's Fortran OneAPI compiler [24], therefore the code uses modern Fortran (2003 and newer) features. The subroutines' code can be found in Appendix B.

(Wx)Maxima The libre[1] software Computer Algebra System (CAS) Maxima [25] is used as the sensibility analysis platform and as data processing utility. The program developed to analyze the data can be found in Appendix C.

Python The programming language Python [26] along with it's most widely used libraries is used to support the sensibility and data analysis. Python is also the official scripting language of Abaqus.

[1] More commonly known as Open Source Software (OSS).

Chapter 2

FEM and creep modeling

As previously explained, the goal of this study is to understand the impact of viscous stress relaxation during the production of the divertor monoblocks. In order to analyze the effect of creep in the part, two simulations were created. Both follow the same setup, but differ in the material properties. In one model, creep was not taken into account while the second one was simulated with creep. By isolating the effect of creep, we are able to easily compare the impact that it has on the residual stresses. In this chapter, only the cooling of the monoblock assembly during HRP is discussed. The creep model and its implementation in the analysis is discussed in section 2.5.

The results generated by the FEM simulation need to be compared with experimental studies in order to asses their accuracy and reliability. For this reason, other research groups have already performed and will perform several tests in order to measure the residual stresses that the monoblock has after it has been produced. The monoblocks have to be cut out of the assembly in order for them to be studied. Furthermore, the machine that will be used to perform a FIB–DIC analysis has a limited sample volume. This requires that the monoblock be cut in two pieces. These cutting operations will change the residual stresses that are ultimately measured when compared to the real stresses that the monoblocks have after they are produced. Therefore, the cutting operations had to be simulated in order to asses and quantify the stress change that will take place. Chapter 3 describes these operations. The FEM results from the cutting simulations will help interpreting the data generated by the experimental analysis.

2.1 Model setup and geometry

The geometry and the dimensions of the model are illustrated in Appendix A. The cooling pipe is not centered in the tungsten monoblock, therefore, only a quarter model was simulated. The symmetry planes are defined by:

- One cut plane perpendicular to the axial direction of the pipe at the center of the part.
- One cut plane which contains the center axis of the cooling pipe and is perpendicular to the plasma facing side of the monoblock. This symmetry plane is the one used in the “Section A-A” cut in Appendix A.

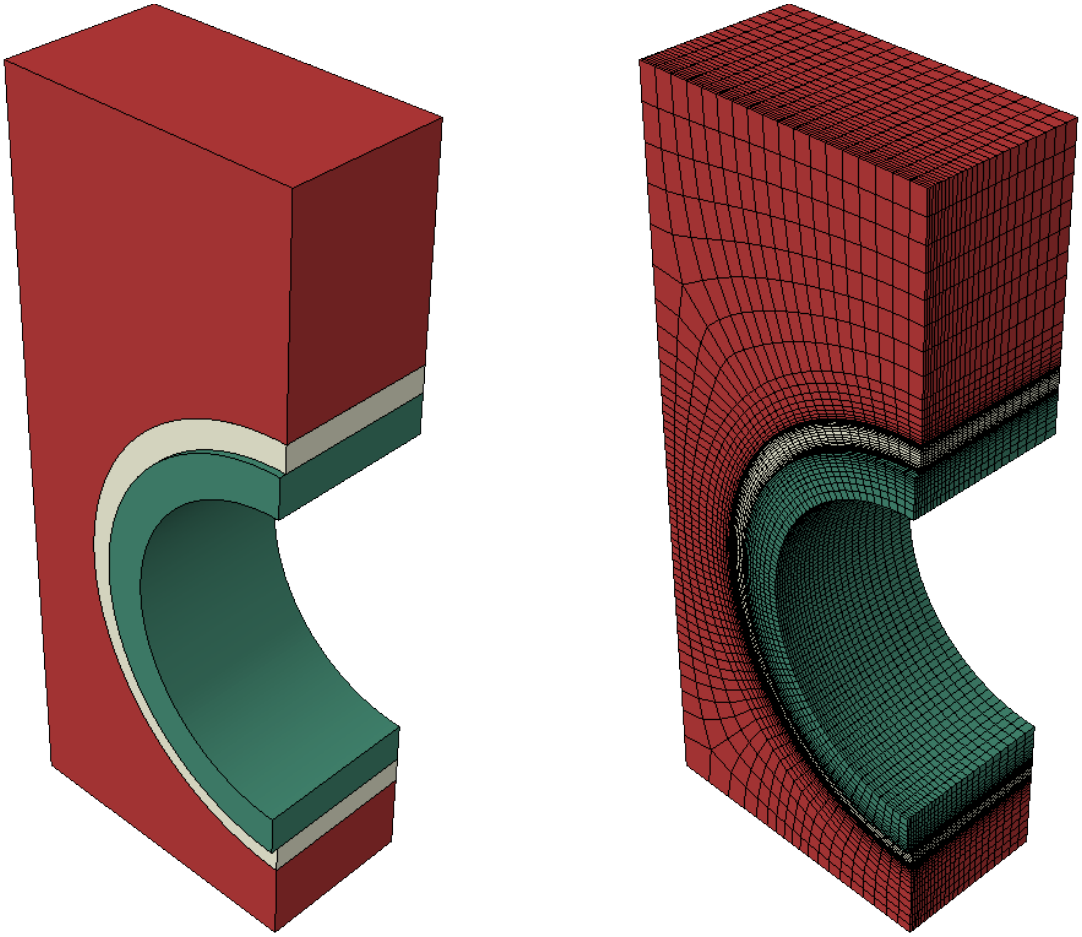

(a) Divertor monoblock, FEM distribution of the materials. Tungsten in red, OFHC-Cu in beige, CuCrZr-IG in green.

(b) Overview of FEM mesh used for the final analysis.

Figure 2.1: A quarter model used for FEM simulations.

This double symmetry is exploited in the FEM model with the required BCs (Boundary Condition). The final mesh model of the part used in the Abaqus simulation is shown in Figure 2.1a. It is noted that the geometry used in this study is the baseline design adopted for the EU-DEMO divertor target [20]. Nonetheless, the analysis methodology proposed here is also applicable to other design concepts.

2.2 Boundary conditions and simulation steps

2.2.1 Definition of the temperature history

The temperature is defined by the user as an input field. The temperature history was taken from the manufacturer's process data Figure 1.4. Due to the long cooldown period and small size of the monoblocks the temperature is assumed to be homogeneous in the component. Because of the high temperature sensitivity of the selected creep model, see

section 2.5, the cooldown of the part was modeled with two stages. The first temperature drop follows an exponential decrease, while the second follows a linear decrease. The exponential decrease models the temperature evolution during the manufacturing process more accurately. The linear decrease is used to speed up the simulation as the impact of the selected creep model at low temperatures on the accumulated creep strain is negligible, see Figure 4.9. Using the temperature profile from the manufacturer, we can define the temperature history as indicated in Table 2.2 and visualized in Figure 2.3.

Abaqus uses Equation 2.1 with the parameters from Table 2.3 to define exponential amplitudes. Using the data points from Table 2.2, setting A_0 and t_0 to zero as initial condition, we obtain the values shown in Table 2.4. The duration of the simulated time is indicated in Table 2.1.

$$f(t) = \begin{cases} A_0 + A \cdot e^{-\frac{t - t_0}{t_d}} & for \quad t \geq t_0 \\ A_0 & for \quad t < t_0 \end{cases} \tag{2.1}$$

2.2.2 Internal pipe pressure during HRP

During the HRP, the CuCrZr pipe is filled with an inert gas at high pressure when the temperature of the process is at its highest point. The high internal pressure allows the formation of a strong joint between the different parts by pressing them together. After the joining process is completed, the temperature is reduced and the part is cooled down. As we assume that the divertor monoblock has no residual stresses at the joining temperature due to the softening of the copper interlayer, the high pressure during joining plays no role. However, the residual pressure that is left in the pipe during cooldown was taken into account, as it lasts up until the part has reached room temperature. In order to include the internal pressure, a pressure load was applied to the internal wall of the CuCrZr pipe. The pressure was increased linearly from 0 MPa to 10 MPa in the first step. The pressure was maintained at 10 MPa during the cooldown and it was set back to 0 MPa for the following steps. The pressure history is also detailed in Table 2.1.

2.2.3 Symmetry boundary conditions and vertical constraint

Due to the double symmetry of the monoblock, a quarter model is simulated. The faces created by the symmetry planes are setup with their respective BCs. The symmetry BCs allow the monoblock to be constrained in the `X` axis, equivalent to `U1` in Abaqus, and in the `Z` axis, equivalent to `U3`; as shown in Figure 2.2. The symmetry BCs' formulation is shown in Equation 2.2.

$$\texttt{XSYMM} \equiv U1 = UR2 = UR3 = 0 \tag{2.2a}$$

$$\texttt{ZSYMM} \equiv U3 = UR1 = UR2 = 0 \tag{2.2b}$$

For the model to be fully constrained in space, the `Y` direction, `U2` in Abaqus, had to be fixed. Therefore, the bottom face of the monoblock was constrained to `Y=0`.However, after the cutting operation of the monoblock, explained in chapter 3, the part becomes

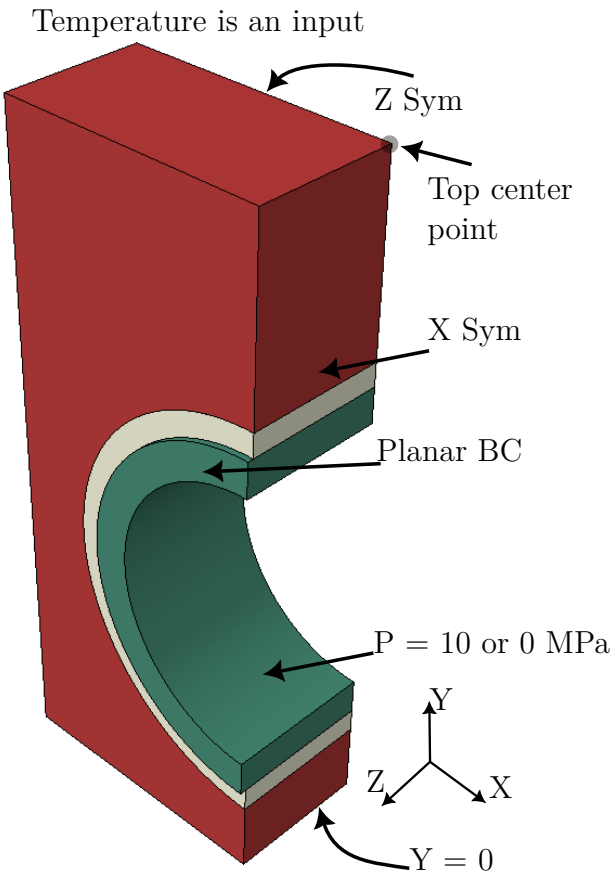

Figure 2.2: Boundary conditions applied on the monoblock. A constraint is added between tungsten and the copper interlayer and between the interlayer and the cooling pipe in order to tie the meshes together. This allows the seamless simulation between different parts even if the meshes are non-conformal; see Figure 2.4 for more information.

	Pressure increase	Exponential drop of temperature	Rapid drop of temperature	Cutting of cooling pipe	Cutting of the part
Duration	10 s	55 000 s	1000 s	1 s	1 s
Temperature	580 °C	580 to 76 °C	76 to 20 °C	20 °C	20 °C
HRP pressure	0 to 10 MPa	10 MPa	10 to 0 MPa	—	—
Tie constrains	✓	✓	✓	✓	✓
X Symmetry plane	✓	✓	✓	✓	✓
Z Symmetry plane	✓	✓	✓	✓	✓
Y = 0 bottom plane	✓	✓	✓	✓	—
Planar BC	✓	✓	✓	—	—
Vertical fix of top and bottom center point	—	—	—	—	✓

Table 2.1: Simulated steps and their boundary conditions. The cutting requires the setup described in subsection 2.2.4 and chapter 3.

	HRP, Figure 1.4		Extrapolated	Linear decrease
Time	20.5 h	28.5 h	35.75 h	36.15 h
Temperature	580 °C	200 °C	76 °C	20 °C

Table 2.2: HRP temperature change during the cooling of the divertor monoblock. The exponential decrease is extrapolated to last up to 15.25 h. After the exponential decrease, the temperature is reduced more rapidly with a linear ramp.

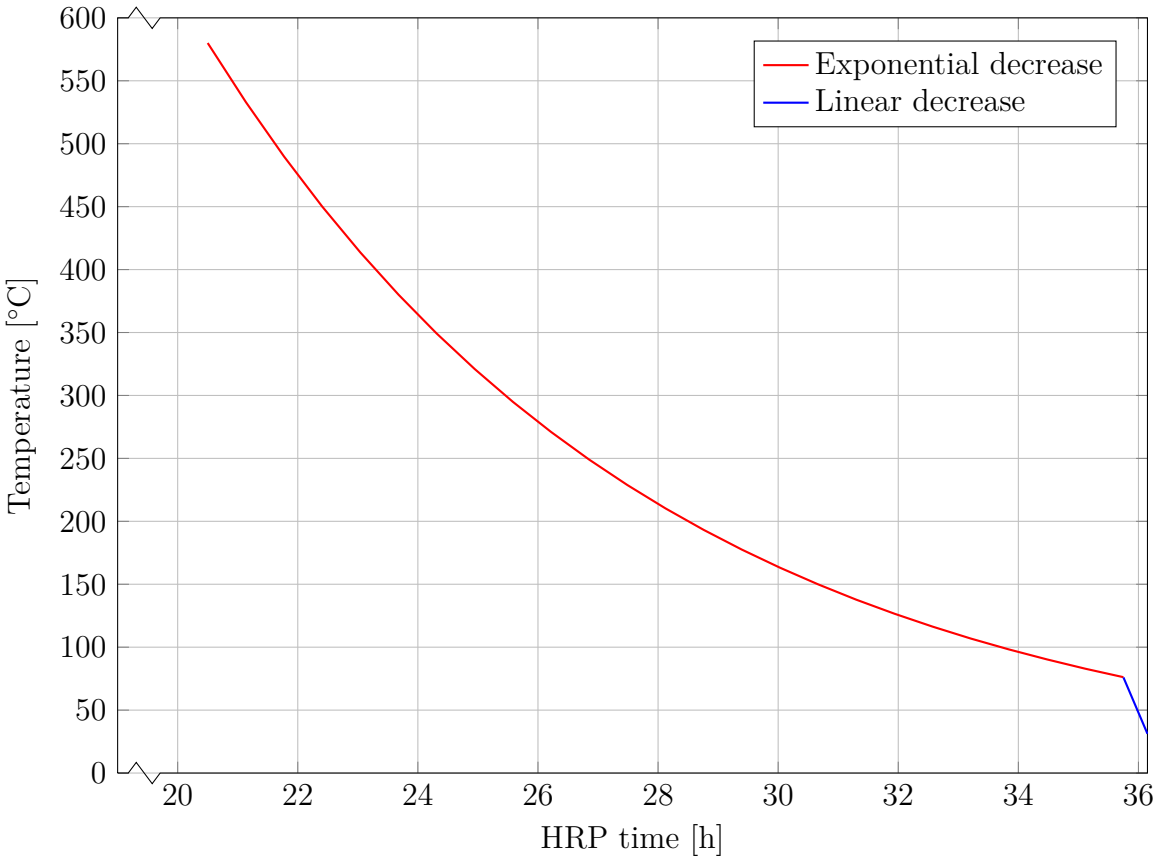

Figure 2.3: Visualization of the HRP temperature transient during the cooling of the divertor monoblock. The full temperature history is shown in Figure 1.4.

Initial amplitude	Max. amplitude	Starting time	Decay time	Step time
A_0	A	t_0	t_d	t

Table 2.3: Exponential decay parameters in Abaqus.

Initial amplitude	Max. amplitude	Starting time	Decay time
$A_0 = 0$	$A = 580\,°\mathrm{C}$	$t_0 = 0$	$t_d = 27\,050\,\mathrm{s}$

Table 2.4: Fitted parameters for the exponential decay of temperature.

two bodies. The upper section would therefore become unconstrained. For that reason, the center node of both the top and the bottom part are constrained to Δ`Y = 0` after the cutting step. During the cutting step the top and bottom face are constrained with Δ`Y = 0` to stabilize the cutting simulation and prevent stress concentration in the BCs.

2.2.4 Planar boundary condition

Several divertor monoblocks are joined at the same time to the CuCrZr pipe, producing the mock-up assembly in Figure 1.3. As is shown, there is a small gap between each monoblock. This means that during the HRP process, there may be some displacement of the middle-plane of the gap, as indicated in Figure 2.2 (planar BC). However, as the CuCrZr tube is a continuous body, the forces that act on the middle-plane at each point are equal from both sides; which indicates the plane should remain planar in the manufacturing process. However, not all points of the middle-plane are required to have the same load. This indicates that the middle-plane is allowed to displace and rotate, while remaining flat. For this reason, a "plane remains plane" BC is applied to the middle-plane of the CuCrZr tube, as indicated in Figure 2.2.

The boundary condition only lasts up until the end of the cooling period. It is deactivated afterwards in order to simulate the cutting of the individual monoblocks for further experimental studies as explained in chapter 3.

2.2.4.1 Implementation of "Bernoulli's assumption" boundary condition

The BC added to the external face of the CuCrZr is not trivial to realize in Abaqus. However, recent versions of Abaqus offer a built-in plug-in that allows the user to easily setup the planar BC. The plug-in is called "Plane Remains Plane". The user needs to be in the "Interaction" module and can then access the plug-in using the drop-down menu called "Plug-ins".

The setup performed by the plug-in in order to create the BC is the following:

- For each face that is to be assigned the BC, an auxiliary plane is created with a reference axis. The plane is not meshed, it is only defined geometrically. It will take part in the simulation as an infinitely rigid body. The `X/U1` direction of the local reference axis has to be perpendicular to the plane.

- The auxiliary plane is assembled against the selected face using the "Face-to-Face assembly" constraint.

- A "Hard contact" interaction property is defined.

- A "Surface-to-Surface contact" interaction is created between the auxiliary plane and the face. The previous hard contact is selected as the interaction. The main surface is the auxiliary plane and target face is the secondary. Finite sliding is used as sliding formulation.

- An auxiliary Reference Point (RP) is created more or less in the center of the face where the BC is being applied.

- A "Coupling" constraint is created between the RP and the face. The coupling type selected is "Continuum Distributing" with uniform weights.
- A BC condition is applied to the newly created RP which restricts `UR1` using the plane's local axis system.

The use of an auxiliary RP to distribute the load is needed. The simulation is unstable when only the contact formulation is used.

2.3 Material selection and properties

The material properties are taken from the EUROfusion MPH [11] with the exception of creep, as no data is given for OFHC-Cu nor CuCrZr. The materials selected are tungsten, OFHC-Cu and CuCrZr-IG. The standard EN 12163 [27] sets the following specification for alloying elements in CuCrZr: Cr (0.5-1.2 wt.%), Zr (0.03-0.3 wt.%), Fe (<0.08 wt.%), Si (<0.1 wt.%), others (<0.2 wt.%), Cu balance. CuCrZr-IG has a narrower range for the alloying elements: Cr (0.6-0.9 wt.%) and Zr (0.07-0.15 wt.%). The values for the different properties are included in Appendix A.

Tungsten is modeled as a brittle material (no plastic behavior) while OFHC-Cu and CuCrZr-IG are modeled with combined non-linear isotropic and kinematic hardening. In the case of tungsten, its elastic limit is not reached during the cooldown and therefore the assumption of purely elastic behavior is valid for this study. It is important to note that all properties of the materials are temperature dependent. However, the hardening parameters of CuCrZr are only available for the temperature range of 20 °C to 350 °C. Abaqus extrapolates the parameters for which there is no defined range by assuming the upper or lower bound as constant. For the casted copper interlayer, the yield stress, σ_Y, has been set to 3 MPa as the material deforms in a very soft and plastic manner. This value was taken from a data fitting process of cyclic tests and it is not based on the commonly agreed 0.2 %ϵ convention. The OFHC-Cu and CuCrZr material parameters are primarily taken from [28].

Viscoplastic effects were only modeled for OFHC-Cu, which is the softest material of the three. Ideally, creep of CuCrZr would need to be modeled, but the available creep models presented noticeable limitations for the current analysis due to their different temperature-stress ranges and alloy composition. Creep in tungsten was not considered as the temperature of the production process is well below half the temperature of tungsten's melting point. For the complete discussion of creep, refer to section 2.5.

2.3.1 A note on element deletion and field dependent properties

In order to carry out the cutting operation as described in chapter 3, an intermediate step needs to be taken when defining material properties in Abaqus. For the `USDFLD` field subroutine to take effect, it seems Abaqus requires a material property that is dependent on a user defined field. For this reason, all the materials have a property (in this study, electrical conductivity) defined with meaningless data and field dependent values as described in Table 2.5. Electrical conductivity was chosen as it has no impact on this simulation.

Entry	Electrical conductivity	Field 1
1	10	0
2	1	1

Table 2.5: Exemplary material parameters in order to enable the `USDFLD` subroutine.

2.4 Mesh design and analysis

The three different parts, corresponding to the three different materials, were meshed independently. A tie constraint was added to the interface between the parts to couple the meshes together. This approach differs from the commonly used partitioning scheme for multi-material and mesh-refinement cases in the computation of the interface. The partitioning scheme generates a single node in the partition interface which is shared by both materials. The tie approach uses two nodes, one from each mesh, and couples them. The difference between both methods is shown in Figure 2.4. Having two nodes on the interface allows the stresses and other field variables to be coupled separately. In the partitioning case, the output variables at the interface are averaged quantities.

The mesh was refined towards the interface as this area has the largest stress concentration and transition. It was refined towards the external surface along the axial direction as future experimental analysis will focus on such area. Finally, the mesh was refined along the hoop direction towards the middle height of the cooling pipe, which required all parts to be partitioned with a horizontal plane at the height of the center hole. The hoop refinement was needed in order for the cutting operation to converge. Figure 2.6 shows the direction of the refinement for each part. Quadratic hexahedral meshes were used for all the parts. For tungsten, a reduced integration scheme was used (`C3D20R`), while full integration was used for OFHC-Cu and CuCrZr (`C3D20`).

2.4.1 Mesh sensitivity analysis

A mesh sensitivity study was performed to select an efficient mesh resolution that still allowed accurate results. Three mesh qualities were chosen: fine, medium and coarse. Table 2.6 summarizes the mesh data. The finer mesh required noticeably more time to compute as its memory requirement was greater than the machine's free memory, approximately 55 GB. Therefore, Abaqus used the hard-drive to store intermediate results, which slowed down the simulation substantially. The mesh analysis used 6 CPU cores, however, for the fine mesh more CPU cores had a negligible improvement on the simulation speed due to the storage bottleneck. The mesh sensitivity analyses were performed on a slightly different geometry compared to the final one. However, this discrepancy is not expected to have had any impact on the quality of the analysis.

In order to compare the quality of the generated results between the different meshes, two stress distribution paths along the center of the part were taken. They start from the plasma facing side and go perpendicular to the plasma facing side up to the cooling face of the CuCrZr pipe. One is located in the external face of the monoblock and the other one along the body's internal centerline. The paths go through both material interfaces, where

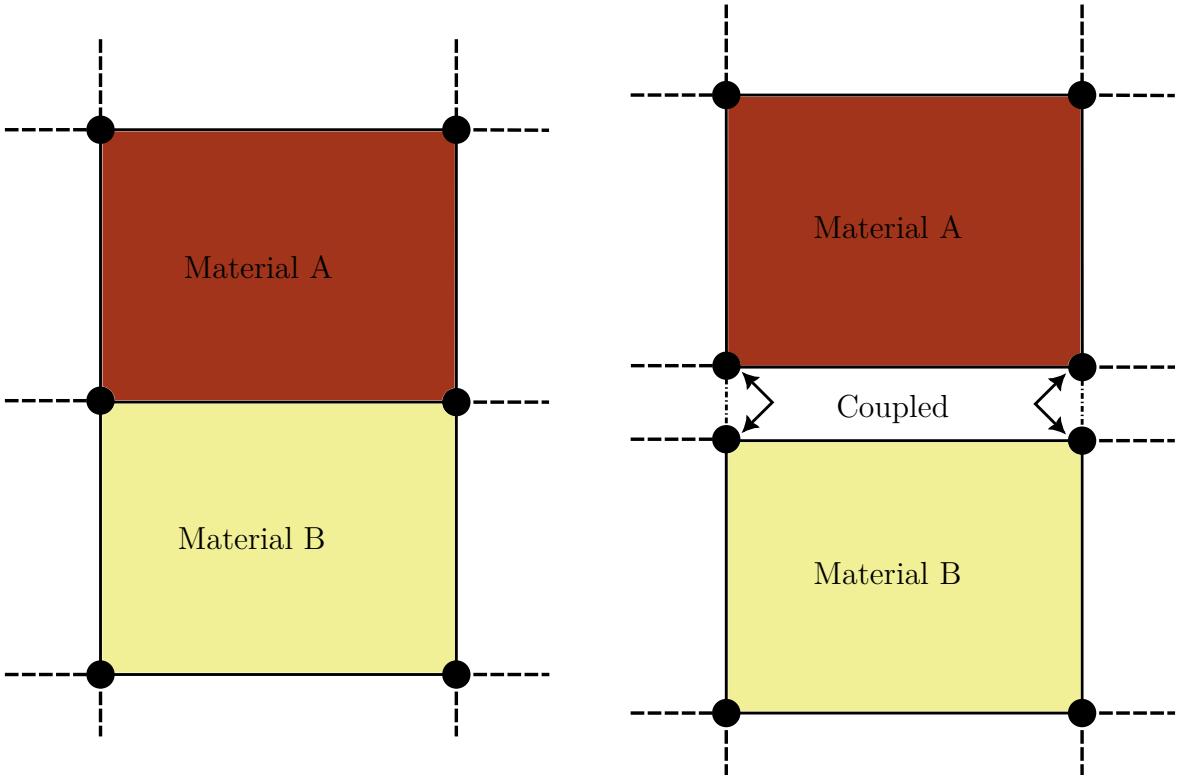

(a) Partitioned mesh with two materials.

(b) Tied meshes with two materials. There is a maximum separation tolerance value to tie surfaces together.

Figure 2.4: Partitioned mesh (a) in comparison with a tie constrain (b). The nodes are only required to be within the tied surfaces; conformance is not a requirement.

most convergence issues are expected. Both paths and the results are shown in Figure 2.5.

The coarse mesh shows a lack of convergence of stresses in the external path, while the medium and fine meshes obtained nearly identical results. The medium quality mesh was therefore chosen as the mesh to run the full analysis as it generates good results, comparable to the fine mesh while being computationally efficient.

2.5 Viscoplastic modeling

In order to model the effect of creep in the materials, Abaqus, among other FEM software, uses the strain partition assumption as indicated in Equation 2.3. It splits the strain in elastic or recoverable strain and inelastic strains.

$$\epsilon^{tot} = \overbrace{\epsilon^{el} + \epsilon^{th}}^{\text{Elastic deformation}} + \underbrace{\epsilon^{pl} + \epsilon^{cr}}_{\text{Inelastic deformation } (\epsilon^{in})} \tag{2.3}$$

The partition of strains allows for the separate modeling of each effect. In the case of creep, Abaqus already offers several material laws, some are listed in Table 2.7. In order to

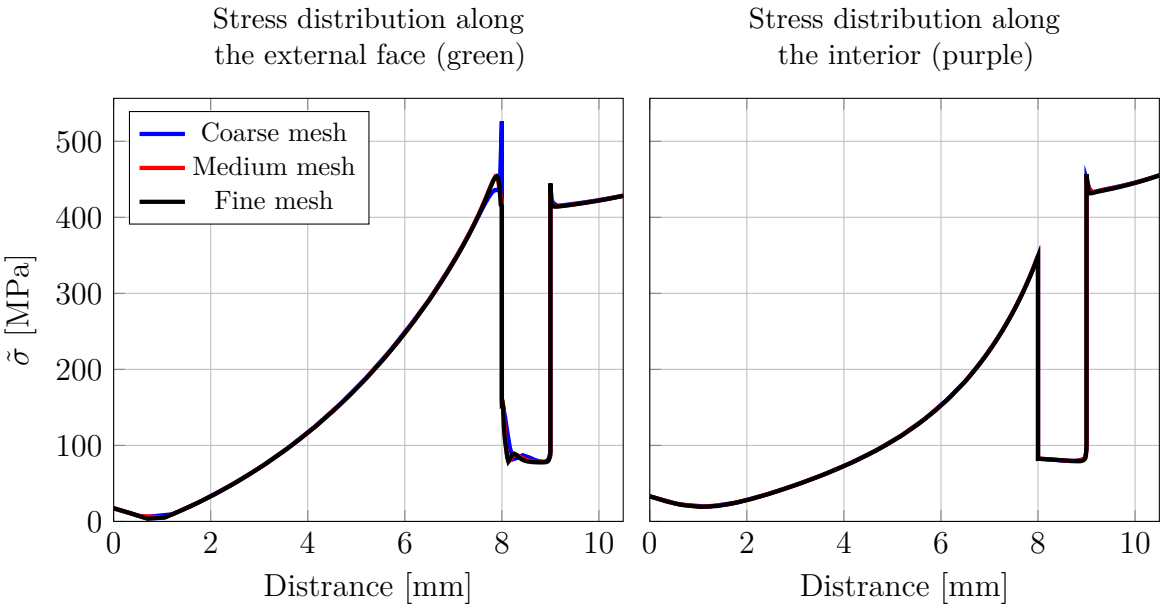

(a) Stress distribution from the plasma facing side to the cooling section.

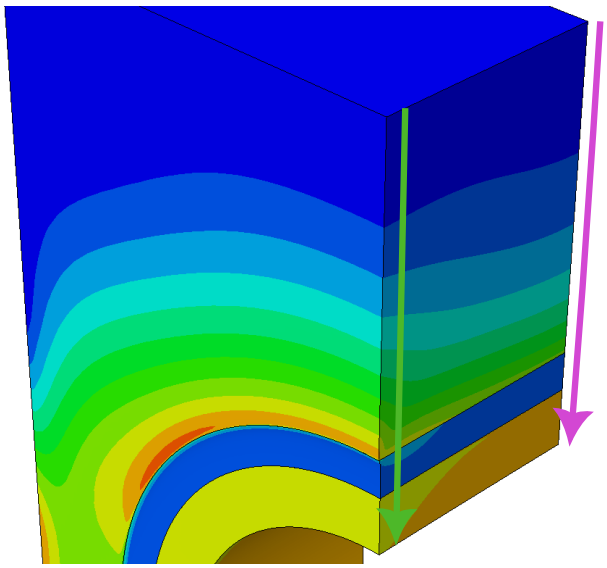

(b) Paths used to asses mesh quality. The geometry is slightly different to one used for the final analysis.

Figure 2.5: Convergence of stresses for the different mesh qualities assessed with two distributions.

Mesh	Nodes	Number of variables	Memory requirements [MB]	CPU time [h]
Coarse	143×10^3	428×10^3	8.95×10^3	6
Medium	415×10^3	1.25×10^6	39.4×10^3	32.5
Fine	1.52×10^6	4.55×10^6	228×10^3	555
Final design	392×10^3	1.16×10^6	37.5×10^3	36

Table 2.6: Mesh parameters for the mesh sensitivity analysis and final mesh. Simulation time given for the cooldown period only and without creep effects.

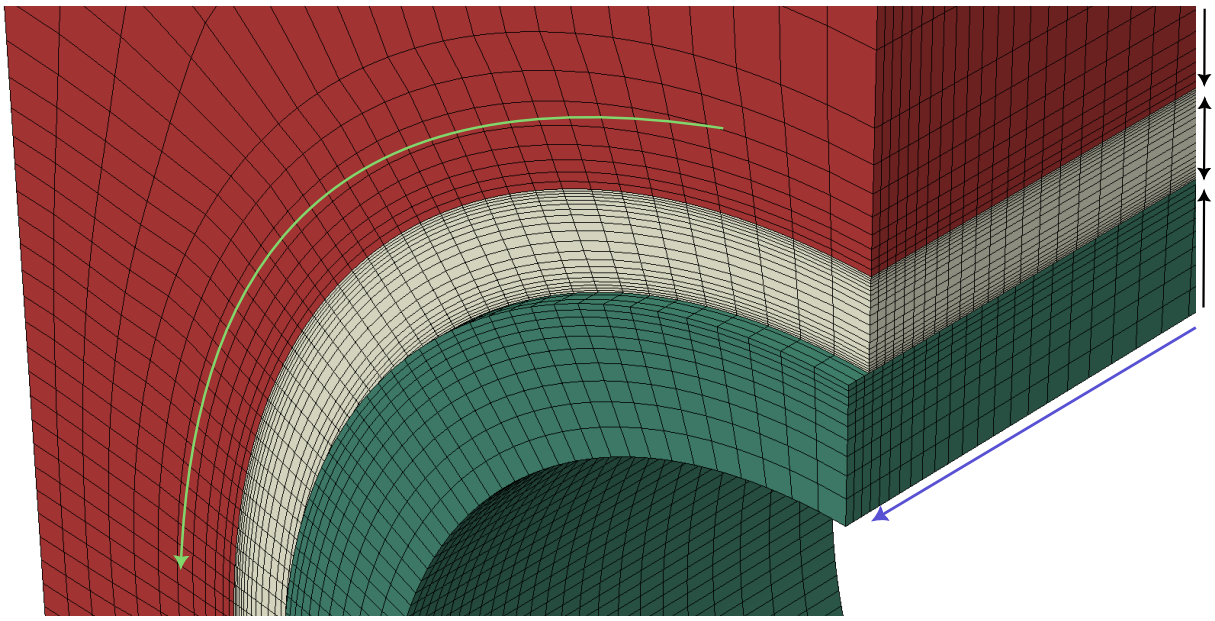

Figure 2.6: Close view of the final mesh control. The mesh has been refined towards the external face (blue), towards the center height of the hole (green) and towards the interfaces between the materials (black). Arrow heads indicate the direction of refinement.

simulate the effect of creep, Abaqus offers two possibilities, a *quasi-static* simulation or a full dynamic one. Static simulations cannot be used when creep is taken into account since creep is a time-dependent process. Normally, rate-dependent properties are taken into account in dynamic simulations. However, since creep is generally a very slow process, its instantaneous impact on the overall structure is minimal and therefore no other dynamic effects take place. For that reason, a *quasi-static* approach is also applicable. Abaqus calls this option a "Visco" step. *Quasi-static* simulations are static simulations that allow the user to control the maximum rate of change of a property, such as swelling or creep strains. These strains are capped to a maximum change by the user in order to control the time-integration error that takes place during a single time-step. In this case, the strain that needs to be controlled is creep. Normally, changes in creep strain during a single time step are set to low values, e.g. 10^{-5} as a common default. However, for the present case with creep, this value was set much higher for the sake of computational speed, this is detailed in section 2.5.4.

Model name	Formulation
Power laws	
Time hardening form	$\dot{\epsilon}^{cr} = A \cdot \tilde{\sigma}^n \cdot t^m$
Strain hardening form	$\dot{\epsilon}^{cr} = (A\tilde{\sigma}^n[(m+1)\cdot\epsilon^{cr}]^m)^{\frac{1}{m+1}}$
Double power	$\dot{\epsilon}^{cr} = A_1 \cdot e^{-\left(\frac{B_1}{T-T_Z}\right)} \cdot \left(\frac{\tilde{\sigma}}{\sigma_0}\right)^{C_1} + A_2 \cdot e^{-\left(\frac{B_2}{T-T_Z}\right)} \cdot \left(\frac{\tilde{\sigma}}{\sigma_0}\right)^{C_2}$
Hyperbolic laws	
Hyperbolic-sine	$\dot{\epsilon}^{cr} = A \cdot \sinh(B\tilde{\sigma})^n \cdot e^{-\left(\frac{Q}{\Re\cdot(T-T_Z)}\right)}$
Anand model	$\dot{\epsilon}^{cr} = A \cdot \left[\sinh\left(\xi\frac{\tilde{\sigma}}{s}\right)\right]^{\frac{1}{m}} \cdot e^{-\left(\frac{Q}{\Re\cdot(T-T_Z)}\right)}$
Darveaux model	$\dot{\epsilon}^{cr} = C_{ss} \cdot [\sinh(\alpha\tilde{\sigma})]^n \cdot e^{-\left(\frac{Q}{\Re\cdot(T-T_Z)}\right)}$

Table 2.7: Reduced selection of creep models available in Abaqus. Hyperbolic models are more widely used for fracture analysis due to their higher sensitivity to stress. Refer to Abaqus' user manual [21] for the meaning of each parameter and the full list.

2.5.1 Literature review of OFHC-Cu and CuCrZr creep

Copper and its alloys are commonly used for thermal management due to their high thermal conductivity and ductility. For this reason, copper has been subject to a large number of creep analysis. Thorough analysis of creep in copper can already be found since the middle of the 20th century. For example, the effect of crystal size on creep was studied in 1965 [13] and the impact of temperature dependence in 1990 [12]. Other research groups have also performed systematic creep analysis of copper, such as the Swedish Nuclear Fuel and Waste Management Co (SKB), which selected copper as the sealing material for long term storage of spent nuclear fuel [29]. Li, Thomas and Stubbins in [17] performed a comprehensive review of the available literature for creep of copper and its alloys in 2000, some of the reviewed literature dates from the 1950s or earlier.

Even though a lot of work was dedicated to characterizing creep in copper, the data available for the current study is lacking. This stems from the fact that focus was put on secondary creep, also known as steady state creep, which is easier to characterize and it is the most relevant, as its behavior generally covers the majority of the service life of the part. In our case, the effect of primary creep is expected to be the main driver of stress relaxation. A lot of studies also focused on the creep of specific copper alloys, which generated results that were unique to that alloy in particular. For example, Oxigen Free, Phosphorous-dopped Copper (OFP-Cu) was chosen by SKB instead of OFHC-Cu [30] as even a small amount of phosphor (>50 p.p.m) in copper substantially decreases the creep rate and enhances total creep strain before fracture [15, 31].

The review of creep in the literature is further complicated by the different creep models that were used by each author. Most creep models for copper and its alloys follow the Norton-Bailey creep rate law (or power law breakdown) with temperature dependence expressed by an Arrhenius term, as shown in Equation 2.4. The Norton-Bailey law is generally only valid for secondary creep rate, however, it can be adapted to model primary creep rates with the use of an explicit time-dependent term, as shown in Equation 2.5. Table 2.8 indicates the parameters used in the Norton-Bailey law. The time constant m is normally ranges between $-1 < m < 0$ for primary creep rate, and it is usually called *time-hardening* constant. May, Gordon and Segletes in [32] indicate the data regression process required to obtain the different creep parameters for the Norton-Bailey law.

$$\dot{\epsilon}_{sd} = A \cdot \tilde{\sigma}^n \cdot e^{-\left(\frac{E_{ac}}{\mathfrak{R} \cdot T}\right)} \tag{2.4}$$

$$\dot{\epsilon}_{pr} = A' \cdot \tilde{\sigma}^{n'} \cdot e^{-\left(\frac{E_{ac}}{\mathfrak{R} \cdot T}\right)} \cdot t^m \tag{2.5}$$

Fitting coefficient	Deviatoric stress	Stress exponent	Time constant	Activation energy for self-diffusion
A	$\tilde{\sigma}$	n	m	E_{ac}

Table 2.8: Norton-Bailey creep law parameters.

2.5.1.1 Modifications to the Norton-Bailey creep law

As previously mentioned, most creep studies for copper use the Norton-Bailey law to model creep. However, the formulation shown in Equation 2.4 is usually modified in different ways, as shown in Equation 2.6. This raises the problem where theoretically compatible formulations use widely different parameters, generally A' and n', which complicates their analysis, comparison and integration in a study. For instance,

$$\dot{\epsilon}_{sd} = A' \cdot \left(\frac{Y}{X}\right)^{n'} \cdot e^{-\left(\frac{E_{ac}}{\mathfrak{R} \cdot T}\right)} \tag{2.6a}$$

where some studies choose one of

$$Y = \tilde{\sigma} - \sigma_Y \qquad or \qquad Y = \tilde{\sigma} - \sigma_0 \\ \text{With } \sigma_0 \text{ being a threshold and } Y \geq 0 \tag{2.6b}$$

$$X = G \qquad or \qquad X = \sigma_Y \qquad or \qquad X = \sigma_0 \\ \text{With } \sigma_0 \text{ being a chosen value} \tag{2.6c}$$

2.5.1.2 Creep parameter dependence

Another area of study in creep analysis is its dependence on the different material parameters. Creep studies focus on the dependence of creep rate with respect to stress and temperature. Other factors are also known to have an effect on a material's creep, such as crystal size [13, 33], heat treatment, radiation or fatigue [34]. However, there is no agreement on the method used to identify these effects within the different creep model parameters. For example, Freed and Walker [12] studied the dependence of the E_{ac} with respect to temperature. But in order to do so, the stress exponent n was fixed to a value of 5. This opens the question whether the variability that was found in E_{ac} is due to the temperature or due to the formulation of the other parameters. Equation 2.7 shows the sensitivity of Equation 2.5 if n, m, A and E_{ac} were temperature and stress dependent. As it can be seen, it is difficult to give an explanation for the temperature and stress dependency. Therefore, most studies tend to fix n, E_{ac} or both.

$$\begin{aligned} \frac{d\dot{\epsilon}_{pr}}{dT} &= Ae^{-\frac{E_{ac}}{\Re T}}\left(\frac{\delta}{\delta T}n\right)t^m\tilde{\sigma}^n\log\left(\tilde{\sigma}\right)+ \\ &+Ae^{-\frac{E_{ac}}{\Re T}}\left(\frac{\delta}{\delta T}m\right)t^m\log\left(t\right)\tilde{\sigma}^n+ \\ &+A\left(\frac{E_{ac}}{\Re T^2}-\frac{\left(\frac{\delta}{\delta T}E_{ac}\right)}{\Re T}\right)e^{-\frac{E_{ac}}{\Re T}}t^m\tilde{\sigma}^n+ \\ &+\left(\frac{\delta}{\delta T}A\right)e^{-\frac{E_{ac}}{\Re T}}t^m\tilde{\sigma}^n \end{aligned} \tag{2.7a}$$

$$\begin{aligned} \frac{d\dot{\epsilon}_{pr}}{d\tilde{\sigma}} &= Ae^{-\frac{E_{ac}}{\Re T}}t^m\tilde{\sigma}^n\left(\left(\frac{\delta}{\delta\tilde{\sigma}}n\right)\log\left(\tilde{\sigma}\right)+\frac{n}{\tilde{\sigma}}\right)+ \\ &+Ae^{-\frac{E_{ac}}{\Re T}}\left(\frac{\delta}{\delta\tilde{\sigma}}m\right)t^m\log\left(t\right)\tilde{\sigma}^n- \\ &-\frac{A\left(\frac{\delta}{\delta\tilde{\sigma}}E_{ac}\right)e^{-\frac{E_{ac}}{\Re T}}t^m\tilde{\sigma}^n}{\Re T}+ \\ &+\left(\frac{\delta}{\delta\tilde{\sigma}}A\right)e^{-\frac{E_{ac}}{\Re T}}t^m\tilde{\sigma}^n \end{aligned} \tag{2.7b}$$

2.5.1.3 A word on non-parametric creep models

In the last few decades, more advanced creep models have been formulated based on dislocation theory [35]. These models have shown good flexibility and accuracy [36]. They also present the advantage of not requiring traditional creep tests and fitting a model to the data of these tests, which is very time consuming and specific to the material tested. Non-parametric formulation of creep models focus on the atomistic behavior of the crystal, which requires the precise measurement of some of its parameters, such as the Taylor coefficient and vacancy density. This can be a complex requirement and its applicability may be challenging for more general cases. For these reasons, it was decided to not use non-parametric models in this study.

2.5.1.4 Validity range of creep models

Another issue of the current "state-of-the-art" of creep models for OFHC-Cu and CuCrZr is the limited range of temperatures and stresses for which the models are applicable. Most studies have focused on temperatures greater than half the melting point [37]. Others have focused on much lower temperatures, as copper can creep at high stresses even if it is at lower temperatures, well below half the melting point [31]. However, no single model exists that encompasses the wide temperature and stress ranges that have been studied, including the relevant range for the present study.

2.5.2 Choice of a creep law

After a review of the different creep models available for OFHC-Cu and CuCrZr, it was decided that only secondary creep for OFHC-Cu be modeled. The quality of the models available for CuCrZr-IG in [17] is questioned by the author, as they either produce extremely high creep rates (most likely due to an incorrect copy of the parameters) or their validity range is completely outside of the current study. As there are no primary creep models for OFHC-Cu, only the secondary creep model was chosen from [17]. The expression in Equation 2.8 is the same as Equation 2.4 with $A = 38.8\,\mathrm{MPa}^{-n}\mathrm{s}^{-m-1}$, $E_{ac} = 197\,\mathrm{kJ\,mol}^{-1}$ and $n = 4.8$.

$$\begin{gathered}\dot{\epsilon}^{cr} = \dot{\epsilon}_{sd} = 38.8 \cdot \tilde{\sigma}^{4.8} \cdot e^{-\dfrac{197\,000}{\mathfrak{R} \cdot T_{abs}}} \\ \frac{\delta \dot{\epsilon}^{cr}}{\delta \tilde{\sigma}} = 38.8 \cdot 4.8 \cdot \tilde{\sigma}^{3.8} \cdot e^{-\dfrac{197\,000}{\mathfrak{R} \cdot T_{abs}}} \\ 400\,^{\circ}\mathrm{C} \leq T \leq 700\,^{\circ}\mathrm{C} \\ 15\,\mathrm{MPa} \leq \tilde{\sigma} \leq 105\,\mathrm{MPa}\end{gathered} \tag{2.8}$$

This expression was also chosen with the expectation that in the future, once primary creep data is available, the *time-hardening* constant m as shown in Equation 2.5, could be fitted, allowing the full modeling of primary and secondary creep. Section 2.5.3 discusses how the coupling between primary and secondary creep could be performed. Section 2.5.4 documents the implementation details of this law in Abaqus and performs some visualization and sensibility analysis.

2.5.2.1 Visualization of the creep model

In order to support the analysis of creep, a set of visualizations and sensitivity studies were performed. Figure 2.7 displays the creep rate produced for the selected temperature and stress range. The selected range covers the temperature and stresses which take place during the cooldown of the monoblock in the copper interlayer. Figure 2.8 shows the same information but projected for each input. As it can be seen and as would be expected from Equation 2.8, the selected model is much more sensitive to temperature than to stresses. Overall, the model produces an extremely broad creep rate depending on the inputs. These visualizations further manifest the large sensitivity that the Norton-Bailey model has to its inputs. Further results and analysis are included in chapter 4.

2.5.3 Coupling between primary and secondary creep

If primary and secondary creep were to be taken into account, the modeling of the transition can be approached in several ways. The most simple approximation, which is also computationally stable as it does not present a discontinuity of the creep strain derivative with respect to stress, would be to add primary and secondary creep strain rates as shown in Equation 2.9.

$$\dot{\epsilon}^{cr} = \dot{\epsilon}_{pr} + \dot{\epsilon}_{sd} \tag{2.9a}$$

$$\epsilon^{cr} = \int \dot{\epsilon}^{cr} \cdot dt \tag{2.9b}$$

$$\frac{\delta \epsilon^{cr}}{\delta \tilde{\sigma}} = \frac{\delta \epsilon_{pr}}{\delta \tilde{\sigma}} + \frac{\delta \epsilon_{sc}}{\delta \tilde{\sigma}} \tag{2.9c}$$

with

$$\lim_{t \to 0} \ \dot{\epsilon}^{cr} \approx \dot{\epsilon}_{pr} \longleftarrow \dot{\epsilon}_{pr} \gg \dot{\epsilon}_{sd} \tag{2.9d}$$

$$\lim_{t \to \infty} \ \dot{\epsilon}^{cr} \approx \dot{\epsilon}_{sd} \longleftarrow \dot{\epsilon}_{pr} = 0 \tag{2.9e}$$

This approach overestimates creep strain as it adds secondary creep strain already from the beginning of the analysis and the decaying primary creep is considered for the entire analysis, whether applicable or not. However, as indicated in Equation 2.9d, this approximation should be valid as primary creep rate is generally much greater than secondary at the beginning of creep and it decreases rapidly with time. This approach is similar to the one used by the θ, ϕ and Ω creep models [15].

Another approach to couple primary and secondary creep strains would be to define total creep strain as function defined by parts as shown in Equation 2.10. Expressing creep strain by parts, presents different possibilities and it is flexible in its formulation with respect to the different parameters that can be used to drive the coupling between expressions. It would also allow the correct estimation of creep. However, the creep strain derivative with respect to the deviatoric stress could see a jump which can make the simulation unstable, as this derivative is used as part of iterative methods. An example of the possible jump in the derivative is shown in Algorithm 1 for Equation 2.10d.

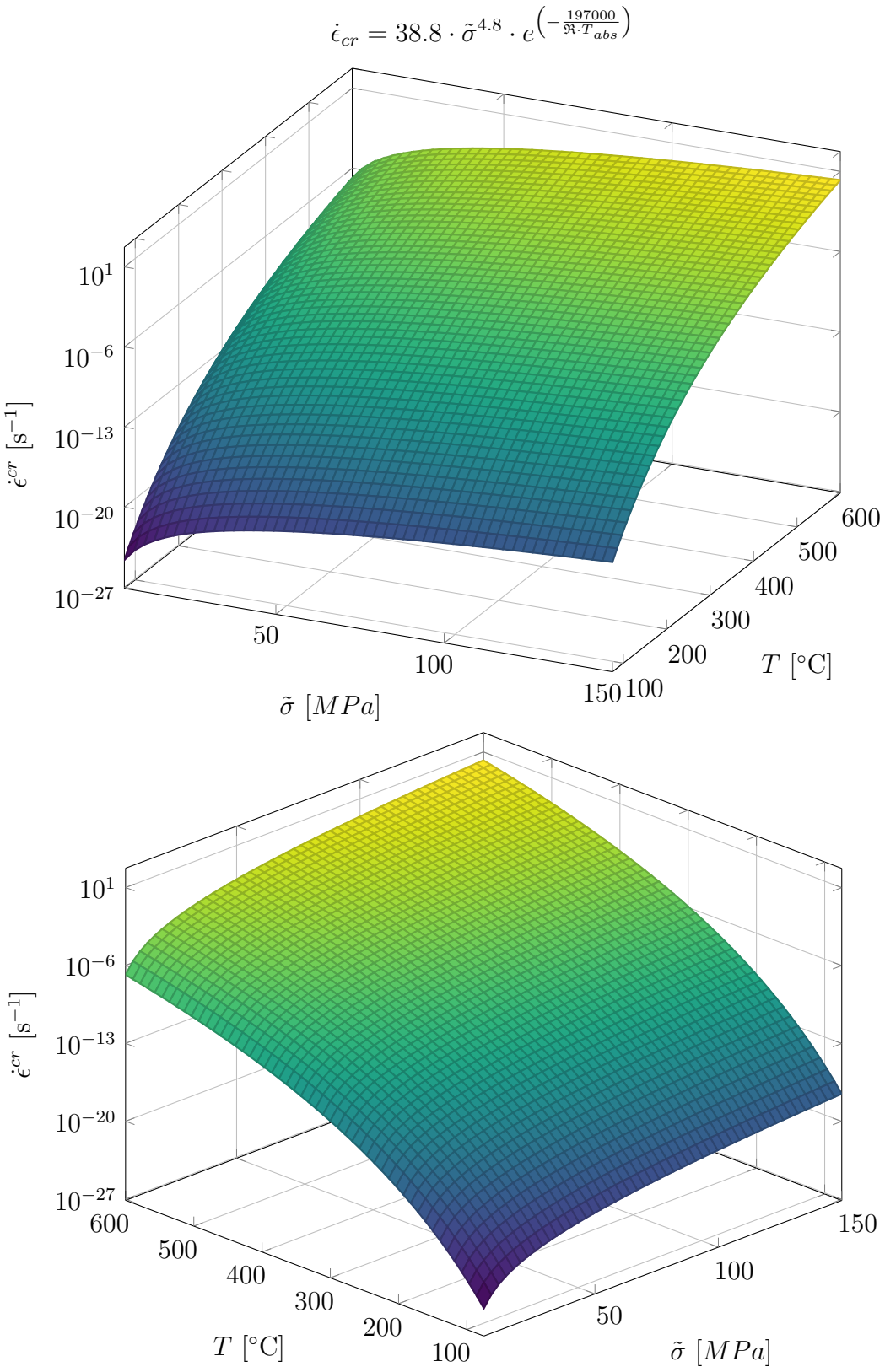

Figure 2.7: Visualization of the selected creep rate law, logarithmic scale.

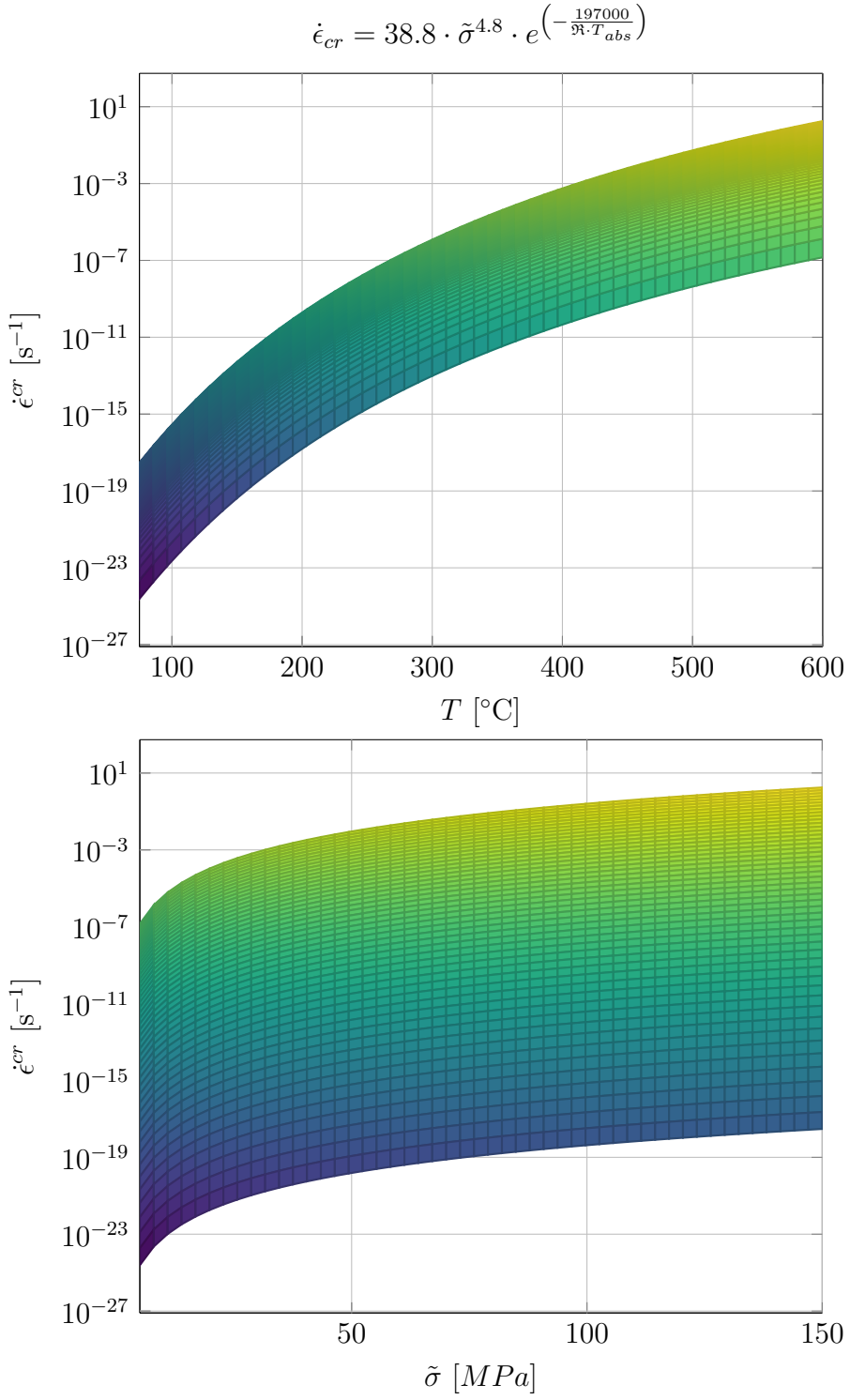

Figure 2.8: Visualization of the selected creep rate law, with respect to temperature and stress.

$$\dot{\epsilon}^{cr} = \begin{cases} \dot{\epsilon}_{pr} & for \quad \epsilon^{cr} < \epsilon^*(\tilde{\sigma}, T) \\ \dot{\epsilon}_{sd} & for \quad \epsilon^{cr} \geq \epsilon^*(\tilde{\sigma}, T) \end{cases} \tag{2.10a}$$

$\epsilon^*(\tilde{\sigma}, T)$ being given by the model

or

$$\dot{\epsilon}^{cr} = \begin{cases} \dot{\epsilon}_{pr} & for \quad t < t^*(\tilde{\sigma}, T) \\ \dot{\epsilon}_{sd} & for \quad t \geq t^*(\tilde{\sigma}, T) \end{cases} \tag{2.10b}$$

$t^*(\tilde{\sigma}, T)$ being given by the model

or

$$\dot{\epsilon}^{cr} = \begin{cases} \dot{\epsilon}_{pr} & for \quad \epsilon_{sc} < \epsilon_{pr} \\ \dot{\epsilon}_{sd} & for \quad \epsilon_{sc} \geq \epsilon_{pr} \end{cases} \tag{2.10c}$$

or

$$\dot{\epsilon}^{cr} = \begin{cases} \dot{\epsilon}_{pr} & for \quad \dot{\epsilon}_{sd} < \dot{\epsilon}_{pr} \\ \dot{\epsilon}_{sd} & for \quad \dot{\epsilon}_{sd} \geq \dot{\epsilon}_{pr} \end{cases} \tag{2.10d}$$

with

$$\epsilon_{sc} = \int \dot{\epsilon}_{sd} \cdot dt \tag{2.10e}$$

$$\epsilon_{pr} = \int \dot{\epsilon}_{pr} \cdot dt \tag{2.10f}$$

$$\epsilon^{cr} = \int \dot{\epsilon}^{cr} \cdot dt \tag{2.10g}$$

For example, in Table II. of [17] the coupling of the primary creep law with the secondary creep for CuCrZr uses the formulation indicated in Equation 2.10c.

2.5.4 Implementation of the creep law

The secondary creep law as indicated in Equation 2.8 was implemented using Abaqus' `CREEP` subroutine, which is included in Appendix B. This subroutine is designed to allow the user the arbitrary definition of creep and swelling models. Equation 2.8 could have been modeled using the "Double power" creep law built into Abaqus as shown in Table 2.7. However, the use of the `CREEP` subroutine is more flexible and can be adapted in the future to account for primary creep effects, which could be coupled as explained in subsection 2.5.3.

In Abaqus, creep was considered for the OFHC-Cu material and the user `CREEP` subroutine was selected as the model. If creep of different materials is to be modeled, refer to Listing B.2 as an example on how to set up the subroutine. For the quasi-static simulation, the maximum increment in ϵ^{cr} allowed was 10^{-3}. This value can be seen high, as that would be equivalent to 0.1 % of strain increase just due to creep in a single time-step. However, this high value was needed as the interfaces between the copper interlayer and

Algorithm 1: Example of a potential instability in the calculation of creep.

Data: `CREEP` input parameters, including Δt for the current time-step n
Result: Calculate the $\Delta\epsilon^{cr}$ for the given time-step
begin
  if $\dot{\epsilon}_{pr}(\tilde{\sigma}_n, T_n, t) > \dot{\epsilon}_{sd}(\tilde{\sigma}_n, T_n)$ **then**
    $\Delta\epsilon^{cr} := \dot{\epsilon}_{pr} \cdot \Delta t_n$
    $\frac{\delta\epsilon^{cr}}{\delta\tilde{\sigma}} := \frac{\delta\epsilon_{pr}}{\delta\tilde{\sigma}}$ /* $\epsilon_{pr} = \dot{\epsilon}_{pr} \cdot \Delta t$ */
  else
    $\Delta\epsilon^{cr} := \dot{\epsilon}_{sd} \cdot \Delta t_n$
    $\frac{\delta\epsilon^{cr}}{\delta\tilde{\sigma}} := \frac{\delta\epsilon_{sc}}{\delta\tilde{\sigma}}$ /* $\epsilon_{sc} = \dot{\epsilon}_{sd} \cdot \Delta t$ */
  end
  /* $\frac{\delta\epsilon^{cr}}{\delta\tilde{\sigma}}$ could have a jump when the condition changes. This could make the simulation unstable. However, a small value of Δt should prevent it. */
end

the other materials are numerically complex areas that can cause locally high stresses, and therefore high creep strain, due to singularities. A localized singularity could surpass a low allowable increment of creep strain and it would require the time-step to be reduced, making creep simulations extremely expensive to compute. For example, the simulated cooldown with creep enabled took 716 h of CPU time, while the same simulation without creep only required 34.5 h. The large increase in time was due to the maximum allowed creep strain increment and the increase in iterations per time-step required to achieve numerical convergence.

2.6 Data processing

In order to analyze the output of the simulations and create approximations for the effect of creep, an analysis platform was developed. The code used to carry out the computations is given in Appendix C. The platform has been designed with the following capabilities:

- Given the stress and temperature history as inputs, calculate the creep rate and creep strain for the selected creep rate law.
- Given a set of parameters for a creep rate expression, compute the accumulated creep strain as a function of the expression's parameters.
- Output the data for visualization purposes. Both 2D and 3D data can be generated.
- Be reasonably fast. Due to the large number of computations needed, specifically during parametric studies, the code has to run in a reasonable time. The main technique used to improve the performance is to use pre-allocation of memory.

The data consumed by the program has to follow a specific format, indicated in the comments in the code. However, any modern tool that can work with tabulated data can easily output the required format. The author recommends using the Excel plug-in utility from Abaqus to output the required results and use a spread-sheet program to clean the data. The results of the computations performed by the program can be seen in Figure 4.11 and 4.10.

Chapter 3

Cutting operation and residual stress analysis

In order to carry out residual stress measurements after HRP, each monoblock had to be taken out of the assembly. This required the cutting of the CuCrZr pipe at the gap between each monoblock. A second cutting operation was needed, due to the limited volume available for samples of the machine that is used to carry out the FIB–DIC tests. It was decided that the monoblock would be cut in two as shown in Figure 3.1. This would allow the top section to fit in the machine. However, cutting the part means that the geometry changes and therefore, internal stresses will have to adapt in order to find a new equilibrium in the sectioned part. This entails that the residual stresses measured by the machine will be different to the ones the part actually has after it has been produced. For this reason both cutting operations had to be simulated in order to understand how the stresses in the monoblock change from their original state.

The FIB operations rely on the focused erosion of the material using an ion beam which leaves a microscopic pillar inside the eroded area. As the erosion takes place, the pillar will experience stress changes and its free face will displace accordingly. The DIC process measures the movement of the pillar's face and correlates it to the stress state that was previously present in the part. For more information on FIB–DIC, refer to [38–40].

3.1 Implementation of the cutting operations

As shown in Table 2.1 two simulation steps take place after the cooldown. The first of those steps is the cutting of the individual monoblocks from the assembly. The operation slices the CuCrZr pipe at the gap between the monoblocks. The cutting of the CuCrZr pipe has been modeled by deactivating the planar boundary condition to allow the unconstrained movement of the nodes on the free surface being created, which models the behavior of free surfaces. However, deactivating the planar boundary condition is not supported by Abaqus. The solution used to overcome this limitation is explained in subsection 3.2.1.

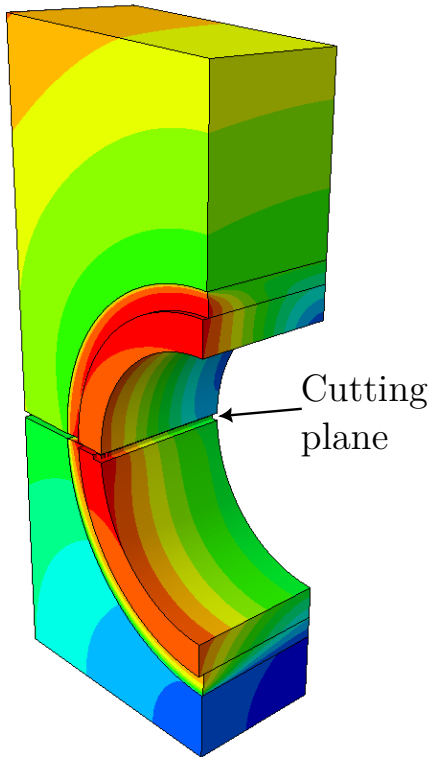

Figure 3.1: Horizontal cut of the monoblock.

3.1.1 Arbitrary element deletion, cutting of parts

The second operation is the cutting of the part horizontally, as shown in Figure 3.1. In order to perform this simulation, a Fortran `USDFLD` subroutine had to be developed which allowed the simulation of element deletion. The code for the subroutine and its technical documentation can be found at appendix B. The general algorithm used is shown in Algorithm 2. This logic can be applied to any geometrical shape that can be modeled in code. For the present study, the main cutting operation is the one shown in Figure 3.1, however, the subroutine was also used to simulate a mock-up in a FIB–DIC operation. As the FIB–DIC requires a more complex setup compared to the cutting operation shown in Figure 3.1, it is explained in detail in Algorithm 3 and Figure 3.2. Algorithm 3 has the limitation that the axis of the cylinder is also defined by the displacement vector. The algorithm could be generalized for the cases where this condition is not valid. However, the complexity of the code would increase and performance would decrease, which was not desired. The results of the FIB–DIC mock-up simulation are shown in subsection 4.2.3.

Algorithm 2: Core logic used for the element deletion subroutine.

Data: `USDFLD` input parameters, including field and time data
Result: Set the field and state to deleted if required
$\Omega \longleftarrow$ Initialize geometrical parameters
$\Omega^* \longleftarrow$ Update geometrical definition with the current simulation time
if *Gauss element* $\in \Omega^*$ **then**
    Field := 0 `/* Disable element */`
    State := 0 `/* Set state to deleted */`
end

3.2 Limitations (and recommendations) of the cutting operations

3.2.1 Limitations of the "plane remains plane" BC

There is a limitation in Abaqus where interactions and constrains cannot be deactivated from step to step, they can only be modified. This presents a problem when dealing with the cutting operations as the planar BC, which uses interaction properties, needs to be deactivated.

The methodology used to overcome Abaqus' limitation is to perform a two-stage simulation. The second stage regenerates the case by importing the geometry from the first stage and all of its results, such as stresses, deformation and hardening fields. The use of a restart file is mandatory in the last step of the first stage as the results need to be projected into the second stage and this can only be done in its entirety using restart files. More information about the procedure and its limitations is given by the `*IMPORT` keyword and "About transferring results between Abaqus analyses" section in Abaqus' user guide [21]. Due to the complex setup needed, only the simulated case without creep was chosen for the cutting operations.

3.2.2 Numerical instabilities during element deletion

Due to the high stress concentration that takes place during the cutting process, convergence of the solution becomes slow. Coupled to the large stress changes that take place every time a row of elements is deleted, the time-stepping algorithm has difficulties converging. For that reason, automatic time-stepping is recommended, as it allows the solver to reduce or increase the simulation time-step depending on the convergence speed of each time-step. For the cutting operation the time-stepping algorithm has to reduce the time-step greatly before a new row of elements is deleted. Once the row of elements is removed, the simulation has no other calculations to do up until the next row of elements is deleted. For that reason the convergence of the time-steps after elements are deleted is very quick and the adaptive time-stepping algorithm starts increasing the time-step.

For these reasons, there is an increase of time-step after a deletion and a reduction before the next deletion takes place. This cyclic behavior makes the simulation of the

Algorithm 3: Full logic used for the FIB–DIC element deletion operation. The algorithm assumes the cylinder axis is the same as the displacement vector.

Data: `USDFLD` input parameters, including field and time ($0 < t \leq 1$) data
Result: Set the field and state to deleted if required

```
/* See Figure 3.2 for a geometrical description of the algorithm        */
/* Define geometrical parameters                                        */
begin
    /* User defined parameters                                          */
    r_i := r_i                                          /* Inner radius */
    r_o := r_o                                          /* Outer radius */
    C⃗ := {C_x, C_y, C_z}                              /* Cylinder center */
    V⃗ := {V_x, V_y, V_z}                    /* Unit displacement vector */
    /* Gauss element position, input from Abaqus                        */
    G⃗ := {G_x, G_y, G_z}
    /* Computed location of cylinder at step time t_n                   */
    C⃗* := C⃗ + V⃗ · t_n
end
 /* Compute intersection of Gauss elements and geometry                 */
begin
    /* Element distance from the center                                 */
    D⃗ := G⃗ − C⃗*
    /* Project distance over to the displacement vector                 */
    m := D⃗ · V⃗
    /* Check if the element is behind the advancing front               */
    if m ≤ 0.0 then
        /* Distance from G⃗ to the cylinder axis                         */
        d := ‖D⃗ − m · V⃗‖
        /* Check if the Gauss element is between the radii              */
        if d ≤ r_o ∧ d ≥ r_i then
            Field_G := 0                                /* Disable element */
            State_G := 0                          /* Set state to deleted */
        end
    end
end
```

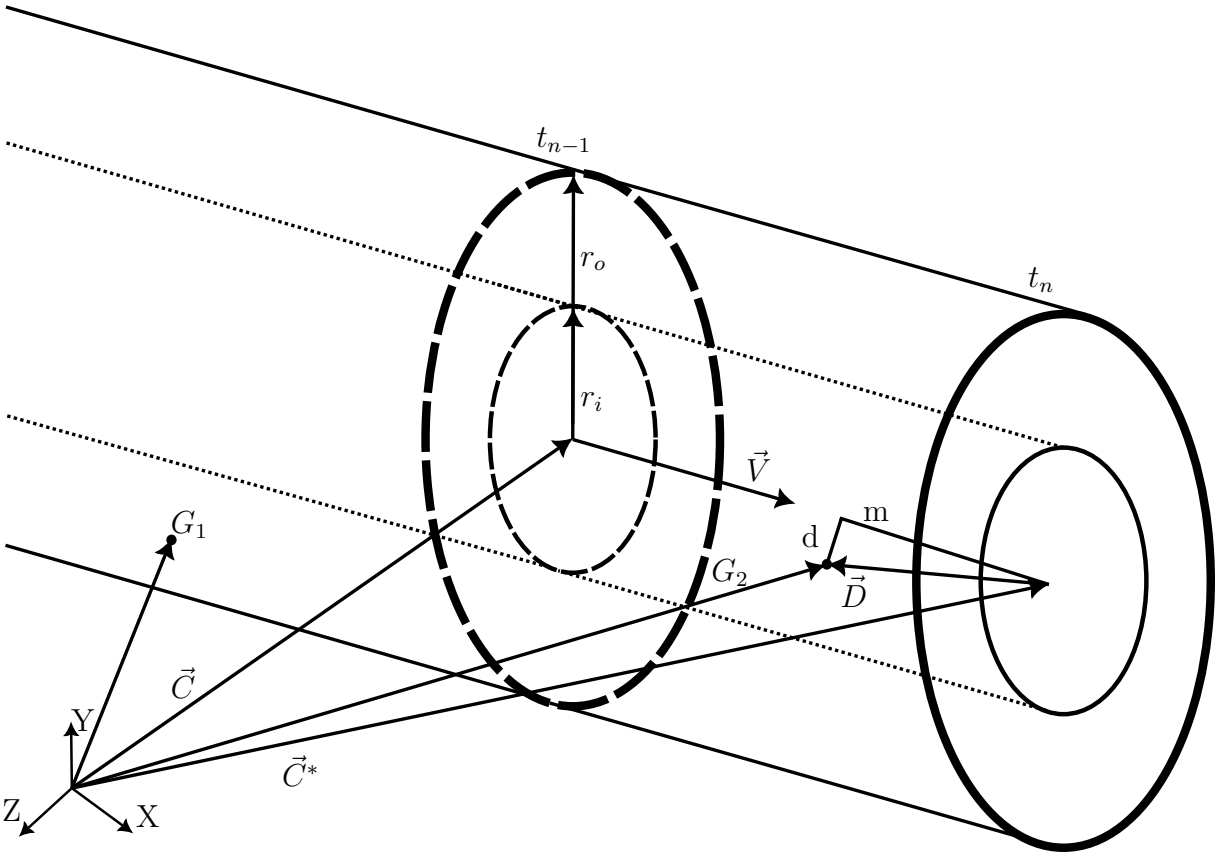

Figure 3.2: Geometry description for element deletion in a FIB–DIC case. In this example, G_2 would be considered outside of the geometry as its distance to the axis is smaller than r_i. G_1 is within r_i and r_o and behind $\vec{C}^*$ as $m \leq 0.0$, so it would have been deleted. We simplify the problem by assuming the cylinder's axis is the same as the displacement vector.

cutting process extremely slow. The algorithm cannot predict the optimal time-step and it has to do several reduction cycles before it is able to converge when a row of elements is deleted, which is computationally expensive. Afterwards the simulation advances slowly as the increase of time-step is done incrementally. This cyclic behavior means the FEM program spends most of the time for adapting the time-step rather than for carrying out the simulation. A fixed time-step is not recommended since the simulation is likely to fail to converge at a given point and a reduction of time-step would be necessary.

Chapter 4

Results

4.1 Residual stress analysis, viscoplastic stress relaxation

The results of the simulation without creep are shown in Figure 4.1, the results with creep in Figure 4.2. The stress profiles indicated in Figure 4.3 are plotted for both simulations in Figure 4.4. The results from the selected stress profiles indicate that the model with creep generates the same stress distribution as the model without creep. This would indicate that the selected secondary creep model does not have an impact on the residual stresses after the production of the part.

Another simulation was performed where the creep stress exponent n from Equation 2.8 was set to 7. The value of 7 is generally discussed in the literature as an upper limit for the stress exponent during secondary creep. Due to the higher sensitivity the creep model has to $\tilde{\sigma}$ with a higher stress exponent, the convergence was much slower and the time-steps required were also smaller. Therefore, the simulation of this new case took substantially longer, 4421 CPU hours.

A more thorough analysis was performed taking six control elements. Three elements were selected in the internal symmetry BC face and three were chosen close to the external face of the monoblock. The selected control elements are indicated in Figure 4.3. The Mises and hoop stresses were plotted for each element and for each case: without creep, with creep and creep with a higher stress exponent. The results are shown in Figure 4.5, 4.6, 4.7 and 4.8.

The results indicate that the impact of creep does not have a material change in the residual stresses of the monoblock. Nonetheless, the area most highly affected is the copper interlayer close to the external face of the monoblock. It is worth noting that the copper interlayer close to the symmetry BC face sees a substantial stress relaxation at the beginning of the cooling process, but as the temperature drops, the stresses build up to the same value as the model without creep.

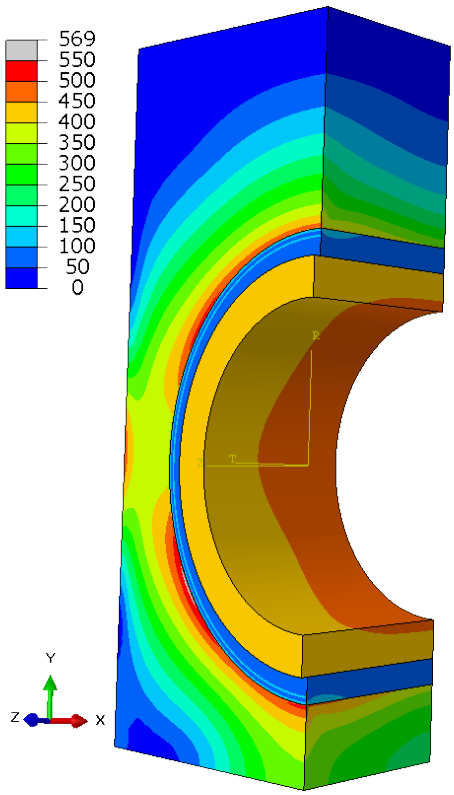

(a) Mises stresses.

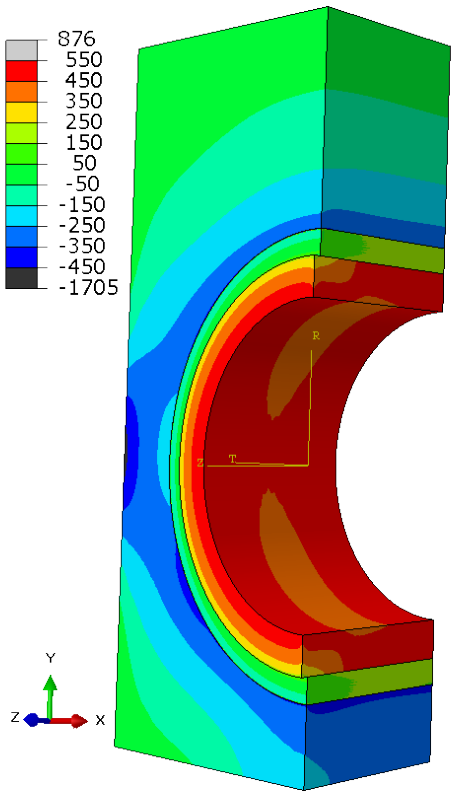

(b) Hoop stresses.

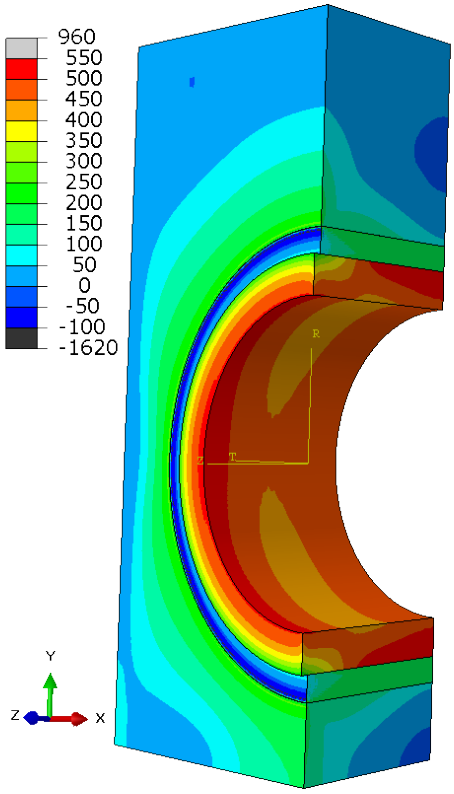

(c) Maximum principal component.

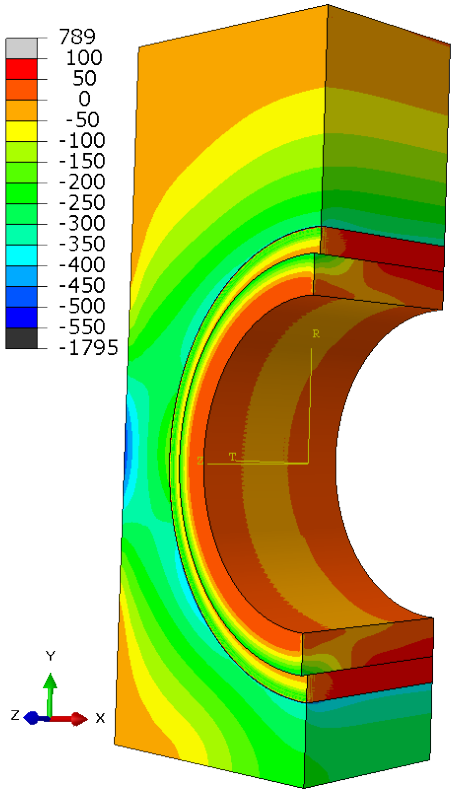

(d) Minimum principal component.

Figure 4.1: Stress distribution of the monoblock after cooldown without creep enabled.

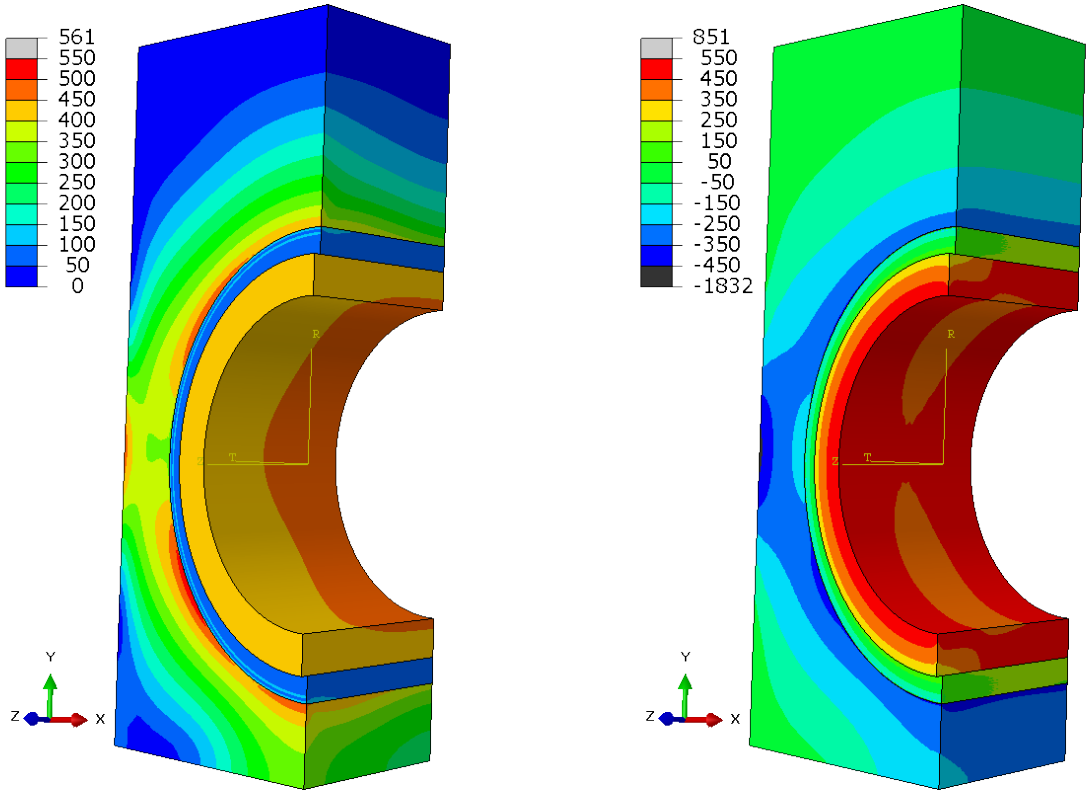

(a) Mises stresses.

(b) Hoop stresses.

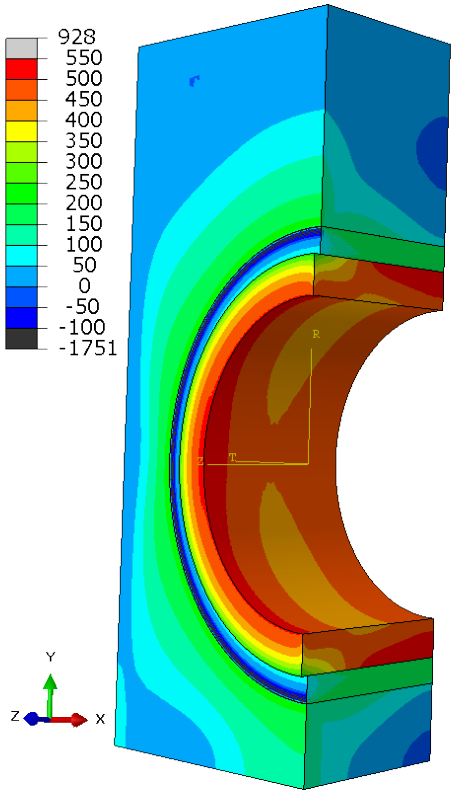

(c) Maximum principal component.

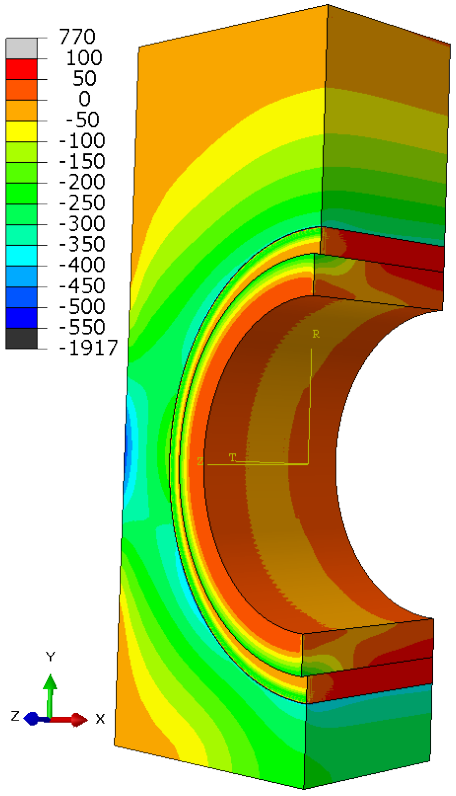

(d) Minimum principal component.

Figure 4.2: Stress distribution of the monoblock after cooldown with creep enabled in OFHC-Cu.

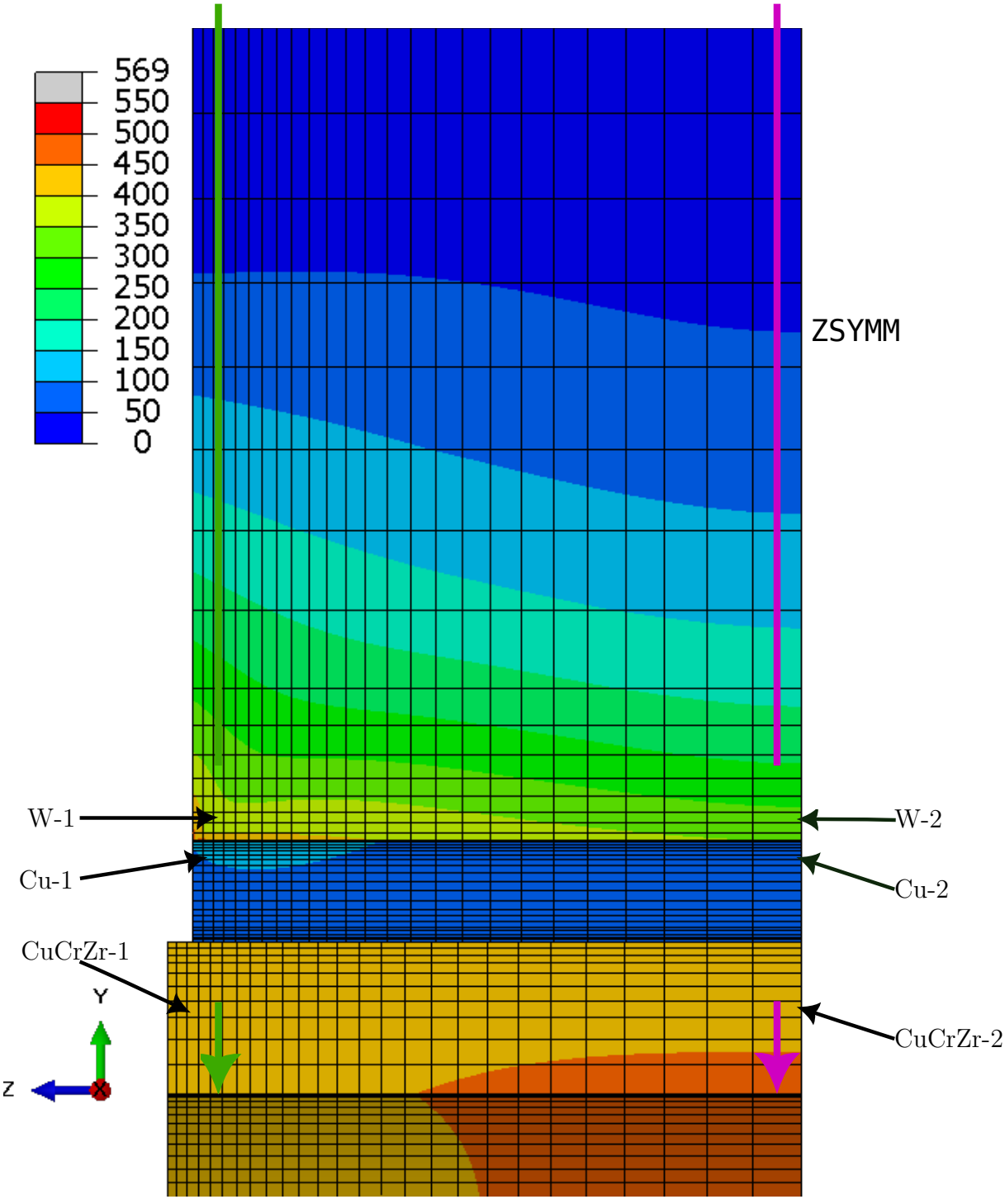

Figure 4.3: Side view of the monoblock with the mesh overlay and Mises stress. The arrows point to the selected elements which are analyzed in Figure 4.5 and 4.6.

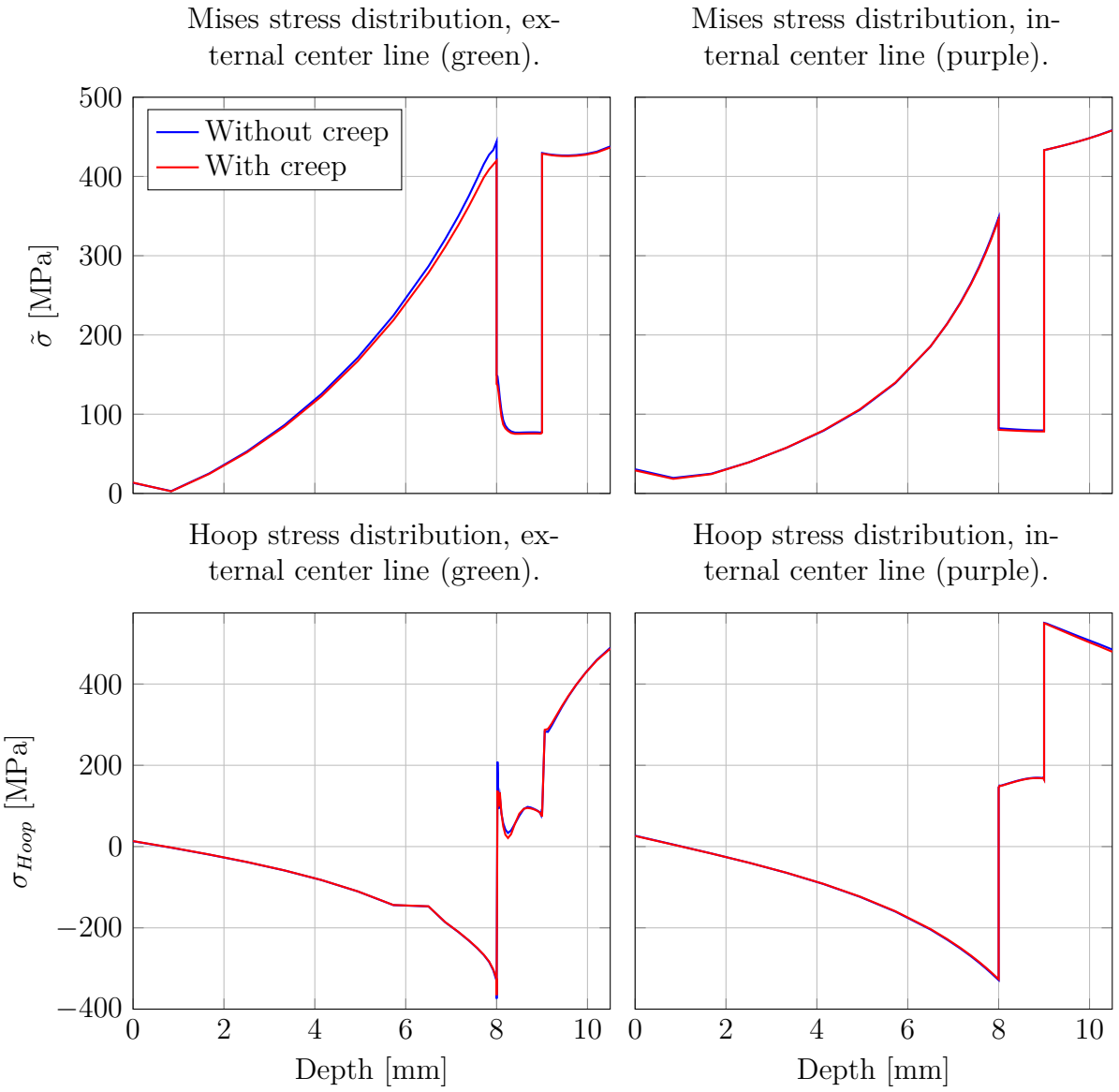

Figure 4.4: Mises and hoop stress comparison between the model without creep and the one with creep in OFHC-Cu. The external and internal profiles plotted are indicated in Figure 4.3 (green and purple arrows).

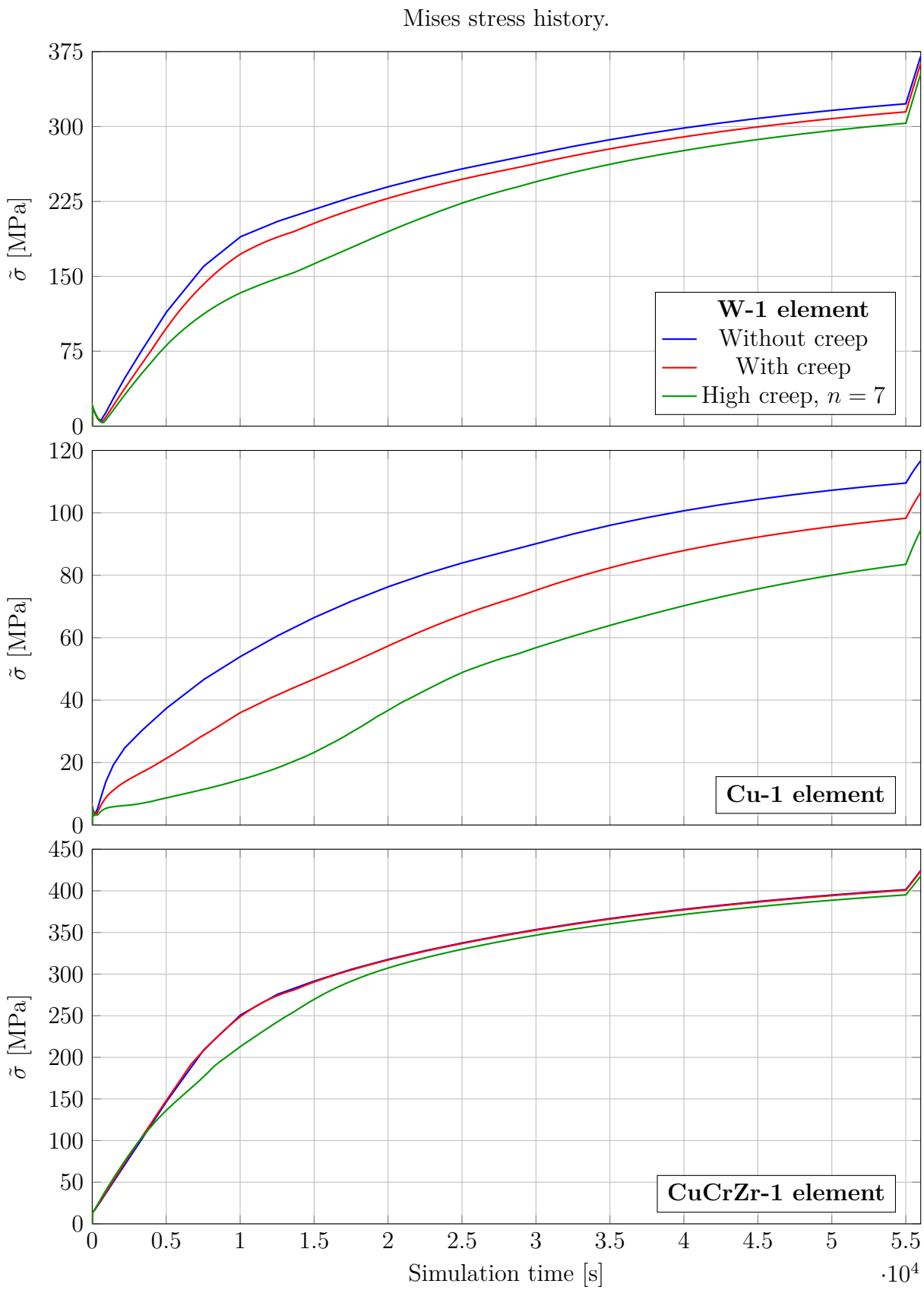

Figure 4.5: Stress history of the selected external elements with and without creep enabled. The hexahedra referred in these plots are shown in Figure 4.3.

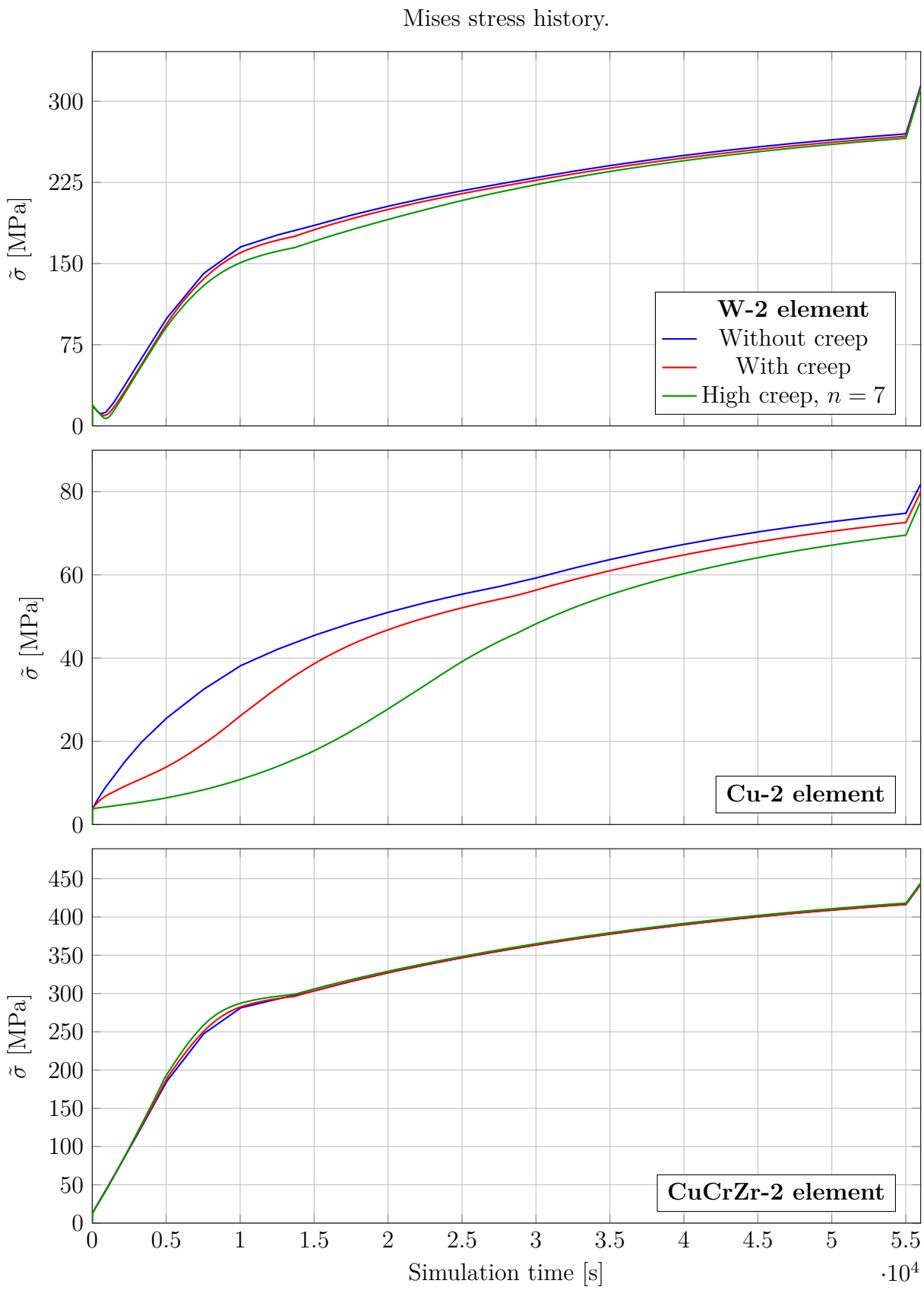

Figure 4.6: Stress history of the selected internal elements with and without creep enabled. The hexahedra referred in these plots are shown in Figure 4.3.

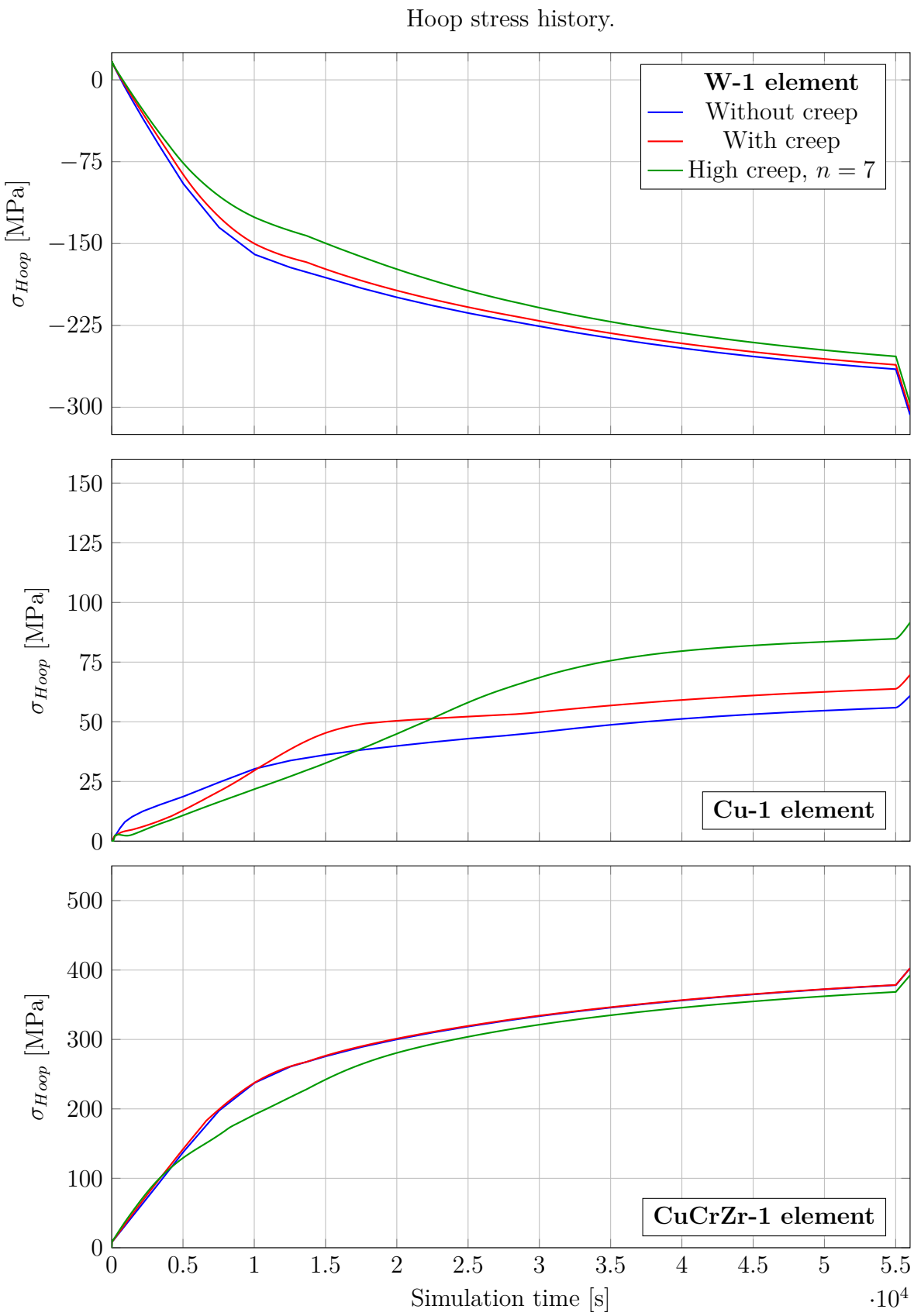

Figure 4.7: Hoop stress history of the selected external elements with and without creep enabled. The hexahedra referred in these plots are shown in Figure 4.3.

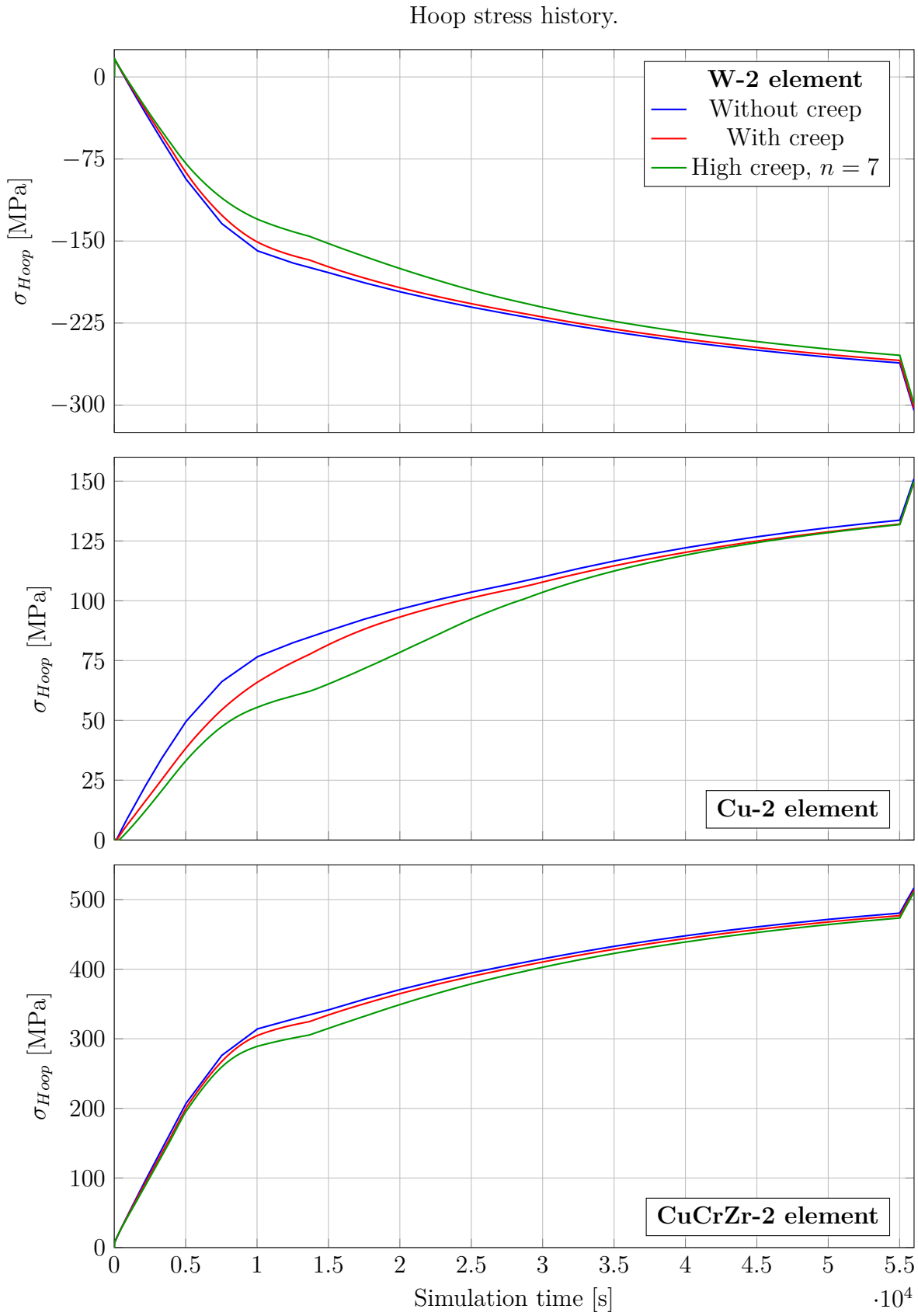

Figure 4.8: Hoop stress history of the selected internal elements with and without creep enabled. The hexahedra referred in these plots are shown in Figure 4.3.

4.1.1 Creep strain and its analytical approximation

The inelastic strain, ϵ^{in}, that the copper interlayer experiences can be divided in two components: plastic strain, ϵ^{pl} and creep strain, ϵ^{cr}. Figure 4.9 compares the strain evolution of the respective components for the three simulated cases. The increase of creep strain (`CEEQ`) takes place at the beginning of the simulation, while the temperature of the part is still high; afterwards, it remains constant. The plastic strain (`PEEQ`) starts to increase more steeply once the creep strain reaches a stable value.

With the stress history generated from the FEM simulation without creep, a simplified analytical approximation can be performed. Using the stress and temperature histories, the creep rate can be computed for the selected creep model. Integrating the creep strain rate over time, we obtain the accumulated creep strain. This process is visualized in Figure 4.10. This technique, however, is a simple analytical approximation. The calculated creep strain was decoupled with the stress history, meaning that there is no stress relaxation effect. For this reason, the expected accumulated creep strain was expected to be higher than the one calculated using FEM, as the FEM program is able to couple viscous effects to the calculated stresses. This assumption is confirmed in Figure 4.11, which compares the expected creep as simulated by the FEM program when creep is taken into account (blue line) and the analytical approximation (red line). The resulting analytical creep strain is nearly an order of magnitude greater than the creep strain calculated in the FEM simulation.

As an interesting thought experiment, another analytical computation was performed. This time, the stress history used was taken from the FEM simulation with creep enabled. The results from this new computation are included in Figure 4.11 (green line). It was expected that the analytical approximation would generate the same results as the FEM computation. The stress and temperature inputs are the same in the analytical model and the FEM simulation, with both cases using the same creep model. However, the resulting analytical creep strain is not the same as the one in the FEM simulation. There is no clear explanation for this discrepancy. However, a potential reason is proposed. The FEM program updates the stress results once it achieves convergence for a given time-step, but it does not update the expected creep strain in the last iteration. This may produce a small discrepancy between the stresses and the expected creep strain increment for those stresses. Due to the high sensitivity the creep model has to stresses, it can be possible that the error is accumulated during integration in the analytical approximation and therefore a discrepancy appears. Figure 4.12 shows in more detail this discrepancy for the simulation with a higher creep exponent.

Equivalent creep strain (CEEQ) in comparison with equivalent plastic strain (PEEQ).

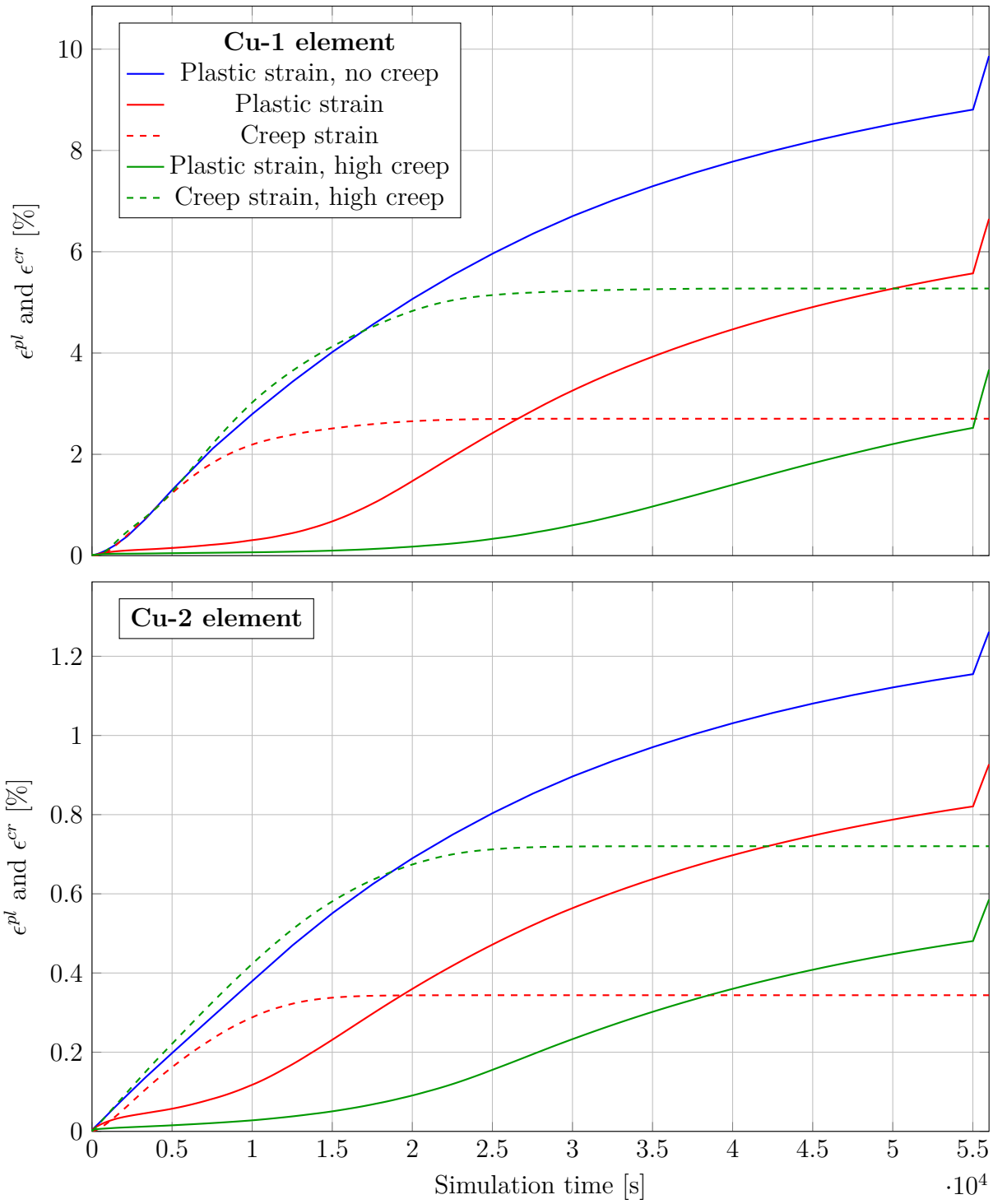

Figure 4.9: Equivalent creep strain compared to equivalent plastic strain.

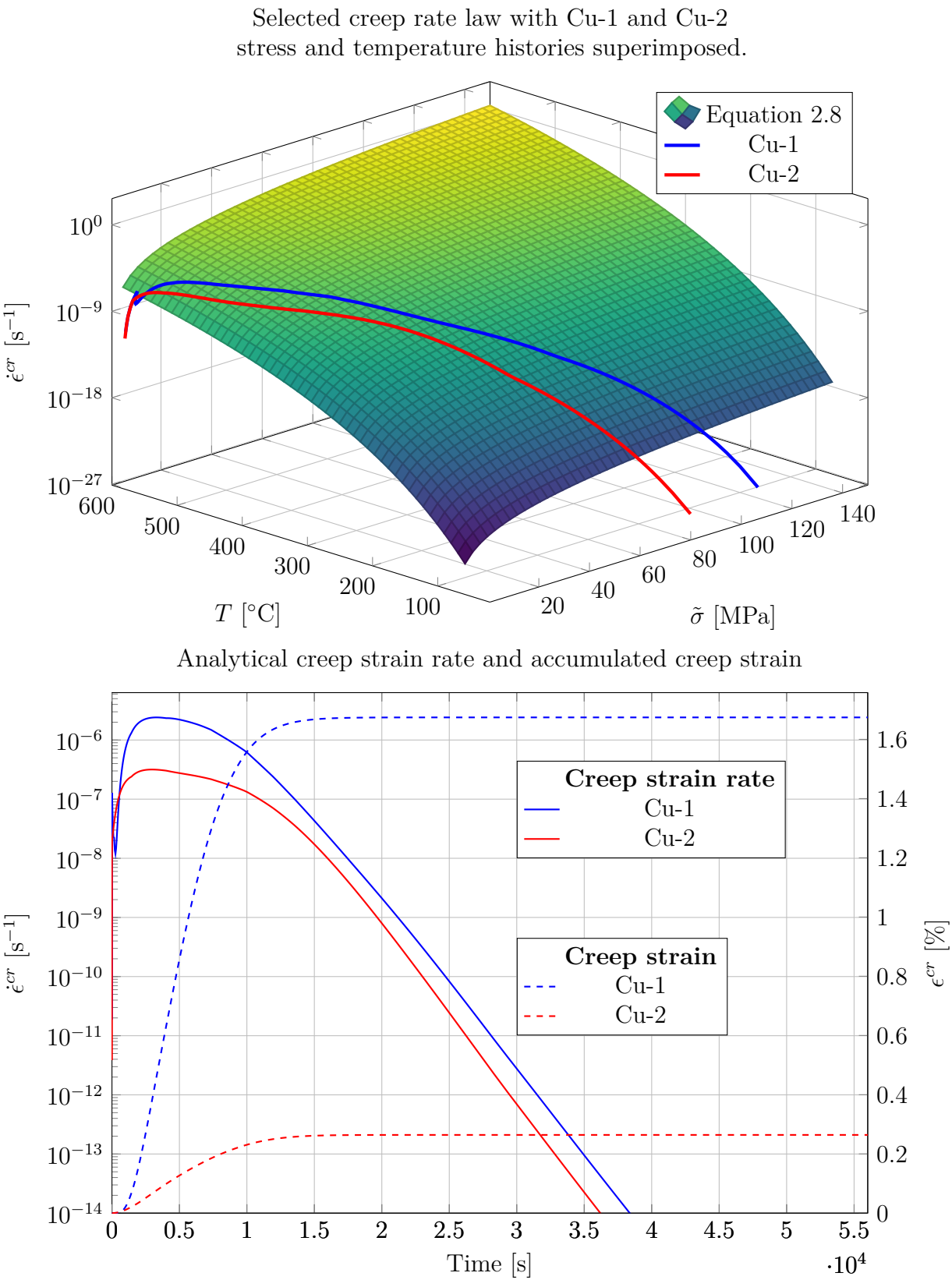

Figure 4.10: Analytical computation of creep strain.

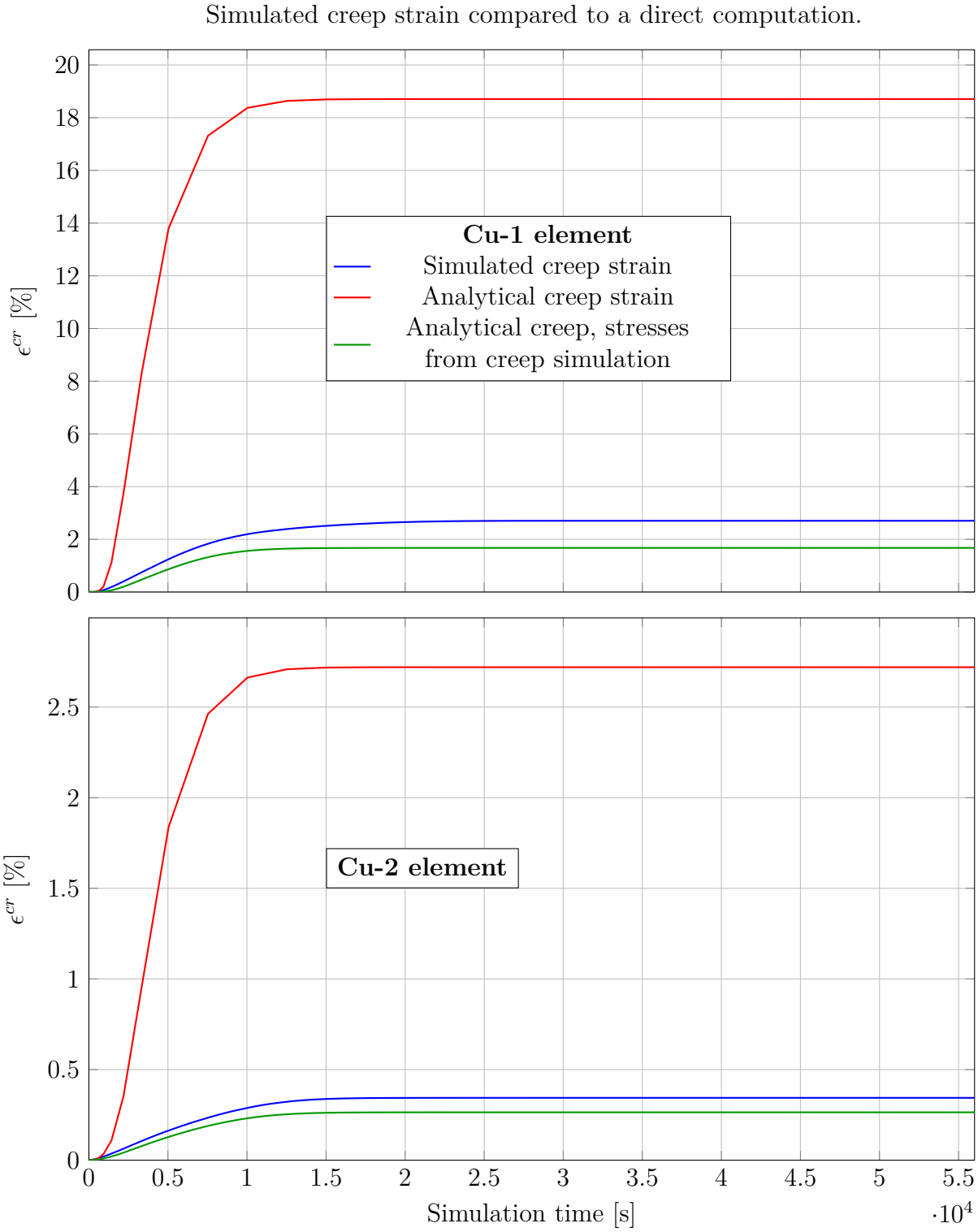

Figure 4.11: Comparison between simulated creep strain and a simplified analytical approach.

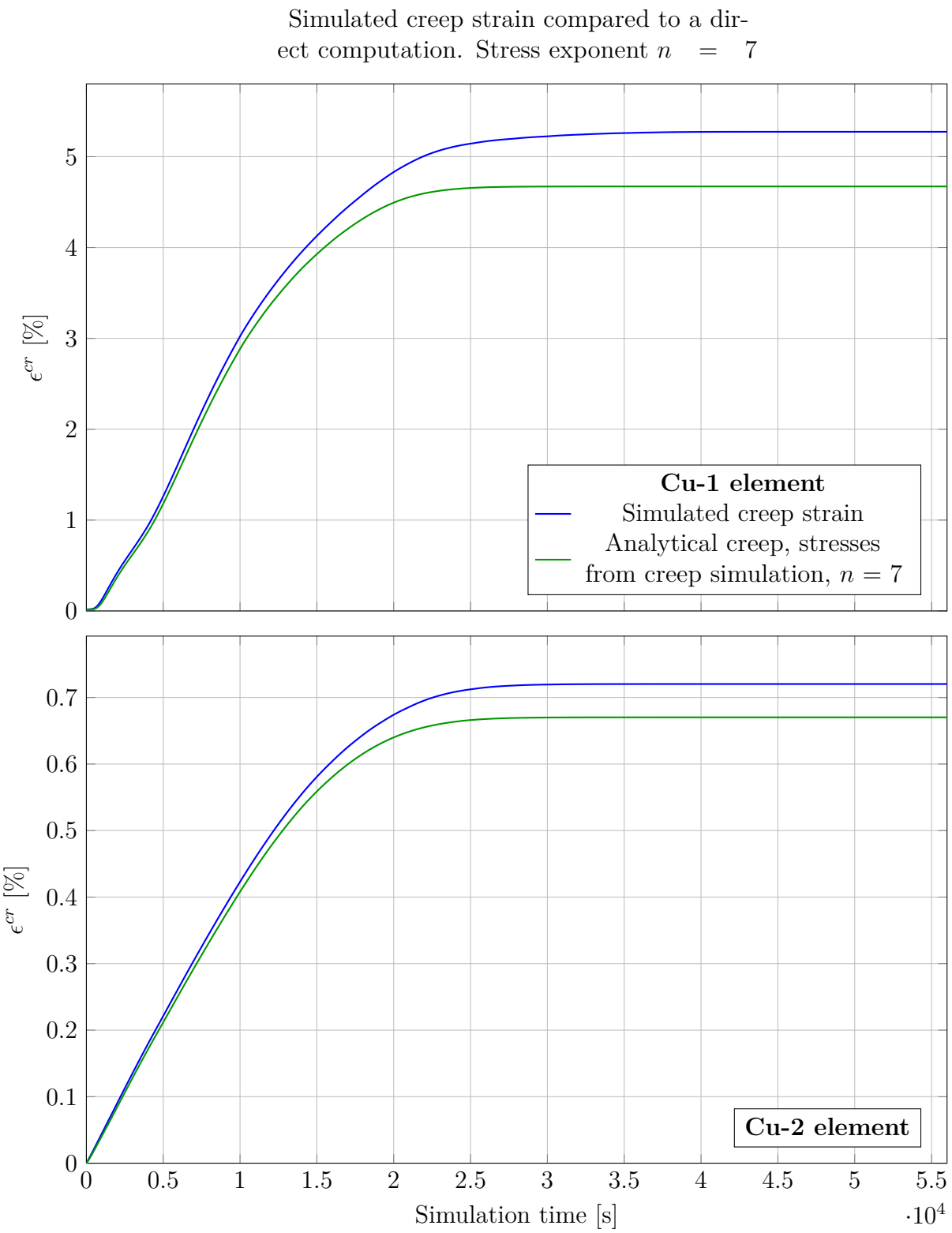

Figure 4.12: Comparison of stress history between FEM and a direct computation for a higher creep exponent. The stress history for the direct computation is taken from the simulation with high creep exponent.

4.2 Cutting operations and final residual stress

4.2.1 Cutting of the CuCrZr pipe

In order to perform experimental analysis on the residual stresses of the monoblock after production, the monoblock assembly, as shown in Figure 1.3, has to be cut into the individual monoblocks. This operation requires the cutting of the cooling pipe as explained in chapter 3. Figure 4.13 and 4.14 display the stress field before and after the simulated cut has taken place. The overall Mises stress of the part, specifically the CuCrZr pipe, drops. This is the expected behavior as the middle-plane of the CuCrZr pipe becomes unconstrained and it finds a lower energy equilibrium. The axial stress component of the newly unconstrained face becomes zero as there is no longer a force being applied in that direction as shown in Figure 4.14. This is also the expected result.

4.2.2 Horizontal cutting of the part

The visualization of the cutting process of the monoblock is shown in Figure 4.15. The elements are deleted as the simulation progresses and therefore, the stress concentration in the cutting plane increases. Figure 4.16 shows the stress state of the copper interlayer and the CuCrZr pipe during the cutting process. The stress state of the monoblock before and after the cut is shown in Figure 4.17. As it can be seen, the deviatoric and hoop stresses suffer a large change after the monoblock has been cut. The plots in Figure 4.18 compare the Mises and hoop stresses before and after the cut for the two paths indicated in Figure 4.3. There is a substantial change in the stress distribution. Both the copper interlayer and the CuCrZr pipe see a substantial decrease in hoop and Mises stresses. The stress distribution in tungsten also changes in order to preserve the stress equilibrium in the part.

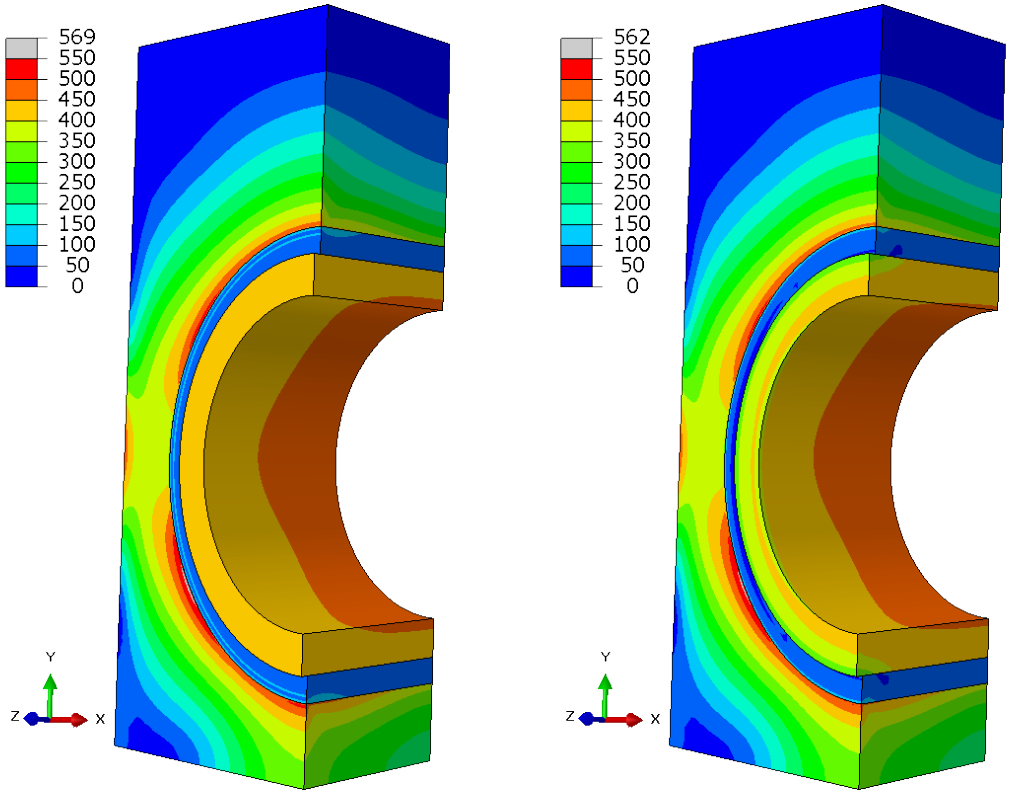

(a) Mises stress distribution, before (left) and after (right) the pipe cut.

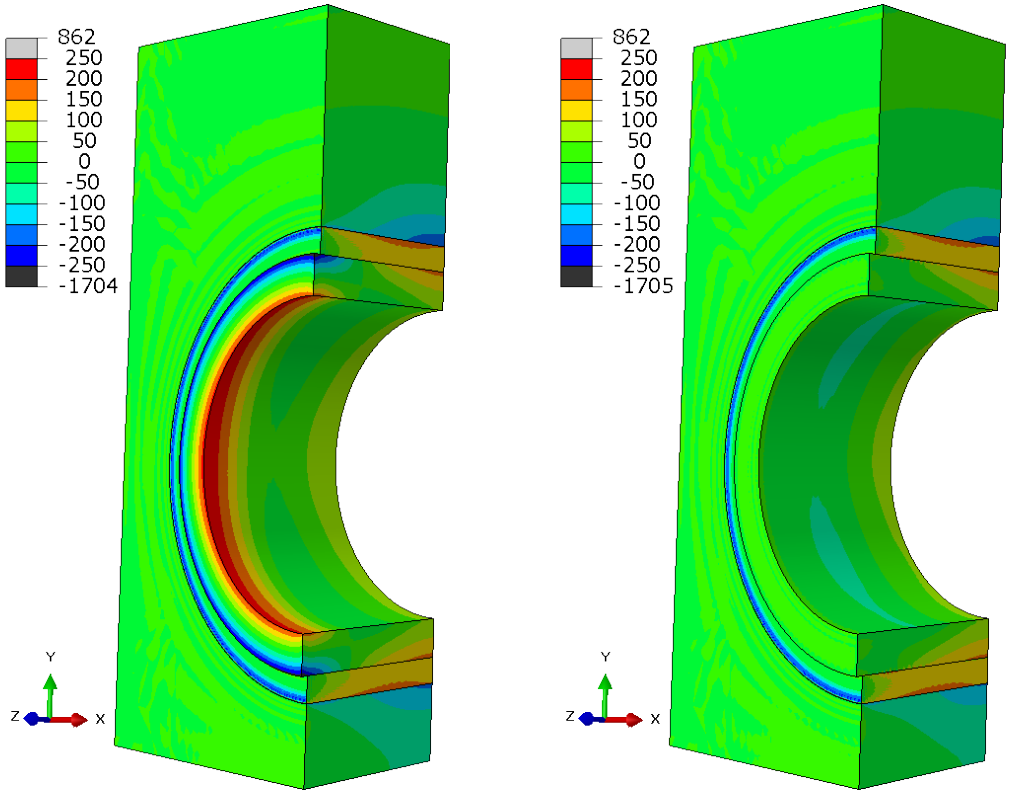

(b) Axial stress distribution, before (left) and after (right) the pipe cut.

Figure 4.13: Comparison of stress distribution of the monoblock, before and after the cutting of the CuCrZr pipe.

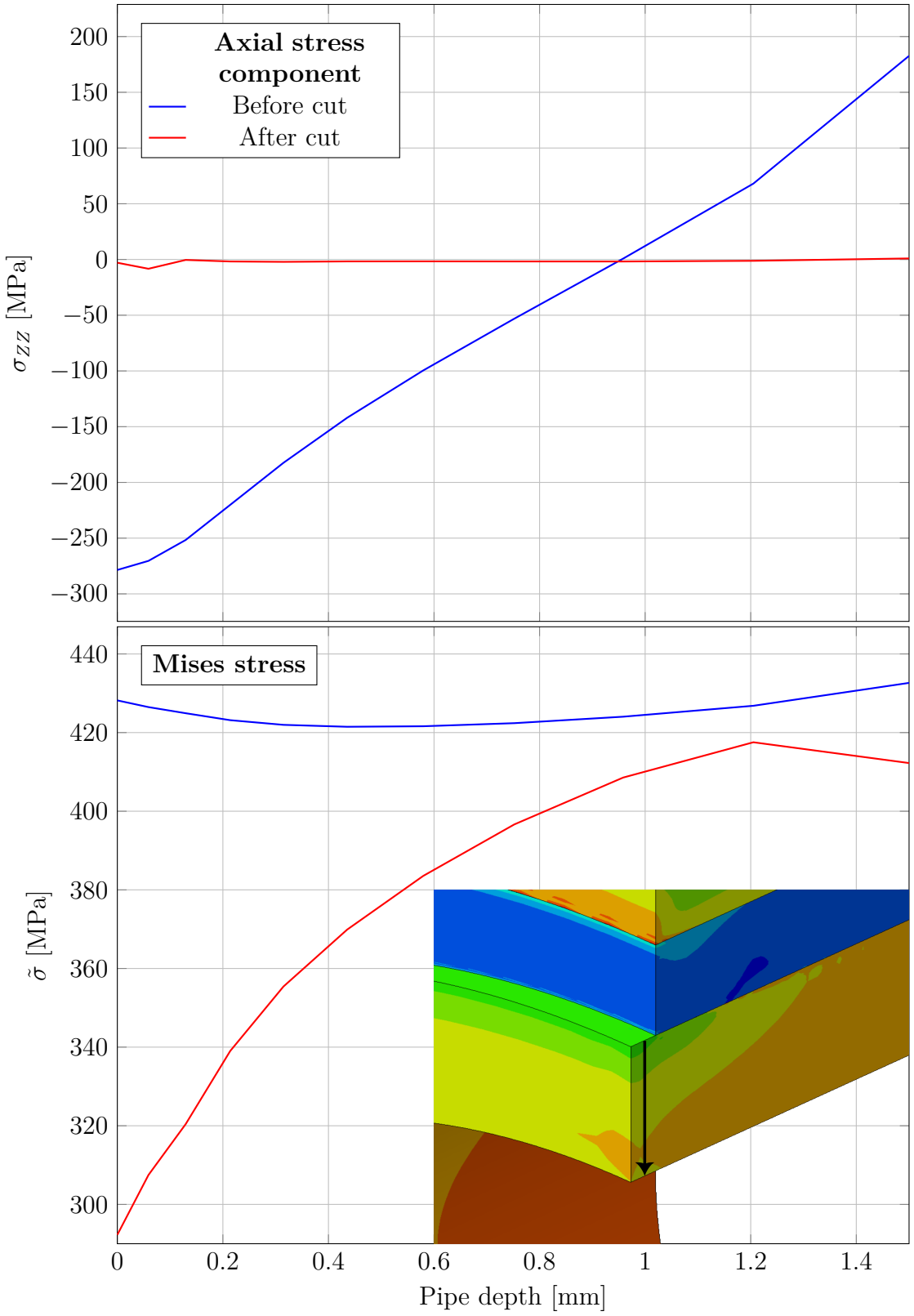

Figure 4.14: Stress difference in the top center of the pipe before and after the pipe cutting operation. Axial stress component (top), Mises stress (bottom).

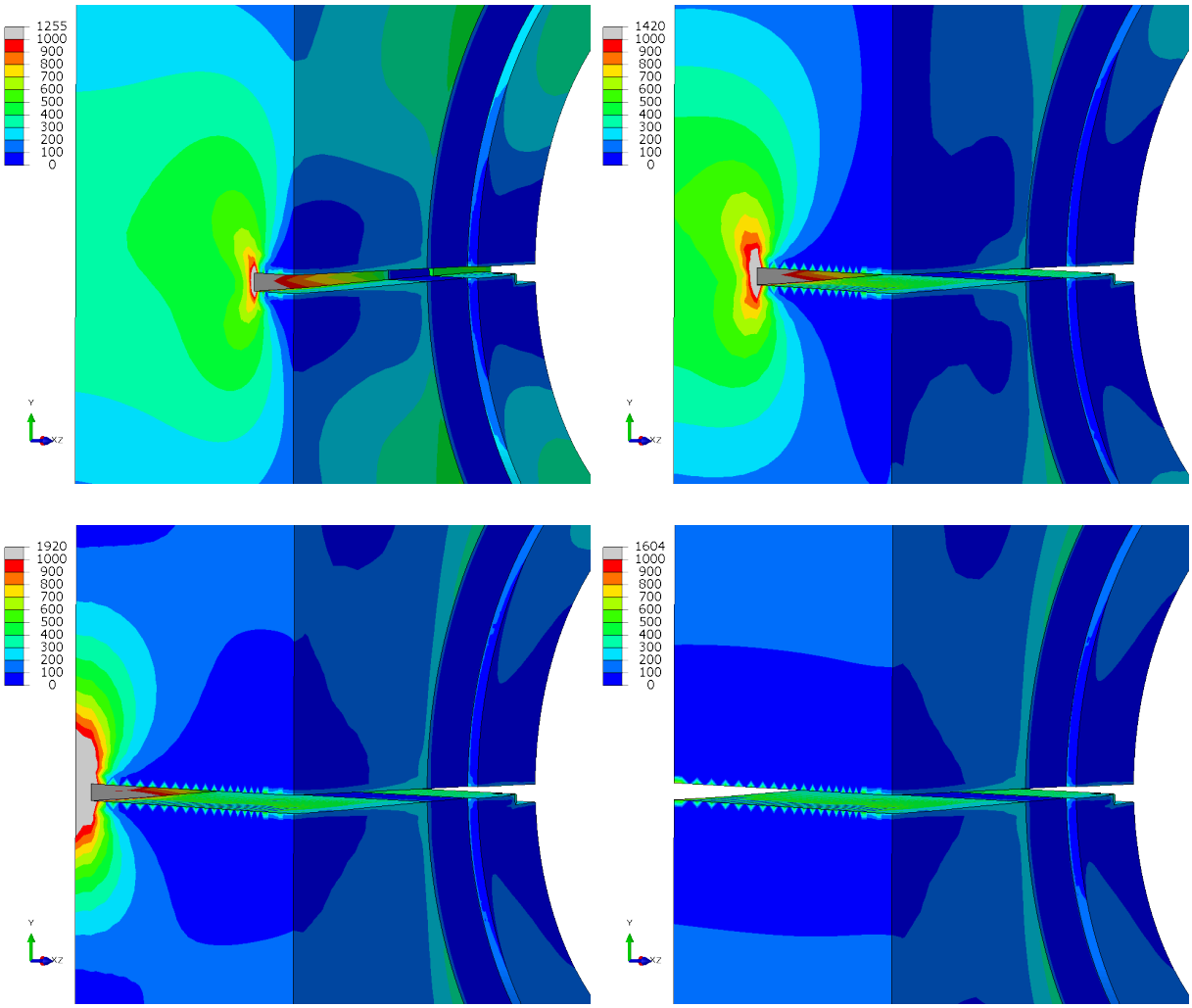

Figure 4.15: Mises stress evolution during the horizontal cutting process. The cutting front-plane generates a high stress concentration. The stress concentration is exacerbated when the cutting plane gets closer to the symmetry BC, which is physically incorrect for the real case.

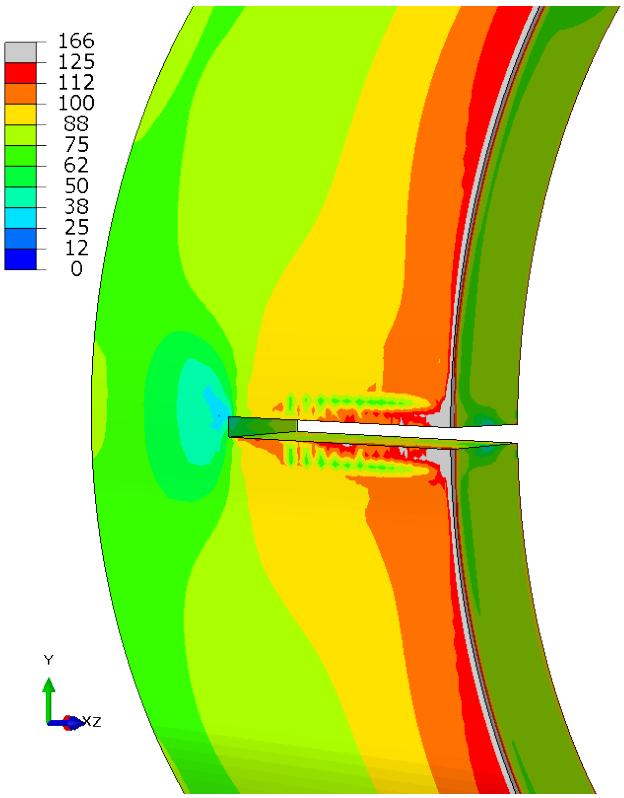

(a) Copper interlayer during cut.

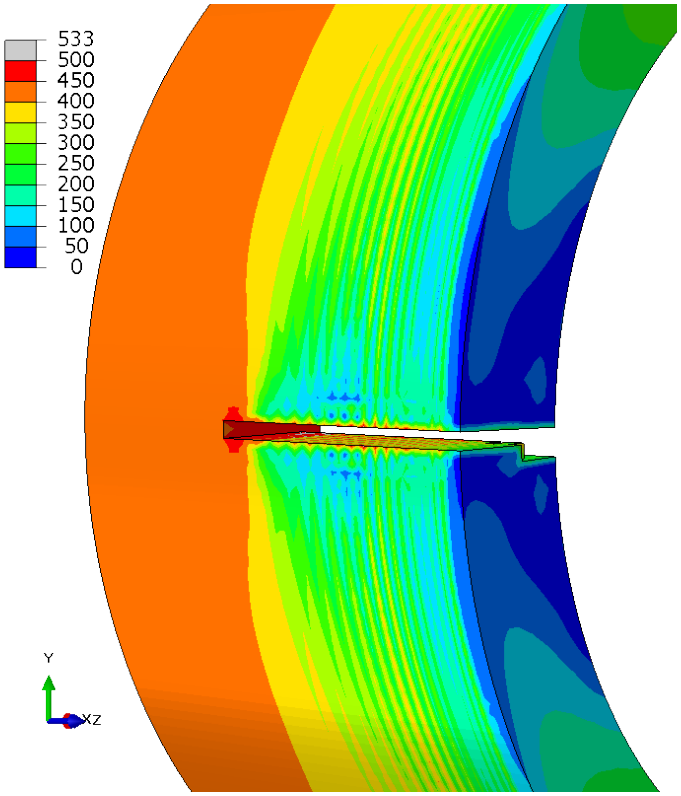

(b) CuCrZr pipe during cut.

Figure 4.16: Copper interlayer and CuCrZr pipe during the horizontal cutting operation.

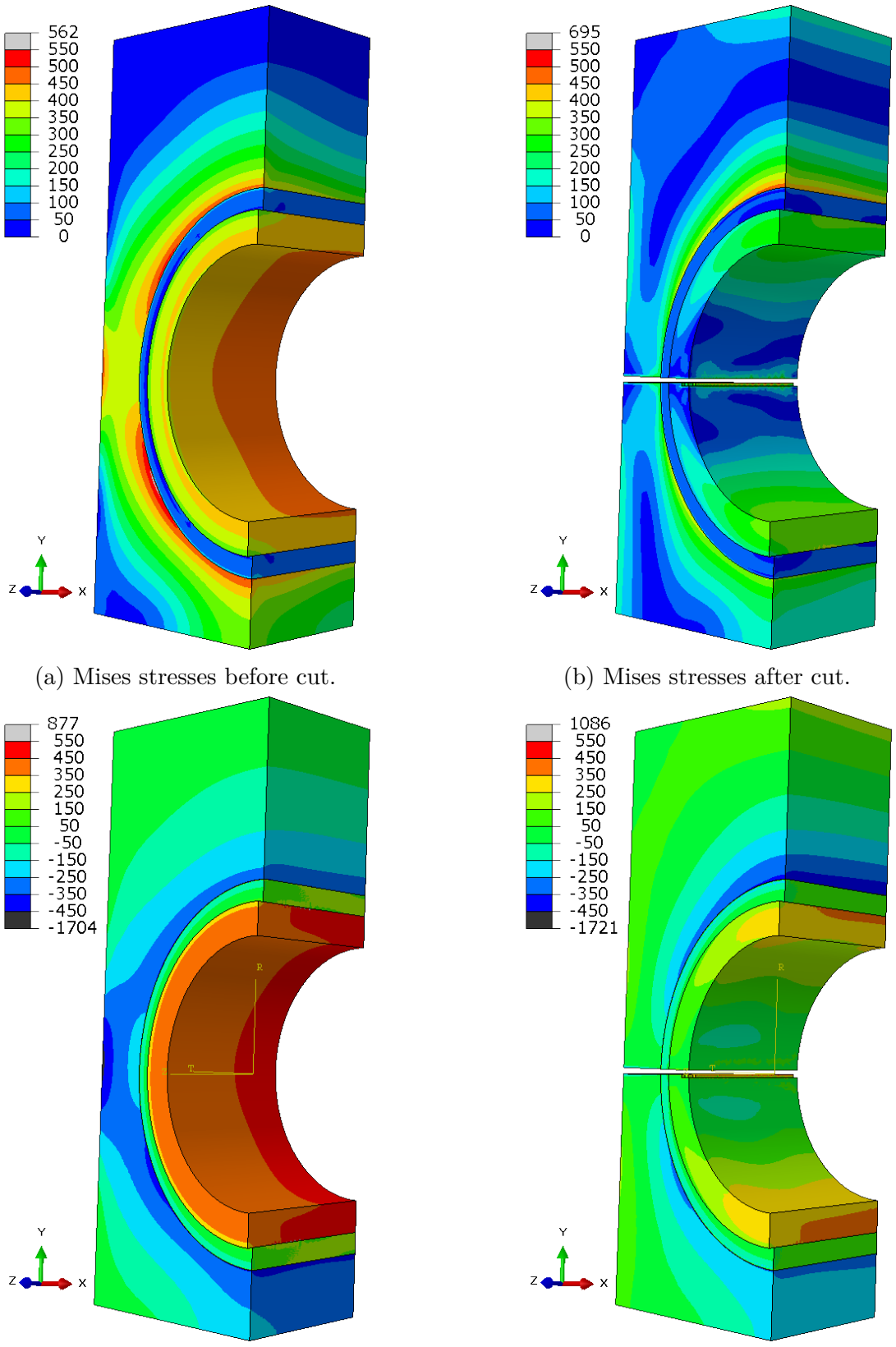

(a) Mises stresses before cut.

(b) Mises stresses after cut.

(c) Hoop stresses before cut.

(d) Hoop stresses after cut.

Figure 4.17: Stress distribution of the monoblock before and after being cut.

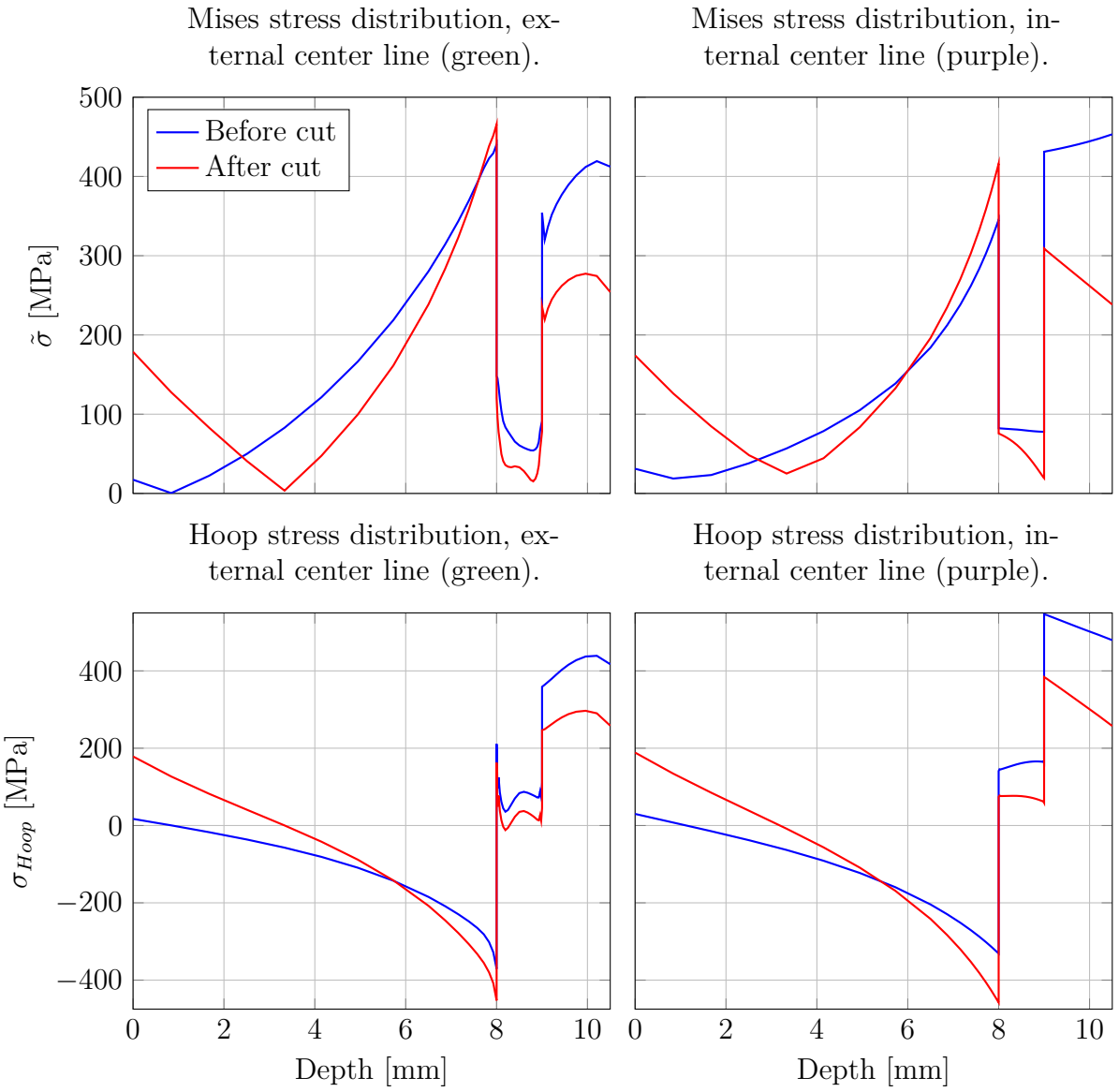

Figure 4.18: Stress distribution of the monoblock before and after the horizontal cutting operation. The external and internal profiles plotted are indicated in Figure 4.3 (green and purple arrows).

4.2.3 Mock-up FIB–DIC simulation

The result of the mock-up FIB–DIC simulation as discussed in Algorithm 3 is shown in Figure 4.20. The small cube was preloaded with a randomly chosen stress field using the OFHC-Cu material. In order to obtain a clean column cut, the mesh had to be created in such a way that the hexahedra were made concentric to the simulated ion-beam axis, as indicated in Figure 4.19. Figure 4.21 shows the displacement plot that a node in the center of the column would generate as the FIB erodes material from the sample. This is a proxy result for what a real DIC operation would obtain. These results demonstrate the capacity to simulate FIB–DIC analysis using the generic deletion subroutine. However, it is important to note that the mesh and dimensions used for this mock-up are not representative of a real FIB–DIC analysis.

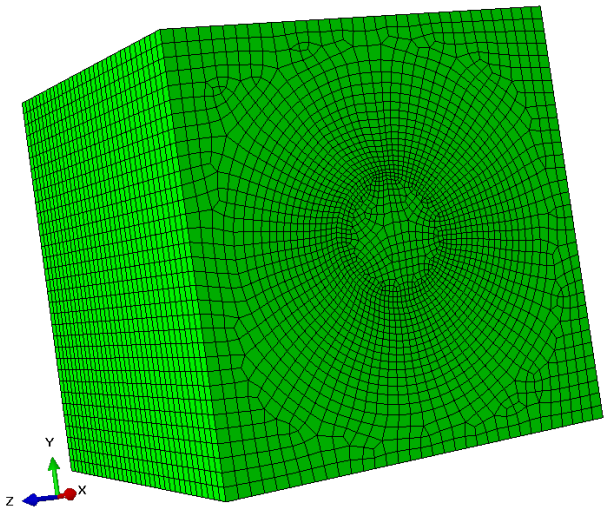

Figure 4.19: Mesh used for the mock-up FIB simulation. A finer mesh is required in order to generate better results.

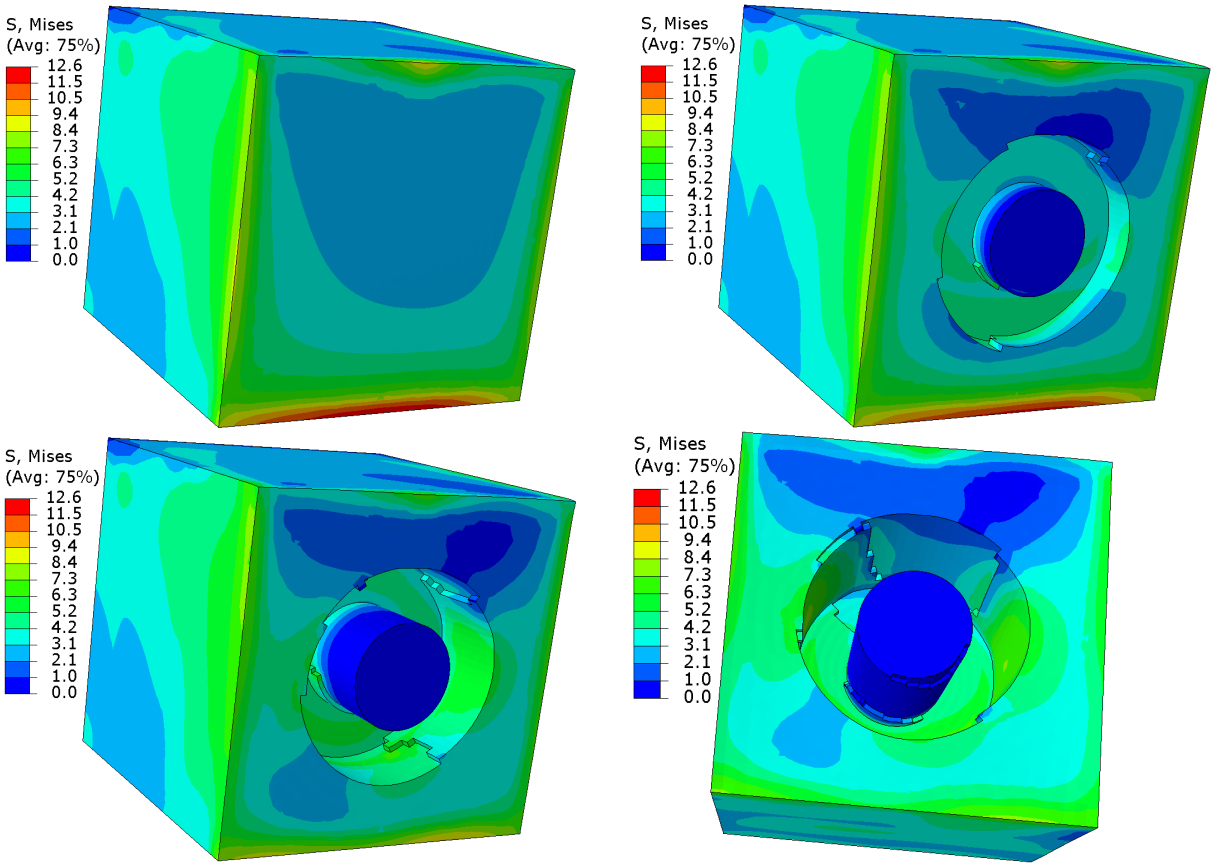

Figure 4.20: Mises stress field evolution during a mock-up FIB simulation.

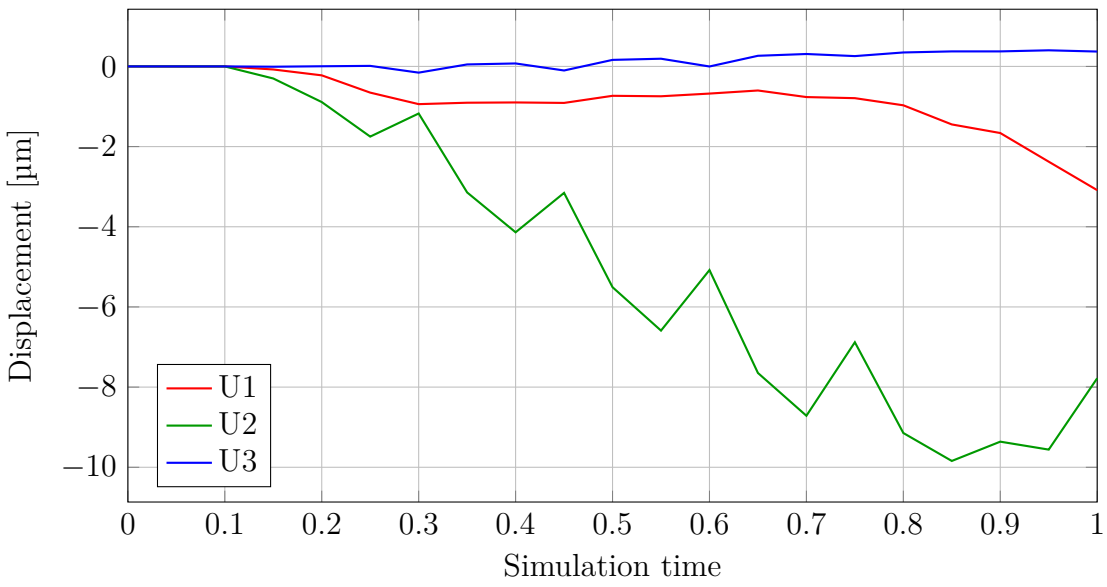

Figure 4.21: Displacement of the center node of the mock-up FIB simulation. The displacement of the node is a proxy of what the DIC method would produce.

Chapter 5

Analysis and conclusions

5.1 Impact of creep

The obtained results from both simulations, with and without creep, show that the selected secondary creep model had no impact on the overall stress build-up. The modified model with a creep stress exponent of $n = 7$ also had no substantial change on the results. Only the most highly stressed OFHC-Cu elements saw a substantial drop in their residual stresses. These elements correspond to the volume of the copper interlayer close to the external face and the tungsten interface. The reason for a lack of stress relaxation can be seen in Figure 4.6 and 4.9. At high temperatures, the copper elements see a reduction in their stresses and an increase in their creep strain. However, as the process progresses and the temperature drops, their creep rate becomes negligible and the elements become more stressed, as seen in their stress and plastic strain histories.

If the impact of creep were to be higher than the one simulated, stress relaxation could have a greater impact. For this reason, an accurate model of primary creep is needed, as primary creep rate is greater than secondary and it is expected to be the driving viscoplastic effect during HRP. A new test campaign was launched in order to characterize primary and secondary creep in OFHC-Cu by EUROfusion under the Divertor Work-Package (WPDIV). However, due to the reduced availability of test samples, the selected temperature-stress points had to be reduced to the relevant values that take place during HRP. The results of the present study served as the reference framework for the selection of the temperature-stress test points. These values have been selected from the temperature and stress histories from the selected OFHC-Cu elements, shown in Figure 5.1 and Table 5.1. The main difficulty in the characterization of creep parameters for the copper interlayer during HRP is the inverse relation between temperature and stress. As temperatures decrease, stresses rise, which leads to an uncertain assessment of the potential impact of viscous stress relaxation.

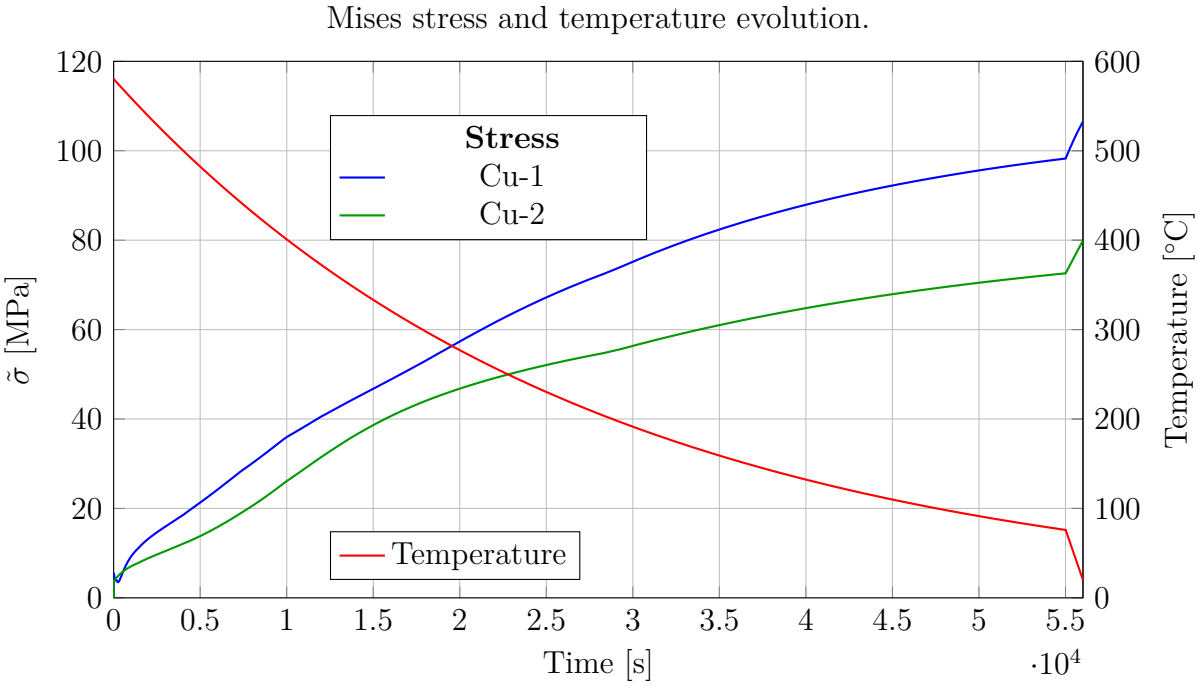

Figure 5.1: Stress and temperature history for selected OFHC-Cu elements. The increase in stresses is juxtaposed to the drop in temperature.

Temperature [°C]	Cu-1 (external) [MPa]	Cu-2 (internal) [MPa]
100	94	69.5
150	84	62
200	72.5	55
250	63	50
300	52.5	43.5
350	44	35.5
400	36	26.5
450	27	17.5
500	18.5	12
550	11	8

Table 5.1: Stress and temperature data-points for the selected OFHC-Cu elements in Figure 4.3. The data points have been taken from the results of the FEM simulation with creep enabled, shown in Figure 5.1.

5.2 Experimental analysis, stress changes after cutting operation

As discussed in chapter 3, the results generated by the FEM simulations need to be compared to the measurements obtained trough experimental testing. For example, previous monoblock designs were analyzed using neutron diffractometry as documented in [41, 42]. Figure 5.2 summarizes the obtained results of these studies. A good fit between the measured stress-strain and those from the FEM simulation in the region far from the copper interface is shown.

As of the time of writing, contour, micro-indentation and FIB–DIC methods are being used to asses the residual stress on the cut monoblock.

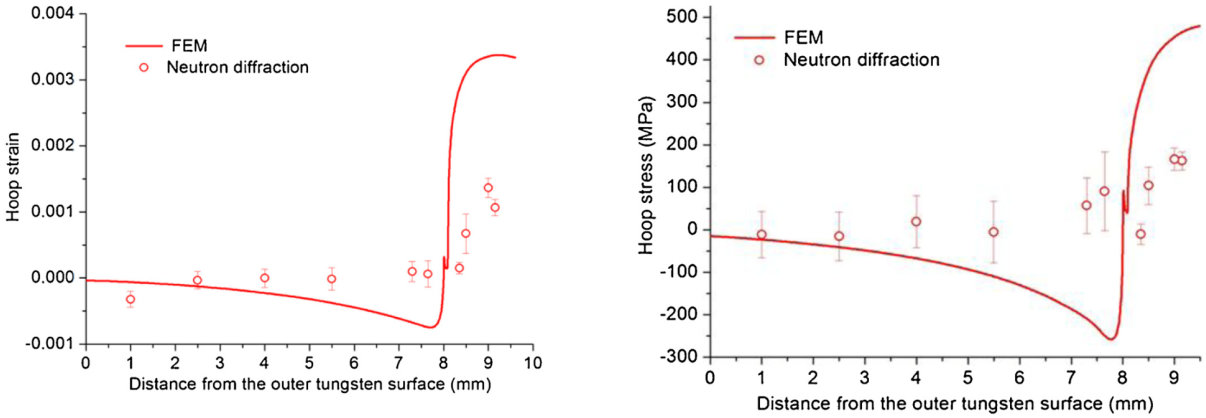

Figure 5.2: Residual stress measurements using neutron diffractometry compared to FEM. Image taken from [41].

The simulated cut of the monoblock points to a large change in the stress distribution in the materials. This presents a severe issue for experimental tests, as it indicates that the stress measurements are not going to be directly representative of those from the part after production. Nonetheless, the results generated by FEM cannot be fully trusted without first comparing them with the ones produced by the new experimental campaign, which, as of the time of writing, are not available.

5.3 Future studies and recommendations

5.3.1 Application of coupled primary and secondary creep

With primary creep data for the relevant temperature-stress range, the viscoplastic stress relaxation in the material can be more accurately assessed. Once the characterization of primary creep has been finalized for OFHC-Cu, a new set of studies should be performed in order to improve the results presented in this study. The coupling between primary and secondary creep will also need to be carried out in order to have a broader simulation time if it is required.

Due to the high stresses that develop in the CuCrZr pipe and the high temperatures during HRP, its viscoplastic properties should also be integrated into the analysis. In this study, the creep of CuCrZr was not considered due to a lack of applicable data. However, its integration into the analysis would allow the assessment of its impact on the residual stress build-up of the monoblock.

5.3.2 Experimental measurements of residual stresses

The data generated by experimental methods needs to be discussed under the light of the potential changes that the part may suffer from production to analysis. While this may seem obvious, the results from the horizontal cutting simulation show a large stress change in the part. Therefore, the measured values from the different experimental methods will need to be adjusted or corrected in order to represent the real stress-strain values after production of the part.

5.4 Closing remarks

The present study further tackles topics presented in the 2022 European DEMO divertor design and technology report [43]. It discussed the methodology to analyze the impact of viscous effects in the divertor monoblock interlayer and its impact has been assessed using models available in the literature. The final residual stresses of the part as it is going to be analyzed have also been simulated. However, the large stress change that takes place after the part has been cut will require validation using the measurements from experimental analysis.

Bibliography

[1] ITER. *What is a Tokamak?* 2022. URL: https://www.iter.org/mach/Tokamak.

[2] Takeshi Hirai et al. 'Use of tungsten material for the ITER divertor'. In: *Nuclear Materials and Energy* (July 2016). DOI: 10.1016/j.nme.2016.07.003.

[3] G.J. van Rooij et al. 'Tungsten divertor erosion in all metal devices: Lessons from the ITER like wall of JET'. In: *Journal of Nuclear Materials* 438 (2013). Proceedings of the 20th International Conference on Plasma-Surface Interactions in Controlled Fusion Devices, S42–S47. ISSN: 0022-3115. DOI: https://doi.org/10.1016/j.jnucmat.2013.01.007. URL: https://www.sciencedirect.com/science/article/pii/S0022311513000159.

[4] Jeong-Ha You, Muyuan Li and Kuo Zhang. 'Structural lifetime assessment for the DEMO divertor targets: Design-by-analysis approach and outstanding issues'. In: *Fusion Engineering and Design* 164 (2021), p. 112203. ISSN: 0920-3796. DOI: https://doi.org/10.1016/j.fusengdes.2020.112203. URL: https://www.sciencedirect.com/science/article/pii/S0920379620307511.

[5] Mike Fursdon, Muyuan Li and Jeong-Ha You. 'Enhancements in the structural integrity assessment of plasma facing components'. In: *Fusion Engineering and Design* 146 (2019). SI:SOFT-30, pp. 1591–1595. ISSN: 0920-3796. DOI: https://doi.org/10.1016/j.fusengdes.2019.02.135. URL: https://www.sciencedirect.com/science/article/pii/S0920379619303175.

[6] Muyuan Li et al. 'Fracture mechanical analysis of a tungsten monoblock-type plasma-facing component without macroscopic interlayer for high-heat-flux divertor target'. In: *Fusion Engineering and Design* 122 (2017), pp. 124–130. ISSN: 0920-3796. DOI: https://doi.org/10.1016/j.fusengdes.2017.09.002. URL: https://www.sciencedirect.com/science/article/pii/S0920379617308025.

[7] Jeong-Ha You, Muyuan Li and Kuo Zhang. 'Structural impact of creep in tungsten monoblock divertor target at 20 MW/m2'. In: *Nuclear Materials and Energy* 14 (2018), pp. 1–7. ISSN: 2352-1791. DOI: https://doi.org/10.1016/j.nme.2017.12.001. URL: https://www.sciencedirect.com/science/article/pii/S2352179117300571.

[8] Shigeru Saito et al. *Development of bonding techniques between tungsten and copper alloy for plasma facing components by HIP method. Bonding between tungsten and oxygen free copper*. Report No: JAERI-Research 99-049. Japan Atomic Energy Research Institute, Tokai, Ibaraki (Japan). Tokai Research Establishment, Aug. 1999. URL: https://inis.iaea.org/collection/NCLCollectionStore/_Public/31/009/31009658.pdf.

[9] Xiaochang Duan et al. 'A Phenomenological Primary–Secondary–Tertiary Creep Model for Polymer-Bonded Composite Materials'. In: *Polymers* 13.14 (2021). ISSN: 2073-4360. DOI: 10.3390/polym13142353. URL: https://www.mdpi.com/2073-4360/13/14/2353.

[10] F. H Norton. *The creep of steel at high temperatures*. McGraw-Hill, 1929. URL: https://archive.org/details/creepofsteelathi00nort.

[11] Michael Gorley et al. 'The EUROfusion materials property handbook for DEMO in-vessel components—Status and the challenge to improve confidence level for engineering data'. In: *Fusion Engineering and Design* 158 (2020), p. 111668. ISSN: 0920-3796. DOI: https://doi.org/10.1016/j.fusengdes.2020.111668. URL: https://www.sciencedirect.com/science/article/pii/S0920379620302167.

[12] A. Freed and K. P. Walker. 'Stress versus temperature dependent activation energies in creep'. In: *3rd International Conference on Constitutive Laws for Engineering Materials: Theory and Applications and Workshop on Innovative Use of Materials in Industrial and Infrastructure Design and Manufacturing* (1990). URL: https://ntrs.nasa.gov/citations/19900014457.

[13] C. R. Barrett, J. L. Lytton and O. D. Sherby. 'Effect of grain size and annealing treatment on steady state creep of copper'. In: (1965). URL: https://apps.dtic.mil/sti/citations/AD0615926.

[14] B. G. Thomas et al. 'Analysis of Thermal and Mechanical Behavior of Copper Molds during Continuous Casting of Steel Slabs'. In: *80th Steelmaking Conference Proceedings, Iron and Steel Society, Warrendale, PA, Chicago, IL* (1997), pp. 183–201. URL: http://ccc.illinois.edu/PDF%20Files/Publications/97_ISS_li_mold_dis_post.pdf.

[15] Rolf Sandström. 'Basic model for primary and secondary creep in copper'. In: *Acta Materialia* 60.1 (2012), pp. 314–322. ISSN: 1359-6454. DOI: https://doi.org/10.1016/j.actamat.2011.09.052. URL: https://www.sciencedirect.com/science/article/pii/S1359645411006999.

[16] Fangfei Sui and Rolf Sandström. 'Basic modelling of tertiary creep of copper'. In: *Journal of Materials Science* 53.9 (Jan. 2018), pp. 6850–6863. DOI: 10.1007/s10853-017-1968-7. URL: https://doi.org/10.1007/s10853-017-1968-7.

[17] G. Li, B. G. Thomas and J. F. Stubbins. 'Modeling creep and fatigue of copper alloys'. In: *Metallurgical and Materials Transactions A* 31.10 (Oct. 2000), pp. 2491–2502. DOI: 10.1007/s11661-000-0194-z. URL: https://doi.org/10.1007/s11661-000-0194-z.

[18] Rolf Sandström. 'Basic Creep-Fatigue Models Considering Cavitation'. In: *Transactions of the Indian National Academy of Engineering* (Oct. 2021). DOI: 10.1007/s41403-021-00283-2. URL: https://doi.org/10.1007/s41403-021-00283-2.

[19] Rolf Sandström. 'Fundamental Models for Creep Properties of Steels and Copper'. In: *Transactions of the Indian Institute of Metals* 69.2 (Dec. 2015), pp. 197–202. DOI: 10.1007/s12666-015-0762-y. URL: https://doi.org/10.1007/s12666-015-0762-y.

[20] J.H. You et al. 'European divertor target concepts for DEMO: Design rationales and high heat flux performance'. In: *Nuclear Materials and Energy* 16 (2018), pp. 1–11. ISSN: 2352-1791. DOI: https://doi.org/10.1016/j.nme.2018.05.012. URL: https://www.sciencedirect.com/science/article/pii/S2352179118300437.

[21] Dassault Systèmes Simulia Corp. *ABAQUS/Standard User's Manual, Version 2022*. Dassault Systèmes Simulia Corp, 2021.

[22] Walt Brainerd. 'Fortran 77'. In: *Commun. ACM* 21.10 (Oct. 1978), pp. 806–820. ISSN: 0001-0782. DOI: 10.1145/359619.359621. URL: https://doi.org/10.1145/359619.359621.

[23] JTC1/SC22/WG5. *Information technology — Programming languages — Fortran — Part 1: Base language*. Standard ISO/IEC 1539:2010. Geneva, CH: International Organization for Standardization, Oct. 2010. URL: https://www.iso.org/standard/50459.html.

[24] Intel. *Intel Fortran OneAPI compiler*. 2021. URL: https://www.intel.com/content/www/us/en/developer/tools/oneapi/fortran-compiler.html.

[25] Maxima. *Maxima, a Computer Algebra System. Version 5.45.1*. 2021. URL: https://maxima.sourceforge.io/.

[26] Guido Van Rossum and Fred L. Drake. *Python 3 Reference Manual*. Scotts Valley, CA: CreateSpace, 2009. ISBN: 1441412697. DOI: 10.5555/1593511.

[27] *DIN EN 12163:2016-11, Kupfer und Kupferlegierungen_- Stangen zur allgemeinen Verwendung; Deutsche Fassung EN_12163:2016*. Tech. rep. Berlin: Beuth Verlag GmbH, 2019.

[28] J.-H. You and M. Miskiewicz. 'Material parameters of copper and CuCrZr alloy for cyclic plasticity at elevated temperatures'. In: *Journal of Nuclear Materials* 373.1 (2008), pp. 269–274. ISSN: 0022-3115. DOI: https://doi.org/10.1016/j.jnucmat.2007.06.005. URL: https://www.sciencedirect.com/science/article/pii/S0022311507008318.

[29] Henrik C M Andersson-Östling and Rolf Sandström. *Survey of creep properties of copper intended for nuclear waste disposal*. eng. 2009. URL: https://www.osti.gov/etdeweb/servlets/purl/992707 (visited on 23/07/2022).

[30] Rui Wu, Rolf Sandström and Facredin Seitisleam. *Creep properties of phosphorus alloyed oxygen free copper under multiaxial stress state*. eng. 2010, pp. 178–195. URL: http://urn.kb.se/resolve?urn=urn:nbn:se:kth:diva-242807 (visited on 23/07/2022).

[31] Rolf Sandström and Henrik C.M. Andersson. 'Creep in phosphorus alloyed copper during power-law breakdown'. In: *Journal of Nuclear Materials* 372.1 (2008), pp. 76–88. ISSN: 0022-3115. DOI: https://doi.org/10.1016/j.jnucmat.2007.02.005. URL: https://www.sciencedirect.com/science/article/pii/S0022311507003303.

[32] *The Application of the Norton-Bailey Law for Creep Prediction Through Power Law Regression*. Vol. Volume 7A: Structures and Dynamics. Turbo Expo: Power for Land, Sea, and Air. V07AT26A005. June 2013. DOI: 10.1115/GT2013-96008. eprint: https://asmedigitalcollection.asme.org/GT/proceedings-pdf/GT2013/55263/V07AT26A005/2422162/v07at26a005-gt2013-96008.pdf. URL: https://doi.org/10.1115/GT2013-96008.

[33] B. Wilshire and A.J. Battenbough. 'Creep and creep fracture of polycrystalline copper'. In: *Materials Science and Engineering: A* 443.1 (2007), pp. 156–166. ISSN: 0921-5093. DOI: https://doi.org/10.1016/j.msea.2006.08.094. URL: https://www.sciencedirect.com/science/article/pii/S0921509306019460.

[34] B.N. Singh et al. 'Creep-fatigue deformation behaviour of OFHC-copper and CuCrZr alloy with different heat treatments and with and without neutron irradiation'. In: (Aug. 2005).

[35] Rolf Sandström. 'Fundamental Models for the Creep of Metals'. In: *Creep*. Ed. by Tomasz Tanski, Marek Sroka and Adam Zielinski. Rijeka: IntechOpen, 2018. Chap. 12. DOI: 10.5772/intechopen.70726. URL: https://doi.org/10.5772/intechopen.70726.

[36] Fangfei Sui. 'Fundamental models and testing of creep in copper'. eng. 2018. URL: http://urn.kb.se/resolve?urn=urn:nbn:se:kth:diva-227968 (visited on 23/07/2022).

[37] M. Pahutova, J. Cadek and P. Rys. 'High temperature creep in copper'. In: *The Philosophical Magazine: A Journal of Theoretical Experimental and Applied Physics* 23.183 (1971), pp. 509–517. DOI: 10.1080/14786437108216401. eprint: https://doi.org/10.1080/14786437108216401. URL: https://doi.org/10.1080/14786437108216401.

[38] A.M. Korsunsky et al. 'Nanoscale residual stress depth profiling by Focused Ion Beam milling and eigenstrain analysis'. In: *Materials & Design* 145 (2018), pp. 55–64. ISSN: 0264-1275. DOI: https://doi.org/10.1016/j.matdes.2018.02.044. URL: https://www.sciencedirect.com/science/article/pii/S0264127518301291.

[39] Enrico Salvati et al. 'The effect of eigenstrain induced by ion beam damage on the apparent strain relief in FIB-DIC residual stress evaluation'. In: *Materials & Design* 92 (2016), pp. 649–658. ISSN: 0264-1275. DOI: https://doi.org/10.1016/j.matdes.2015.12.015. URL: https://www.sciencedirect.com/science/article/pii/S0264127515308789.

[40] E. Salvati et al. 'Eigenstrain reconstruction of residual strains in an additively manufactured and shot peened nickel superalloy compressor blade'. In: *Computer Methods in Applied Mechanics and Engineering* 320 (2017), pp. 335–351. ISSN: 0045-7825. DOI: https://doi.org/10.1016/j.cma.2017.03.005. URL: https://www.sciencedirect.com/science/article/pii/S0045782516318461.

[41] R. Coppola et al. 'Neutron diffraction measurement of residual stresses in an ITER-like tungsten-monoblock type plasma-facing component'. In: *Fusion Engineering and Design* 146 (2019). SI:SOFT-30, pp. 701–704. ISSN: 0920-3796. DOI: https://doi.org/10.1016/j.fusengdes.2019.01.059. URL: https://www.sciencedirect.com/science/article/pii/S0920379619300675.

[42] Roberto Coppola et al. 'Small-scale neutron tomography & diffractometry - Interim Report 2021'. In: *EUROfusion WP DIV* (2021). Reference: DIV-DEMO.T.2-T003. URL: https://idm.euro-fusion.org/?uid=2PHJVG.

[43] J.H. You et al. 'Divertor of the European DEMO: Engineering and technologies for power exhaust'. In: *Fusion Engineering and Design* 175 (2022), p. 113010. ISSN: 0920-3796. DOI: https://doi.org/10.1016/j.fusengdes.2022.113010. URL: https://www.sciencedirect.com/science/article/pii/S0920379622000102.

[44] United Nations. *Sustainable Development Goals*. 2022. URL: https://sdgs.un.org/.

Appendix A

Material properties and part design

The relevant material properties used in the study are included in the tables below, with the exception of creep, which is discussed in subsection 2.5.2. The unit system used for the material properties and the dimensions of the monoblock is SI [mm]. The implementation of the creep model can be found in Appendix B. The relevant materials are OFHC-Cu, CuCrZr-IG and tungsten.

The design of a single monoblock is included at the end of this appendix.

OFHC-Cu			
Yield at $\epsilon^{pl} = 0$ [MPa]	Kinematic Hardening		Temperature [°C]
	C_1	γ_1	
3	64,257	888	20
3	44,324	923	200
3	31,461	952	400
3	17,188	979	550

OFHC-Cu							
Yield at $\epsilon^{pl} = 0$ [MPa]	Kinematic Hardening						Temperature [°C]
	C_1	γ_1	C_2	γ_3	C_3	γ_3	
280	$3 \cdot 10^5$	4,000	30,000	825	7,000	1	20
190	$3 \cdot 10^5$	4,000	30,000	825	1,500	1	350

Table A.1: Plastic parameters as a function of temperature for OFHC-Cu and CuCrZr-IG.

OFHC-Cu			
Equivalent stress [MPa]	Q-Infinity	Hardening parameter b	Temperature [°C]
3	76	8	20
3	60	15	200
3	36	25	400
3	16	40	550

Table A.2: Cyclic hardening parameters for OFHC-Cu

Tungsten		
σ_Y [MPa]	ϵ^{pl} [-]	Temperature [°C]
1,384.62	0	0
1,324.69	0	50
1,266.32	0	100
1,209.48	0	150
1,154.17	0	200
1,100.37	0	250
1,048.06	0	300
997.23	0	350
947.86	0	400
899.95	0	450
853.48	0	500
808.43	0	550
764.79	0	600
722.54	0	650
681.68	0	700
642.18	0	750
604.03	0	800
567.23	0	850
531.74	0	900
497.57	0	950
464.69	0	1,000
433.09	0	1,050
402.76	0	1,100
373.68	0	1,150
345.84	0	1,200

Tungsten		
σ_Y [MPa]	ϵ^{pl} [-]	Temperature [°C]
319.23	0	1,250
293.83	0	1,300
269.62	0	1,350
246.59	0	1,400
224.73	0	1,450
204.03	0	1,500
184.46	0	1,550
166.02	0	1,600
148.69	0	1,650
132.45	0	1,700
117.3	0	1,750
103.22	0	1,800
90.18	0	1,850
78.19	0	1,900
67.23	0	1,950
57.27	0	2,000
48.32	0	2,050
40.34	0	2,100
33.33	0	2,150
27.28	0	2,200
22.17	0	2,250
17.98	0	2,300
14.71	0	2,350
12.33	0	2,400
10.84	0	2,450
10.21	0	2,500

Table A.3: Plastic parameters as a function of temperature for tungsten.

Tungsten	
Expansion [mm °C^{-1} mm^{-1}]	Temperature [°C]
$4.5 \cdot 10^{-6}$	20
$4.5 \cdot 10^{-6}$	100
$4.53 \cdot 10^{-6}$	200
$4.58 \cdot 10^{-6}$	300
$4.63 \cdot 10^{-6}$	400
$4.68 \cdot 10^{-6}$	500
$4.72 \cdot 10^{-6}$	600
$4.76 \cdot 10^{-6}$	700
$4.81 \cdot 10^{-6}$	800
$4.85 \cdot 10^{-6}$	900
$4.89 \cdot 10^{-6}$	1,000
$4.98 \cdot 10^{-6}$	1,200
$5.08 \cdot 10^{-6}$	1,400
$5.18 \cdot 10^{-6}$	1,600
$5.3 \cdot 10^{-6}$	1,800
$5.43 \cdot 10^{-6}$	2,000
$5.57 \cdot 10^{-6}$	2,200
$5.74 \cdot 10^{-6}$	2,400
$5.93 \cdot 10^{-6}$	2,600
$6.15 \cdot 10^{-6}$	2,800
$6.4 \cdot 10^{-6}$	3,000
$6.67 \cdot 10^{-6}$	3,200

OFHC-Cu	
Expansion [mm °C^{-1} mm^{-1}]	Temperature [°C]
$1.68 \cdot 10^{-5}$	20
$1.7 \cdot 10^{-5}$	50
$1.72 \cdot 10^{-5}$	100
$1.74 \cdot 10^{-5}$	150
$1.76 \cdot 10^{-5}$	200
$1.78 \cdot 10^{-5}$	250
$1.79 \cdot 10^{-5}$	300
$1.81 \cdot 10^{-5}$	350
$1.82 \cdot 10^{-5}$	400
$1.84 \cdot 10^{-5}$	450
$1.85 \cdot 10^{-5}$	500
$1.87 \cdot 10^{-5}$	550
$1.88 \cdot 10^{-5}$	600
$1.9 \cdot 10^{-5}$	650
$1.91 \cdot 10^{-5}$	700
$1.93 \cdot 10^{-5}$	750
$1.96 \cdot 10^{-5}$	800
$1.98 \cdot 10^{-5}$	850
$2.01 \cdot 10^{-5}$	900

CuCrZr-IG	
Expansion [mm °C^{-1} mm^{-1}]	Temperature [°C]
$1.67 \cdot 10^{-5}$	20
$1.73 \cdot 10^{-5}$	100
$1.77 \cdot 10^{-5}$	200
$1.8 \cdot 10^{-5}$	300
$1.81 \cdot 10^{-5}$	400
$1.85 \cdot 10^{-5}$	500
$1.86 \cdot 10^{-5}$	600

Table A.4: Thermal expansion as a function of temperature for tungsten, OFHC-Cu and CuCrZr-IG.

Tungsten	
Conductivity [mW mm^{-1} °C^{-1}]	Temperature [°C]
173	20
165	100
155	200
145	300
140	400
132	500
128	600
122	700
118	800
113	900
110	1,000
108	1,100
105	1,200
103.6	1,300
102.2	1,400
101.1	1,500
100.3	1,600
99.7	1,700
99.4	1,800
99.2	1,900
99.1	2,000
99.1	2,100
99.1	2,200
99	2,300
98.9	2,400

OFHC-Cu	
Conductivity [mW mm^{-1} °C^{-1}]	Temperature [°C]
400.58	20
398.47	50
394.94	100
391.44	150
387.94	200
384.45	250
380.98	300
377.52	350
374.07	400
370.64	450
367.22	500
363.8	550
360.41	600
357.02	650
353.65	700
350.28	750
346.93	800
343.6	850
340.27	900
336.96	950
333.66	1,000

CuCrZr-IG	
Conductivity [mW mm^{-1} °C^{-1}]	Temperature [°C]
318	20
324	50
333	100
339	150
343	200
345	250
346	300
347	350
347	400
346	450
346	500

Table A.5: Thermal conductivity as a function of temperature for tungsten, OFHC-Cu and CuCrZr-IG.

Tungsten	
Density [t mm^{-3}]	Temperature [°C]
$1.93 \cdot 10^{-8}$	20
$1.93 \cdot 10^{-8}$	100
$1.93 \cdot 10^{-8}$	200
$1.92 \cdot 10^{-8}$	300
$1.92 \cdot 10^{-8}$	400
$1.92 \cdot 10^{-8}$	500
$1.92 \cdot 10^{-8}$	600
$1.91 \cdot 10^{-8}$	700
$1.91 \cdot 10^{-8}$	800
$1.91 \cdot 10^{-8}$	900
$1.9 \cdot 10^{-8}$	1,000
$1.9 \cdot 10^{-8}$	1,100
$1.9 \cdot 10^{-8}$	1,200

OFHC-Cu	
Density [t mm^{-3}]	Temperature [°C]
$8.94 \cdot 10^{-9}$	20
$8.93 \cdot 10^{-9}$	50
$8.9 \cdot 10^{-9}$	100
$8.88 \cdot 10^{-9}$	150
$8.85 \cdot 10^{-9}$	200
$8.83 \cdot 10^{-9}$	250
$8.8 \cdot 10^{-9}$	300
$8.77 \cdot 10^{-9}$	350
$8.74 \cdot 10^{-9}$	400
$8.71 \cdot 10^{-9}$	450
$8.68 \cdot 10^{-9}$	500
$8.65 \cdot 10^{-9}$	550
$8.61 \cdot 10^{-9}$	600
$8.57 \cdot 10^{-9}$	650
$8.54 \cdot 10^{-9}$	700
$8.5 \cdot 10^{-9}$	750
$8.45 \cdot 10^{-9}$	800
$8.41 \cdot 10^{-9}$	850
$8.36 \cdot 10^{-9}$	900
$8.32 \cdot 10^{-9}$	950
$8.27 \cdot 10^{-9}$	1,000

CuCrZr-IG	
Density [t mm^{-3}]	Temperature [°C]
$8.9 \cdot 10^{-9}$	20
$8.86 \cdot 10^{-9}$	100
$8.82 \cdot 10^{-9}$	200
$8.77 \cdot 10^{-9}$	300
$8.72 \cdot 10^{-9}$	400
$8.67 \cdot 10^{-9}$	500

Table A.6: Density as a function of temperature for tungsten, OFHC-Cu and CuCrZr-IG.

Tungsten		
Young [MPa]	Poisson [-]	Temperature [°C]
$3.98 \cdot 10^5$	0.29	20
$3.97 \cdot 10^5$	0.29	100
$3.96 \cdot 10^5$	0.29	200
$3.95 \cdot 10^5$	0.29	300
$3.93 \cdot 10^5$	0.29	400
$3.9 \cdot 10^5$	0.29	500
$3.87 \cdot 10^5$	0.29	600
$3.83 \cdot 10^5$	0.29	700
$3.79 \cdot 10^5$	0.29	800
$3.74 \cdot 10^5$	0.29	900
$3.68 \cdot 10^5$	0.29	1,000
$3.63 \cdot 10^5$	0.29	1,100
$3.56 \cdot 10^5$	0.29	1,200
$3.49 \cdot 10^5$	0.29	1,300
$3.41 \cdot 10^5$	0.29	1,400
$3.33 \cdot 10^5$	0.29	1,500
$3.25 \cdot 10^5$	0.29	1,600
$3.15 \cdot 10^5$	0.29	1,700
$3.06 \cdot 10^5$	0.29	1,800
$2.95 \cdot 10^5$	0.29	1,900
$2.85 \cdot 10^5$	0.29	2,000
$2.73 \cdot 10^5$	0.29	2,100
$2.61 \cdot 10^5$	0.29	2,200
$2.49 \cdot 10^5$	0.29	2,300
$2.36 \cdot 10^5$	0.29	2,400

OFHC-Cu		
Young [MPa]	Poisson [-]	Temperature [°C]
$1.17 \cdot 10^5$	0.33	20
$1.16 \cdot 10^5$	0.33	50
$1.14 \cdot 10^5$	0.33	100
$1.12 \cdot 10^5$	0.33	150
$1.1 \cdot 10^5$	0.33	200
$1.08 \cdot 10^5$	0.33	250
$1.05 \cdot 10^5$	0.33	300
$1.02 \cdot 10^5$	0.33	350
98,256	0.33	400
94,497.75	0.33	450
90,425	0.33	500
86,037.75	0.33	550
81,336	0.33	600
76,319.75	0.33	650
70,989	0.33	700
65,343.75	0.33	750
59,384	0.33	800
53,109.75	0.33	850
46,521	0.33	900
39,617.75	0.33	950
32,400	0.33	1,000

CuCrZr-IG		
Young [MPa]	Poisson [-]	Temperature [°C]
$1.28 \cdot 10^5$	0.33	20
$1.27 \cdot 10^5$	0.33	100
$1.23 \cdot 10^5$	0.33	200
$1.18 \cdot 10^5$	0.33	300
$1.13 \cdot 10^5$	0.33	400
$1.06 \cdot 10^5$	0.33	500
95,000	0.33	600
86,000	0.33	700

Table A.7: Young modulus and Poisson's coefficient as a function of temperature for tungsten, OFHC-Cu and CuCrZr-IG.

Tungsten	
Density [t mm^{-3}]	Temperature [°C]
$1.93 \cdot 10^{-8}$	20
$1.93 \cdot 10^{-8}$	100
$1.93 \cdot 10^{-8}$	200
$1.92 \cdot 10^{-8}$	300
$1.92 \cdot 10^{-8}$	400
$1.92 \cdot 10^{-8}$	500
$1.92 \cdot 10^{-8}$	600
$1.91 \cdot 10^{-8}$	700
$1.91 \cdot 10^{-8}$	800
$1.91 \cdot 10^{-8}$	900
$1.9 \cdot 10^{-8}$	1,000
$1.9 \cdot 10^{-8}$	1,100
$1.9 \cdot 10^{-8}$	1,200

OFHC-Cu	
Density [t mm^{-3}]	Temperature [°C]
$8.94 \cdot 10^{-9}$	20
$8.93 \cdot 10^{-9}$	50
$8.9 \cdot 10^{-9}$	100
$8.88 \cdot 10^{-9}$	150
$8.85 \cdot 10^{-9}$	200
$8.83 \cdot 10^{-9}$	250
$8.8 \cdot 10^{-9}$	300
$8.77 \cdot 10^{-9}$	350
$8.74 \cdot 10^{-9}$	400
$8.71 \cdot 10^{-9}$	450
$8.68 \cdot 10^{-9}$	500
$8.65 \cdot 10^{-9}$	550
$8.61 \cdot 10^{-9}$	600
$8.57 \cdot 10^{-9}$	650
$8.54 \cdot 10^{-9}$	700
$8.5 \cdot 10^{-9}$	750
$8.45 \cdot 10^{-9}$	800
$8.41 \cdot 10^{-9}$	850
$8.36 \cdot 10^{-9}$	900
$8.32 \cdot 10^{-9}$	950
$8.27 \cdot 10^{-9}$	1,000

CuCrZr-IG	
Density [t mm^{-3}]	Temperature [°C]
$8.9 \cdot 10^{-9}$	20
$8.86 \cdot 10^{-9}$	100
$8.82 \cdot 10^{-9}$	200
$8.77 \cdot 10^{-9}$	300
$8.72 \cdot 10^{-9}$	400
$8.67 \cdot 10^{-9}$	500

Table A.8: Density as a function of temperature for tungsten, OFHC-Cu and CuCrZr-IG.

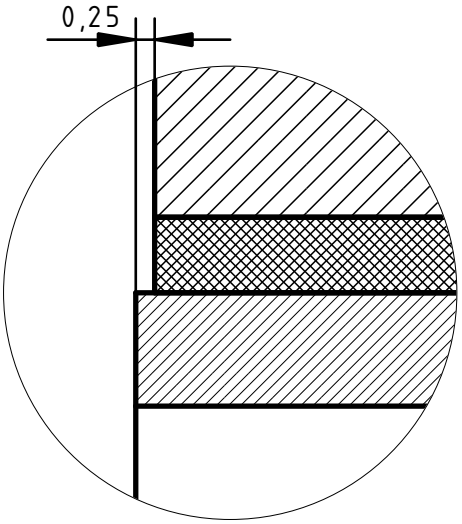

Scale 10:1

Detail A

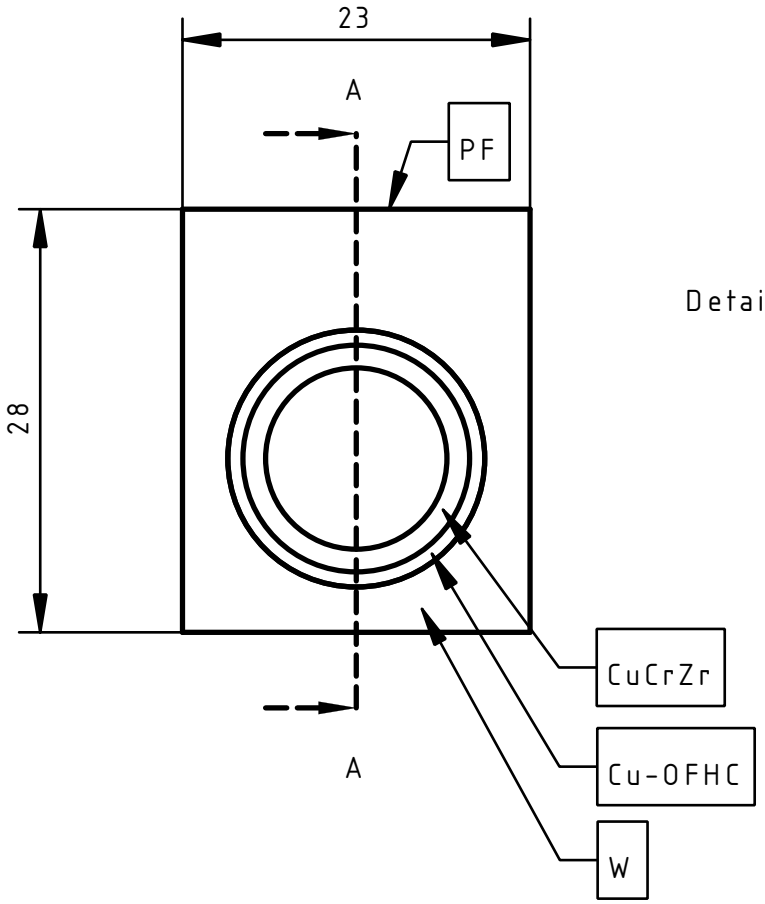

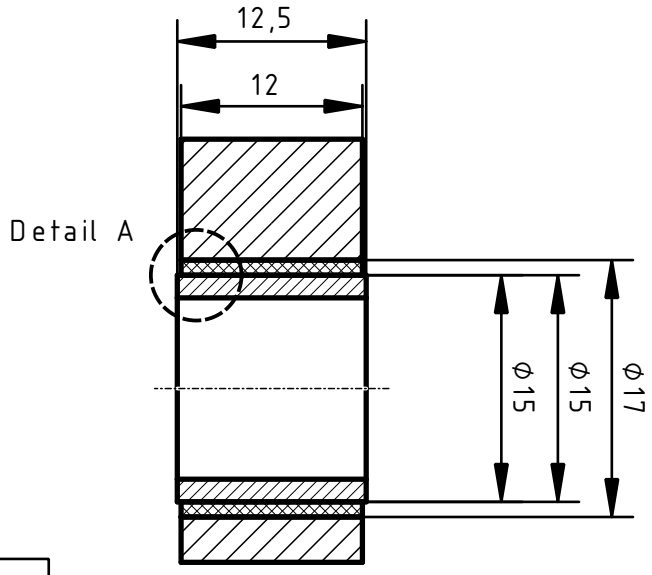

Section A - A

PF indicates the plasma facing side

Author: Fernando Oleo Blanco Appr.: Jeong-Ha You	Legal owner: EUROfusion	Scale: M 2:1 Toler.:-	Sheet: 1 of 1 Size: A4
TITLE: Divertor monoblock design		Part material: Indicated Part number: -	
		Drawing no.: 1.1	
Document type: Descriptive design		Date: 2022-06-22	Revision: REV A

Appendix B

Auxiliary Abaqus subroutines

B.1 `CREEP` subroutine

The `CREEP` subroutine allows the user to define arbitrary models for creep and swelling. Refer to the Abaqus' user documentation [21] for more information.

Several creep models for different materials can be implemented into a single `CREEP` subroutine with the use of the `CNAME` variable, which contains the name of the material of the node that is being computed. An example of this setup is given in Listing B.2.

Listing B.1: Abaqus' `CREEP` subroutine used to model the creep of OFHC-Cu. The parameter `AN` controls the deviatoric stress', $\tilde{\sigma}$, exponent n as discussed in subsection 2.5.2.

```
0  CCCCCCCCCCCCCCCCCCCCCCCCCCCCCCCCCCCCCCCCCCC
   C
   C FILE: COMPUTE CREEP OF CU-OFHC AND CUCRZR
   C AUTHOR: FERNANDO OLEO BLANCO
   C LICENSE: BSD-2-Clause
5  C FOR MORE INFORMATION ABOUT THE LICENSE, VISIT
   C https://spdx.org/licenses/BSD-2-Clause.html
   C YEAR: 2022
   C GOAL: IMPROVE THE MODELISATION OF SAID MATERIALS
   C FRAMEWORK: TUM/ICAI MASTER THESIS
10 C CONTACT EMAIL: fernando.oleo@tum.de
   C                fernando.oleo@alu.comillas.edu
   C INFORMATION REGARDING SOURCES FOR THE DATA
   C SHOULD BE INSIDE EACH MATERIALS SUBROUTINE
   C
15 C IMPORTANT INFORMATION
   C
   C UNITS
   C THE UNITS USED FOR THIS SUBROUTINE ASSUME AS INPUTS
   C MILLIMETERS FOR UNIT LENGTH
20 C NEWTONS FOR FORCE
   C DEGREE CENTIGRADE (C) FOR TEMPERATURE
   C SECONDS FOR TIME
   C
   C NOTES
25 C THIS FILE USES FORTRAN IMPLICIT TYPING
   C THIS MEANS THAT VARIABLES WHICH START WITH
```

```
C I, J, K, L, M, or N ARE TREATED AS INTEGERS
C AND EVERY OTHER VARIABLE IS TREATED AS A REAL
C
C THE CREEP SUBROUTINE, WHICH IS THE ONE CALLED BY
C ABAQUS, IS AT THE BOTTOM OF THIS FILE
C
C THE COMPILER USED FOR THIS FILE IS THE
C INTEL ONEAPI HPC FORTRAN COMPILER
C
C THIS FILE REQUIRES A FORTRAN 2008 CAPABLE COMPILER!
C
C THE INTEL ONEAPI PLATFORM IS FREE TO USE
C IT WAS CONFIGURED AS EXPLAINED IN THIS VIDEO
C https://www.youtube.com/watch?v=WPA-V_qEt_w
C HOWEVER, THE FOLLOWING LINE WAS USED TO SET THE COMPILER'S
C SETTINGS (IN ORDER TO GAIN MORE PERFORMANCE)
C compile_fortran += ['/names:lowercase', '/QxHost', '/O3', '/fp:fast=2',]
C THE DOCUMENTATION FOR INTEL'S COMPILER OPTIONS CAN BE FOUND AT
C https://www.intel.com/content/www/us/en/develop/documentation/fortran-compiler-oneapi-dev-
    guide-and-reference/top/compiler-reference/compiler-options/alphabetical-list-of-compiler-
    options.html
C THE CHOSEN OPTIONS ARE A CLOSE APPROXIMATION TO "/fast"
C BUT SINCE "/fast" WAS GIVING ME ERRORS, THEY WERE INDIVIDUALLY SELECTED
C
CCCCCCCCCCCCCCCCCCCCCCCCCCCCCCCCCCCCCCCC
C
C CREEP COMPUTATION FOR CU-OFHC
      SUBROUTINE CREEP(DECRA,DESWA,STATEV,SERD,EC,ESW,P,QTILD,
     1 TEMP,DTEMP,PREDEF,DPRED,TIME,DTIME,CMNAME,LEXIMP,LEND,
     2 COORDS,NSTATV,NOEL,NPT,LAYER,KSPT,KSTEP,KINC)
C
      INCLUDE 'ABA_PARAM.INC'
C
      CHARACTER*80 CMNAME
C
      DIMENSION DECRA(5),DESWA(5),STATEV(*),PREDEF(*),DPRED(*),
     1 TIME(3),EC(2),ESW(2),COORDS(*)
C
C MODEL AND PARAMETERS TAKEN FROM
C https://experts.illinois.edu/en/publications/modeling-creep-and-fatigue-of-copper-alloys
C "Modeling creep and fatigue of copper alloys"
C THE INDICATED RANGE IS FOR:
C TEMPERATURE: 400 TO 700 C
C STRESS: 15 TO 105 MPA
C
C ONLY SECONDARY CREEP RATE (ALSO KNOWN AS MINIMUM OR STEADY)
C SINCE THE AVAILABILITY OF PRIMARY CREEP IS NOT CLEAR/GOOD
C WE USE THE NORTON-BAILEY LAW
C
      A=38.8
      AN=4.8
C ACTIVATION ENERGY FOR SELF DIFUSSION IN J*MOL-1
      ENACT=197E3
C UNIVERSAL GAS CONSTANT IN J*MOL-1*K-1
```

```
      R=8.31432
C THE ARRHENIUS TERM REQUIRES THE TEMPERATURE IN ABSOLUTE TERMS, IN K
      TEMPABS = TEMP+273.15
C
C CONSTANT TERM. SCALAR, ARRHENIUS AND TIME
      CONST = A*EXP(-ENACT/(R*TEMPABS))*DTIME
C STRESS TERM
      SIGMA = QTILD**AN
C
      DECRA(1) = CONST*SIGMA
      IF(LEXIMP.EQ.1) THEN
C REUSE COMPUTED TERM
C DERIVATIVE IS CONST*AN*(QTILD**(AN-1))
C QTILD**(AN-1) .EQ. SIGMA/QTILD... BUT DO NOT USE THAT!
C SIGMA/QTILD IS INF IF QTILD IS 0, WHICH IT IS AT THE BEGINNING
C I COULD DO AN INITIAL SETUP FOR THE VARIABLE, BUT IT IS NOT WORTH IT
       DECRA(5) = CONST*AN*QTILD**(AN-1)
      END IF
C
C DEBUG INFO
C      WRITE(7,*) "CU-OFHC CREEP CALCULATION:"
C      WRITE(7,*) "DECRA(1): ", DECRA(1), " AND DECRA(5): ", DECRA(5)
C
      RETURN
      END
C
```

Listing B.2: Abaqus' CREEP subroutine example for several materials.

```
C
C MAIN CREEP SUBROUTINE, CALLED BY ABAQUS
C
      SUBROUTINE CREEP(DECRA,DESWA,STATEV,SERD,EC,ESW,P,QTILD,
     1 TEMP,DTEMP,PREDEF,DPRED,TIME,DTIME,CMNAME,LEXIMP,LEND,
     2 COORDS,NSTATV,NOEL,NPT,LAYER,KSPT,KSTEP,KINC)
C
      INCLUDE 'ABA_PARAM.INC'
C
      CHARACTER*80 CMNAME
C
      DIMENSION DECRA(5),DESWA(5),STATEV(*),PREDEF(*),DPRED(*),
     1 TIME(3),COORDS(*),EC(2),ESW(2)
C
C DOCUMENTATION FOR THIS SUBROUTINE CAN BE FOUND IN
C https://abaqus-docs.mit.edu/2017/English/SIMACAESUBRefMap/simasub-c-creep.htm
C
C
C MATERIAL INFORMATION
C NAMES OF THE MATERIALS CAN BE CHANGED BELOW IN THEIR DEFINITION
C
C WE BREAK UP THE CREEP SUBROUTINE INTO SEVERAL OTHERS TO ALLOW
C FOR MULTIPLE MATERIALS TO BE DEFINED
C
C SELECT MATERIAL TO COMPUTE CREEP
C
```

```
C USE "MODERN" FORTRAN 95 FEATURES
C
C DEFINE MATERIAL NAMES
C
C
      CHARACTER, PARAMETER :: CU_NAME = "ITER Cu You-harden for WPDIV phase II"
      CHARACTER, PARAMETER :: CUCRZR_NAME = "CuCrZr_ITER_A"
C
C SELECT SUBROUTINE DEPENDING ON THE MATERIAL BEING COMPUTED
C
      IF (CMNAME(1:LEN(CU_NAME)) .EQ. CU_NAME) THEN
            CALL CREEP_CU(DECRA,DESWA,STATEV,SERD,EC,ESW,P,QTILD,
     1 TEMP,DTEMP,PREDEF,DPRED,TIME,DTIME,CMNAME,LEXIMP,LEND,
     2 COORDS,NSTATV,NOEL,NPT,LAYER,KSPT,KSTEP,KINC)
C            WRITE(7,*) "CREEP SUBROUTINE: COMPUTED CU CREEP"
      ELSE IF(CMNAME(1:LEN(CUCRZR_NAME)) .EQ. CUCRZR_NAME) THEN
            CALL CREEP_CUCRZR(DECRA,DESWA,STATEV,SERD,EC,ESW,P,QTILD,
     1 TEMP,DTEMP,PREDEF,DPRED,TIME,DTIME,CMNAME,LEXIMP,LEND,
     2 COORDS,NSTATV,NOEL,NPT,LAYER,KSPT,KSTEP,KINC)
C            WRITE(7,*) "CREEP SUBROUTINE: COMPUTED CUCRZR CREEP"
      ELSE
C
C MATERIAL NOT IN THE SELECTION
C WRITE ERROR
C THE ERROR GETS PRINTED IN THE .MSG FILE
C FOR MORE INFORMATION ON THE FILE DESCRIPTOR NUMBERS USED BY
C ABAQUS, SEE
C https://abaqus-docs.mit.edu/2017/English/SIMACAEEXCRefMap/simaexc-c-unitnumbers.htm
C
            WRITE(7,*) "CREEP SUBROUTINE: MATERIAL NOT FOUND"
            WRITE(7,*) "MATERIAL NAME THAT WAS RECEIVED"
            WRITE(7,*) CNAME
            WRITE(7,*) "PLEASE, FIX THE NAME OF THE MATERIAL IN THE FORTRAN CODE"
      END IF
C
      RETURN
      END
```

B.2 `USDFLD`, deletion subroutines

The `USDFLD` allows the specification and modification of user defined material fields. The subroutine is commonly used for Functionally Graded Materials (FGM), where material properties vary with the defined fields. In this study, the field which we are controlling is the built-in, user-selectable "element deletion field". In both subroutines, Listing B.3 and B.4, this field is selected by the `NUM_DELETE` variable. Element deletion has to be enabled during mesh creation. The field number for element deletion has to be indicated in the Abaqus' setup file, under the material definition in the `*Depvar` section. For example, in the input file `.inp` it should appear as:

`[...]`

```
Finite element definition
Group definitions
Group assignment
[...]
**
** ELEMENT CONTROLS
**
*Section Controls, name=EC-1, ELEMENT DELETION=YES
1., 1., 1.
[...]
[Inside the material definition]
*Depvar, delete=1
1,
```

In this case, the element deletion has been enabled in the `EC-1` group. The field variable number `delete=1` controls the field number driving element deletion. We are creating a single field as indicated by `Depvar`, which will be the one driving the element deletion. Therefore, the variable `NUM_DELETE` in the `USDFLD` subroutine is set to "1". All the Abaqus' parameters are accessible through the Graphical User Interface (GUI).

Refer to the Abaqus' documentation [21] for more information on the use of the `USDFLD` subroutine.

Listing B.3: Abaqus' `USDFLD` subroutine used to perform a mock-up FIB-DIC (Focused Ion Beam – Digital Image Correlation) operation. The geometrical parameters are not representative of those used in real FIB–DIC experiments. The code is explained in Algorithm 3 and visualised in Figure 3.2.

```
0  CCCCCCCCCCCCCCCCCCCCCCCCCCCCCCCCCCCCCCCCCC
   C
   C FILE: ELEMENT DELITION SUBROUTINE, DESIGNED FOR FIB
   C AUTHOR: FERNANDO OLEO BLANCO
   C LICENSE: BSD-2-Clause
5  C FOR MORE INFORMATION ABOUT THE LICENSE, VISIT
   C https://spdx.org/licenses/BSD-2-Clause.html
   C YEAR: 2022
   C GOAL: SIMULATE REMOVAL OF MATERIAL
   C FRAMEWORK: TUM/ICAI MASTER THESIS
10 C CONTACT EMAIL: fernando.oleo@tum.de
   C                fernando.oleo@alu.comillas.edu
   C INFORMATION REGARDING SOURCES FOR THE DATA
   C SHOULD BE INSIDE EACH SUBROUTINE
   C
15 C IMPORTANT INFORMATION
   C
   C UNITS
   C THE UNITS USED FOR THIS SUBROUTINE ASSUME AS INPUTS
   C MILLIMETERS FOR UNIT LENGTH
20 C NEWTONS FOR FORCE
   C DEGREE CENTIGRADE (C) FOR TEMPERATURE
   C SECONDS FOR TIME
   C
```

```
C NOTES
C THIS FILE USES FORTRAN IMPLICIT TYPING
C THIS MEANS THAT VARIABLES WHICH START WITH
C I, J, K, L, M, or N ARE TREATED AS INTEGERS
C AND EVERY OTHER VARIABLE IS TREATED AS A REAL
C
C THE COMPILER USED FOR THIS FILE IS THE
C INTEL ONEAPI HPC FORTRAN COMPILER
C
C THIS FILE REQUIRES A FORTRAN 2008 CAPABLE COMPILER!
C
C THE INTEL ONEAPI PLATFORM IS FREE TO USE
C IT WAS CONFIGURED AS EXPLAINED IN THIS VIDEO
C https://www.youtube.com/watch?v=WPA-V_qEt_w
C HOWEVER, THE FOLLOWING LINE WAS USED TO SET THE COMPILER'S
C SETTINGS (IN ORDER TO GAIN MORE PERFORMANCE)
C compile_fortran += ['/names:lowercase', '/QxHost', '/O3', '/fp:fast=2',]
C THE DOCUMENTATION FOR INTEL'S COMPILER OPTIONS CAN BE FOUND AT
C https://www.intel.com/content/www/us/en/develop/documentation/fortran-compiler-oneapi-dev-
    guide-and-reference/top/compiler-reference/compiler-options/alphabetical-list-of-compiler-
    options.html
C THE CHOSEN OPTIONS ARE A CLOSE APPROXIMATION TO "/fast"
C BUT SINCE "/fast" WAS GIVING ME ERRORS, THEY WERE INDIVIDUALLY SELECTED
C
CCCCCCCCCCCCCCCCCCCCCCCCCCCCCCCCCCCCCCCCCC
C
C THE LOGIC OF THE DELETION SUBROUTINE IS AS FOLLOWS
C
C 1. SETUP
C 1.1 CONSTRUCT THE GEOMETRICAL SPACE FROM WHERE THE MATERIAL
C     WILL BE DELETED
C 1.2 DECOMPOSE THE GAUSS POINT INFORMATION INTO A VECTOR
C 2. COMPUTATION
C 2.1 CHECK WHETHER WE ARE IN THE "DELETING" STEP. THIS IS DONE
C     TO ALLOW THIS SUBROUTINE TO WORK ON MULTISTEP SIMULATIONS.
C     SET THE VARIABLE "NUM_STEP" TO THE STEP NUMBER YOU WANT.
C     IT STARTS COUNTING FROM 1 (FIRST STEP THAT IS NOT "INITIAL"
C     IS THE NUMBER 1, SECOND IS NUMBER 2...)
C 2.2 HAVE A DISPLACEMENT VECTOR THAT WILL MOVE THAT GEOMETRICAL
C     SPACE OVER THE STEP TIME. THE DISPLACEMENT IS PROPORTIONAL
C     TO THE SIZE OF THE DISPLACEMENT VECTOR AND THE SIMULATION
C     TIME!!
C 2.3 (FOR THE SEMI-INFINITE CYLINDER) CHECK WHETHER THE GAUSS
C     POINT IS IN "BEHIND" THE FRONTAL BASE OF THE CYLINDER
C 2.4 IF TRUE, CHECK THE DISTANCE FROM THE POINT TO THE AXIS
C 2.5 IF THE DISTANCE FALLS BETWEEN THE OUTER AND INNER DIAMETERS
C     "DELETE THE ELEMENT", AKA, SET THE FIELDS TO THE DELETION VALUE
C 2.6 EXIT
C
CCCCCCCCCCCCCCCCCCCCCCCCCCCCCCCCCCCCCCCCCC
C
C LIMITATIONS AND ADVANTAGES
C
C LIMITATIONS
```

```
C THE BASE OF THE CYLINDER OR GEOMETRICAL BODY IS NOT PARAMETRISED.
C THIS IS A PROBLEM BECAUSE THE PART CAN MOVE AND LOSE CONCENTRICITY
C WITH THE CYLINDER, MAKING THE ELIMINATION LESS ACCURATE
C
C THE MOVEMENT OF THE "GEOMETRICAL BODY" IS DEFINED BY A DISPLACEMENT
C VECTOR AND TIME. THIS MEANS THAT IF YOU CHANGE THE SIZE OF ANY OF THOSE
C TWO VALUES, THE "GEOMETRICAL BODY" MAY BE DISPLACED A DIFFERENT AMOUNT
C
C ADVANTAGES
C THE SUBROUTINE CAN STILL BE USED FOR OTHER GENERIC FIELDS. THIS WOULD
C ALLOW, IN THE CASE OF FIB, THE MODELING OF MATERIAL DAMAGE/PROPERTY
C CHANGE IN THE SURROUNDING AREA/VOLUME OF FIB
C
CCCCCCCCCCCCCCCCCCCCCCCCCCCCCCCCCCCCCCCCC
C
C ABAQUS SETUP AND REQUIREMENTS. IMPORTANT!!!
C
C IN ORDER FOR THE DELETION OF ELEMENTS TO TAKE PLACE, THE ABAQUS FILE
C REQUIRES SPECIAL TREATMENT.
C
C 1. ELEMENT DELETION HAS TO BE ENABLED DURING MESH CREATION. THIS CAN BE
C    DONE IN THE GUI UNDER THE MESH > ELEMENT TYPE > ELEMENT DELETION: YES
C 2. IN THE MATERIAL DEFINITION THE USER HAS TO DO THE FOLLOWING
C 2.1 ENABLE VARIABLE DEPENDENCY (FIELD DEPENDENCY). DOCUMENTATION FOR THIS
C     OPTION CAN BE FOUND IN: https://abaqus-docs.mit.edu/2017/English/SIMACAEKEYRefMap/simakey-
    r-depvar.htm
C 2.1.1 THIS IS DONE BY GOING INTO THE MATERIAL DEFINITION: GENERAL > DEPVAR
C 2.1.2 INDICATE HOW MANY SOLUTION DEPENDENT VARIABLES THE MATERIAL WILL HAVE
C       (AT LEAST ONE!)
C 2.1.3 GIVE THE FIELD NUMBER THAT WILL DRIVE THE ELEMENT DELETION (THIS IS
C       PARAMETRISED IN THIS SUBROUTINE UNDER THE VARIABLE NAME "NUM_DELETE"
C 2.2 ENABLE USER DEFINED FIELD BY SELECTING GENERAL > USER DEFINED FIELD
C 2.3 IMPORTANT! ABAQUS SEEMS TO OPTIMISE OUT THE SUBROUTINE IF IT DOES NOT FIND
C     A MATERIAL PROPERTY THAT EXPLICITLY DEPENDS ON A FIELD VARIABLE! FOR THAT
C     REASON, WE NEED TO ENABLE A FIELD DEPENDENCY IN A MATERIAL PROPERTY.
C     MY RECOMENDATION FOR MECHANICAL PROBLEMS IS TO MAKE THE
C     ELECTRICAL > CONDUCTIVITY BE DEPENDENT ON A FIELD. GIVE A FIELD VARIABLE
C     AND ADD ANOTHER COLUMN. GIVE DUMMY VALUES TO THE CONDUCTIVITY (.NE. 0)
C     AND IN THE VARIABLE FIELD USE TWO DIFFERENT VALUES!
C     VALUES SUCH AS 0 AND 1 ARE RECOMMENDED
C
CCCCCCCCCCCCCCCCCCCCCCCCCCCCCCCCCCCCCCCCC
C
C ABAQUS SUBROUTINE DOCUMENTATION
C https://abaqus-docs.mit.edu/2017/English/SIMACAESUBRefMap/simasub-c-usdfld.htm#simasub-c-
    usdfld
C
      SUBROUTINE USDFLD(FIELD,STATEV,PNEWDT,DIRECT,T,CELENT,
     1 TIME,DTIME,CMNAME,ORNAME,NFIELD,NSTATV,NOEL,NPT,LAYER,
     2 KSPT,KSTEP,KINC,NDI,NSHR,COORD,JMAC,JMATYP,MATLAYO,
     3 LACCFLA)
C
      INCLUDE 'ABA_PARAM.INC'
C
```

```
      CHARACTER*80 CMNAME,ORNAME
      CHARACTER*3  FLGRAY(15)
      DIMENSION FIELD(NFIELD),STATEV(NSTATV),DIRECT(3,3),
     1 T(3,3),TIME(2)
      DIMENSION ARRAY(15),JARRAY(15),JMAC(*),JMATYP(*),
     1 COORD(*)
C
CCC Define constants
C
C Field number that will drive the deletion
      PARAMETER NUM_DELETE=1
C Step for which the deletion will be active
      PARAMETER NUM_STEP=2
C Define the geometrical espace from which material will be eliminated
C We define a hollow cylinder
      PARAMETER OUT_RADIUS=0.3
      PARAMETER INN_RADIUS=0.15
      DIMENSION CENTRE_T(3)
C Starting point for the deletion
      DIMENSION ORIGIN(3)
C Vector of movement
      DIMENSION DISPLACEMENT_V(3)
C Vector in which to decompose and recompose the coordinates of the Gauss element
      DIMENSION GAUSS_ELEM(3)
C Vecotrial distance
      DIMENSION VEC_DIST(3)
C
C IMPORTANT NOTES
C THE DESCRIPTION OF THE "HOLLOW" CYLINDER ASSUMES THAT THE
C AXIS OF ROTATION IS ALIGNED TO THAT OF THE DISPLACEMENT.
C THIS MEAN THAT THE CYLINDER CAN ONLY MOVE AXIALY. IT HAS _NO_
C ROTATION OF ANY KIND AND CANNOT MOVE PERPEDICULAR TO ITS AXIS
C
C MODIFY THESE ACCORDINGLY
C Origin/base of the cylinder, selected coordinates
      ORIGIN = (/0.0, 8.0, 0.5/)
C Vector of displacement, selected unit vector
      DISPLACEMENT_V = (/-1.0, 0.0, 0.0/)
C
C Transform the Gauss coordinates to the vector we needed
      GAUSS_ELEM = (/COORD(1), COORD(2), COORD(3)/)
C
C ONLY COMPUTE IF WE ARE IN THE SELECTED STEP!
C
      IF (KSTEP .EQ. NUM_STEP) THEN
C Define the geometrical space from which material will be eliminated
C Current centre
C Time(1) is the time since the beginning from this step
        CENTRE_T = ORIGIN + DISPLACEMENT_V*TIME(1)
C
CCC Calculate distance from the material centre to the "deleting" hollow cylinder
C Calculate projected distance over the cylinder axis
C with vector DISPLACEMENT_V and centre CENTRE_T
        VEC_DIST = GAUSS_ELEM - CENTRE_T
```

```
        PROJECTION = DOT_PRODUCT(VEC_DIST, DISPLACEMENT_V)
C Check that the point is "behind" the frontral face, if it is, then check for elimination
        IF (PROJECTION .LE. 0.0) THEN
C Euclidean vector norm. NORM2 is a built in Fortran 2008 routine
          DISTANCE = NORM2(VEC_DIST - PROJECTION*DISPLACEMENT_V)
C We delete the element if it is in the hollow cylinder
          IF (DISTANCE .LT. OUT_RADIUS .AND. DISTANCE .GT. INN_RADIUS) THEN
C The element delition variable is set to 1 by default. Value 0 indicates deletion
            FIELD(NUM_DELETE) = 0
            STATEV(NUM_DELETE) = FIELD(NUM_DELETE)
C         WRITE(7,*) 'ELEMENT ', NOEL, ' WAS DELETED'
          ENDIF
        ENDIF
C
      ENDIF
C      WRITE(7,*) 'FERNANDO: THE CODE IS RUNNING'
      RETURN
      END
```

Listing B.4: Abaqus' USDFLD subroutine used to perform the horizontal cutting operation as explained in chapter 3.

```
CCCCCCCCCCCCCCCCCCCCCCCCCCCCCCCCCCCCCCCCCC
C
C
C THE CODE BELOW WAS ORIGINALLZ CREATED FOR A FIB ANALYSIS AND THE GEOMETRY
C DELETED WAS IN THE SHAPE OF A CYLINDER:
C FOR THIS FILE, THE GEOMETRY IS A SEMI-INFINITE HEXAHEDRA
C
C
CCCCCCCCCCCCCCCCCCCCCCCCCCCCCCCCCCCCCCCCCC
C
C FILE: ELEMENT DELITION SUBROUTINE, DESIGNED FOR FIB
C AUTHOR: FERNANDO OLEO BLANCO
C LICENSE: BSD-2-Clause
C FOR MORE INFORMATION ABOUT THE LICENSE, VISIT
C https://spdx.org/licenses/BSD-2-Clause.html
C YEAR: 2022
C GOAL: SIMULATE REMOVAL OF MATERIAL
C FRAMEWORK: TUM/ICAI MASTER THESIS
C CONTACT EMAIL: fernando.oleo@tum.de
C                fernando.oleo@alu.comillas.edu
C INFORMATION REGARDING SOURCES FOR THE DATA
C SHOULD BE INSIDE EACH SUBROUTINE
C
C IMPORTANT INFORMATION
C
C UNITS
C THE UNITS USED FOR THIS SUBROUTINE ASSUME AS INPUTS
C MILLIMETERS FOR UNIT LENGTH
C NEWTONS FOR FORCE
C DEGREE CENTIGRADE (C) FOR TEMPERATURE
C SECONDS FOR TIME
C
```

```
C NOTES
C THIS FILE USES FORTRAN IMPLICIT TYPING
C THIS MEANS THAT VARIABLES WHICH START WITH
C I, J, K, L, M, or N ARE TREATED AS INTEGERS
C AND EVERY OTHER VARIABLE IS TREATED AS A REAL
C
C THE COMPILER USED FOR THIS FILE IS THE
C INTEL ONEAPI HPC FORTRAN COMPILER
C
C THIS FILE REQUIRES A FORTRAN 2008 CAPABLE COMPILER!
C
C THE INTEL ONEAPI PLATFORM IS FREE TO USE
C IT WAS CONFIGURED AS EXPLAINED IN THIS VIDEO
C https://www.youtube.com/watch?v=WPA-V_qEt_w
C HOWEVER, THE FOLLOWING LINE WAS USED TO SET THE COMPILER'S
C SETTINGS (IN ORDER TO GAIN MORE PERFORMANCE)
C compile_fortran += ['/names:lowercase', '/QxHost', '/O3', '/fp:fast=2',]
C THE DOCUMENTATION FOR INTEL'S COMPILER OPTIONS CAN BE FOUND AT
C https://www.intel.com/content/www/us/en/develop/documentation/fortran-compiler-oneapi-dev-
    guide-and-reference/top/compiler-reference/compiler-options/alphabetical-list-of-compiler-
    options.html
C THE CHOSEN OPTIONS ARE A CLOSE APPROXIMATION TO "/fast"
C BUT SINCE "/fast" WAS GIVING ME ERRORS, THEY WERE INDIVIDUALLY SELECTED
C
CCCCCCCCCCCCCCCCCCCCCCCCCCCCCCCCCCCCCCCCCC
C
C THE LOGIC OF THE DELETION SUBROUTINE IS AS FOLLOWS
C
C 1. SETUP
C 1.1 CONSTRUCT THE GEOMETRICAL SPACE FROM WHERE THE MATERIAL
C     WILL BE DELETED
C 1.2 DECOMPOSE THE GAUSS POINT INFORMATION INTO A VECTOR
C 2. COMPUTATION
C 2.1 CHECK WHETHER WE ARE IN THE "DELETING" STEP. THIS IS DONE
C     TO ALLOW THIS SUBROUTINE TO WORK ON MULTISTEP SIMULATIONS.
C     SET THE VARIABLE "NUM_STEP" TO THE STEP NUMBER YOU WANT.
C     IT STARTS COUNTING FROM 1 (FIRST STEP THAT IS NOT "INITIAL"
C     IS THE NUMBER 1, SECOND IS NUMBER 2...)
C 2.2 HAVE A DISPLACEMENT VECTOR THAT WILL MOVE THAT GEOMETRICAL
C     SPACE OVER THE STEP TIME. THE DISPLACEMENT IS PROPORTIONAL
C     TO THE SIZE OF THE DISPLACEMENT VECTOR AND THE SIMULATION
C     TIME!!
C 2.3 (FOR THE SEMI-INFINITE CYLINDER) CHECK WHETHER THE GAUSS
C     POINT IS IN "BEHIND" THE FRONTAL BASE OF THE CYLINDER
C 2.4 IF TRUE, CHECK THE DISTANCE FROM THE POINT TO THE AXIS
C 2.5 IF THE DISTANCE FALLS BETWEEN THE OUTER AND INNER DIAMETERS
C     "DELETE THE ELEMENT", AKA, SET THE FIELDS TO THE DELETION VALUE
C 2.6 EXIT
C
CCCCCCCCCCCCCCCCCCCCCCCCCCCCCCCCCCCCCCCCCC
C
C LIMITATIONS AND ADVANTAGES
C
C LIMITATIONS
```

```
C THE BASE OF THE CYLINDER OR GEOMETRICAL BODY IS NOT PARAMETRISED.
C THIS IS A PROBLEM BECAUSE THE PART CAN MOVE AND LOSE CONCENTRICITY
C WITH THE CYLINDER, MAKING THE ELIMINATION LESS ACCURATE
C
C THE MOVEMENT OF THE "GEOMETRICAL BODY" IS DEFINED BY A DISPLACEMENT
C VECTOR AND TIME. THIS MEANS THAT IF YOU CHANGE THE SIZE OF ANY OF THOSE
C TWO VALUES, THE "GEOMETRICAL BODY" MAY BE DISPLACED A DIFFERENT AMOUNT
C
C ADVANTAGES
C THE SUBROUTINE CAN STILL BE USED FOR OTHER GENERIC FIELDS. THIS WOULD
C ALLOW, IN THE CASE OF FIB, THE MODELING OF MATERIAL DAMAGE/PROPERTY
C CHANGE IN THE SURROUNDING AREA/VOLUME OF FIB
C
CCCCCCCCCCCCCCCCCCCCCCCCCCCCCCCCCCCCCCCCCC
C
C ABAQUS SETUP AND REQUIREMENTS. IMPORTANT!!!
C
C IN ORDER FOR THE DELETION OF ELEMENTS TO TAKE PLACE, THE ABAQUS FILE
C REQUIRES SPECIAL TREATMENT.
C
C 1. ELEMENT DELETION HAS TO BE ENABLED DURING MESH CREATION. THIS CAN BE
C    DONE IN THE GUI UNDER THE MESH > ELEMENT TYPE > ELEMENT DELETION: YES
C 2. IN THE MATERIAL DEFINITION THE USER HAS TO DO THE FOLLOWING
C 2.1 ENABLE VARIABLE DEPENDENCY (FIELD DEPENDENCY). DOCUMENTATION FOR THIS
C     OPTION CAN BE FOUND IN: https://abaqus-docs.mit.edu/2017/English/SIMACAEKEYRefMap/simakey-
    r-depvar.htm
C 2.1.1 THIS IS DONE BY GOING INTO THE MATERIAL DEFINITION: GENERAL > DEPVAR
C 2.1.2 INDICATE HOW MANY SOLUTION DEPENDENT VARIABLES THE MATERIAL WILL HAVE
C       (AT LEAST ONE!)
C 2.1.3 GIVE THE FIELD NUMBER THAT WILL DRIVE THE ELEMENT DELETION (THIS IS
C       PARAMETRISED IN THIS SUBROUTINE UNDER THE VARIABLE NAME "NUM_DELETE"
C 2.2 ENABLE USER DEFINED FIELD BY SELECTING GENERAL > USER DEFINED FIELD
C 2.3 IMPORTANT! ABAQUS SEEMS TO OPTIMISE OUT THE SUBROUTINE IF IT DOES NOT FIND
C     A MATERIAL PROPERTY THAT EXPLICITLY DEPENDS ON A FIELD VARIABLE! FOR THAT
C     REASON, WE NEED TO ENABLE A FIELD DEPENDENCY IN A MATERIAL PROPERTY.
C     MY RECOMENDATION FOR MECHANICAL PROBLEMS IS TO MAKE THE
C     ELECTRICAL > CONDUCTIVITY BE DEPENDENT ON A FIELD. GIVE A FIELD VARIABLE
C     AND ADD ANOTHER COLUMN. GIVE DUMMY VALUES TO THE CONDUCTIVITY (.NE. 0)
C     AND IN THE VARIABLE FIELD USE TWO DIFFERENT VALUES!
C     VALUES SUCH AS 0 AND 1 ARE RECOMMENDED
C
CCCCCCCCCCCCCCCCCCCCCCCCCCCCCCCCCCCCCCCCCC
C
C ABAQUS SUBROUTINE DOCUMENTATION
C https://abaqus-docs.mit.edu/2017/English/SIMACAESUBRefMap/simasub-c-usdfld.htm#simasub-c-
    usdfld
C
      SUBROUTINE USDFLD(FIELD,STATEV,PNEWDT,DIRECT,T,CELENT,
     1 TIME,DTIME,CMNAME,ORNAME,NFIELD,NSTATV,NOEL,NPT,LAYER,
     2 KSPT,KSTEP,KINC,NDI,NSHR,COORD,JMAC,JMATYP,MATLAYO,
     3 LACCFLA)
C
      INCLUDE 'ABA_PARAM.INC'
C
```

```
      CHARACTER*80 CMNAME,ORNAME
      CHARACTER*3  FLGRAY(15)
      DIMENSION FIELD(NFIELD),STATEV(NSTATV),DIRECT(3,3),
     1 T(3,3),TIME(2)
      DIMENSION ARRAY(15),JARRAY(15),JMAC(*),JMATYP(*),
     1 COORD(*)
C
CCC Define constants
C
C Field number that will drive the deletion
      PARAMETER NUM_DELETE=1
C Step for which the deletion will be active
      PARAMETER NUM_STEP=5
C Define the geometrical espace from which material will be eliminated
      PARAMETER DELTA_PLANE = 0.37
      DIMENSION CENTRE_T(3)
C Starting point for the deletion
      DIMENSION ORIGIN(3)
C Vector of movement
      DIMENSION DISPLACEMENT_V(3)
C Vector in which to decompose and recompose the coordinates of the Gauss element
      DIMENSION GAUSS_ELEM(3)
C Vecotrial distance
      DIMENSION VEC_DIST(3)
C
C MODIFY THESE ACCORDINGLY
C Origin/base of the semi-infinite hexahedra (cutting plane), selected coordinates
      ORIGIN = (/0.0, 0.0, 6.25/)
C Vector of displacement, selected unit vector
      DISPLACEMENT_V = (/0.0, 0.0, -6.5/)
C
C Transform the Gauss coordinates to the vector we needed
      GAUSS_ELEM = (/COORD(1), COORD(2), COORD(3)/)
C
C ONLY COMPUTE IF WE ARE IN THE SELECTED STEP!
C
      IF (KSTEP .EQ. NUM_STEP) THEN
C Define the geometrical space from which material will be eliminated
C Current centre
C Time(1) is the time since the beginning from this step
        CENTRE_T = ORIGIN + DISPLACEMENT_V*TIME(1)
C
CCC Calculate distance from the material cetre to the geometrical space
C
C CHECK IF THE POINT IS BELOW THE TOP PLANE .AND. ABOVE BOTTOM PLANE .AND. BEHIND THE ADVANCING
    FRONT
C HERE WE ARE OPTIMISING THE FACT THAT WE ARE CUTTING FROM THE Y=0 PLANE
        IF (GAUSS_ELEM(2) .LT. 0.0 .AND.
     1      GAUSS_ELEM(2) .GT. -DELTA_PLANE .AND.
     2      GAUSS_ELEM(3) .GT. CENTRE_T(3)) THEN
C The element delition variable is set to 1 by default. Value 0 indicates deletion
          FIELD(NUM_DELETE) = 0
          STATEV(NUM_DELETE) = FIELD(NUM_DELETE)
C         WRITE(7,*) 'ELEMENT ', NOEL, ' WAS DELETED'
```

```
        ENDIF
      ENDIF
C
C      WRITE(7,*) 'FERNANDO: THE CODE IS RUNNING'
      RETURN
      END
C
CCCCCCCCCCCCCCCCCCCCCCCCCCCCCCCCCCCCCCCCCC
```

Appendix C

Auxiliary data processing programs

Listing C.1: Maxima's code to process and calculate creep rate and accumulated creep data for a given temperature-stress history. The input is a CSV file generated from the Excel output that Abaqus can generate with its plug-in. Please, read the comments carefully, as the data needs to be cleaned before processing. Time, temperature and stress are the required inputs.

```
/* Automate the process of reading files and cleaning the data.
   Important! The data that is read has to have the following structure:
   1st column: time
   2nd column: stress
   3rd column: temperature
   ---
   The units are expected in mm, Newton, second, centigrades.
   ---
   Notes on maxima:
   It is very similar to Mathematica or Maple. It should be easy to read for
   anyone with experience in programming; although Maxima takes a more
   functional approach.
   Maxima uses ":" for assignment and ":=" for function definition
   A "$" at the end of a declarations supresses the output. A ";" does not.
*/
read_and_process_file(filename) := block([s, mat, result],
    /* Open file */
    tmp : openr(filename),
    /* Read contents of the .csv as a matrix */
    mat : read_matrix(tmp),
    /* Clean the data */
    result : clean_data(mat),
    result
) $

/* Delete repeated time column since Abaqus adds it to every output requested.
   Remember that Maxima starts counting from 1. */
clean_data(data) := submatrix(data,3) $

/* Trapezoidal integration for numerical data.
   Returns the integral of y over x. */
trapz(y, x) := block([acc, delta_x],
```

```
    acc : 0,
    for i : 1 thru (length(x) - 1) do (
        delta_x : x[i+1] - x[i],
        acc : acc + delta_x*0.5*(y[i]+y[i+1])
        ),
    acc
) $

/* Accumulated values from the trapezoidal integration.
   Useful when the integral of a computation has to be plotted.
   Returns a list of the integral values for each x. */
trapz_accumul(y,x) := block([delta_x, result],
    result : makelist(1, length(x)),
    result[1] : 0,
    for i : 1 thru (length(x) - 1) do (
        delta_x : x[i+1] - x[i],
        result[i+1] : result[i] + delta_x * 0.5 * (y[i]+y[i+1])
        ),
    result
) $

/* Accumulated values from the trapezoidal integration.
   Useful when the integral of a computation has to be plotted.
   Returns a list of the integral values for each x. */
upper_integral(y,x) := block([delta_x, result],
    result : makelist(1, length(x)),
    result[1] : 0,
    for i : 1 thru (length(x) - 1) do (
        delta_x : x[i+1] - x[i],
        result[i+1] : result[i] + delta_x * y[i+1]
        ),
    result
) $

/* Accumulated values from the trapezoidal integration.
   Useful when the integral of a computation has to be plotted.
   Returns a list of the integral values for each x. */
lower_integral(y,x) := block([delta_x, result],
    result : makelist(1, length(x)),
    result[1] : 0,
    for i : 1 thru (length(x) - 1) do (
        delta_x : x[i+1] - x[i],
        result[i+1] : result[i] + delta_x * y[i]
        ),
    result
) $

/* Compute creep evolution.
   The given data matrix must already have the creep rate included in its fourth column. */
compute_creep(matrix) := block([t, εdot, aux, creep, result],
    aux : transpose(matrix),
    t : first(aux),
    εdot : fourth(aux),
    creep : trapz_accumul(εdot, t)
```

```
    /* creep : upper_integral(εdot, t) */
    /* creep : lower_integral(εdot, t) */
) $

/* Compute final/total creep.
   The given data matrix must already have the creep rate included in its fourth column */
compute_total_creep(matrix) := block([t, εdot, aux, creep, result],
    aux : transpose(matrix),
    t : first(aux),
    εdot : fourth(aux),
    creep : trapz(εdot, t)
) $

/* Computes the creep rate for each instant.
   This function requires the data matrix and a function/expresion
   with which to compute the creep rate. */
compute_creep_rate(matrix, expr) := block([σ, T, creep_rate, result],
    σ : col(matrix, 2),
    T : col(matrix, 3),
    /* We need to transform the expression into a proper function to operate with it */
    define(fun(a,b), expr),
    creep_rate : fun(σ, T)
    /* Leaving the bottom code as reference as to how this may have worked */
    /* creep : apply(
            lambda([a, b], function(a,b)),
            [σ, T]), */
) $

/*
   Define the creep rate function
*/

/* Create dependencies for the different parameters. */
/* σ is the stress */
depends(σ, [t]) $
/* T is the temperature */
depends(T, [t]) $
/* A is the creep rate coefficient */
depends(A, [σ, T]) $
/* n is the stress exponent */
depends(n, [σ, T]) $
/* m is the time hardening constant */
depends(m, [σ, T]) $
/* Q is the activation energy for self-difussion */
depends(Q, [σ, T]) $

/* Define the creep rate function in its most general form.
    We use float() to force numerical output, same with %e. */
εdotfull(σ,T, n, Q, A, m, t) := float(A*σ^n*%e^(-Q/(8.31432*(T+273.15)))*t^m);

/* Simplify the creep rate expression to the parameters that we want to focus on. */
εdotsecondary(σ, T, n, Q) := εdotfull(σ, T, n, Q, 1, 0, 1) $

/* Simplify the creep rate expression to the parameters that we want to focus on. */
```

```
εdotsimple(σ, T, n) := εdotsecondary(σ, T, n, 197000) $

/* Read data file */
Data_cleaned : read_and_process_file("./org_cleaned_creep.csv") $

/* Define the stress exponent.
   Only needed for manual computatios. */
n_expo : 4.8 $

/* Generate creep rate data with the Abaqus information */
Creep_rate_data : addcol(Data_cleaned, compute_creep_rate(Data_cleaned, εdotsimple(σ, T, n_expo)
    )) $

/* Compute the accumulated creep and add it to the table */
Creep_data : addcol(Creep_rate_data, compute_creep(Creep_rate_data)) $

Creep_coefficient : 38.8 $
Creep_coefficient;
compute_total_creep(Creep_rate_data);

/*
   Auxiliary function to compute total creep as a function of the creep rate definition
*/
parametric_total_creep(data, n, Q) := block([creep_rate, total_creep],
    /* Compute the creep rate */
    creep_rate : transpose(compute_creep_rate(data, εdotsecondary(σ, T, n,Q))),
    /* Integrate it over time.
       We use first(creep_rate) to transform it from a Matrix to a list */
    total_creep : trapz(first(creep_rate), first(transpose(data)))
) $

/* Check that the parametric function works */
parametric_total_creep(Data_cleaned, 5, 197000);

/*
   Create parametric 3D plot
*/

/* plot3d(log(parametric_total_creep(Data_cleaned, x, y)), [x, 1, 10], [y, 197000*0.5,
    197000*1.5]); */;

/* Export parametric data to allow LaTeX plotting */

compute_parametric_n_Q_creep(data) := block([n_divisions, Q_divisions, n_min, n_max, Q_base,
    Q_min, Q_max, line, Data_export],
    /* Number of data points */
    n_divisions : 50,
    Q_divisions : 50,
    n_min : 1,
    n_max : 10,
    Q_base : 197000,
    Q_min : Q_base * 0.5,
    Q_max : Q_base * 1.5,
    /* Preallocate data */
```

```
    Data_export : makelist([i,i,i], i, 1, (n_divisions+1)*(Q_divisions+1)),
    /* Make computation purely numeric */
    numer : true,
    /* Line counter */
    line : 1,
    for n : 0 thru n_divisions do (
        for Q : 0 thru Q_divisions do (
            n_comp : n_min + n*(n_max-n_min)/n_divisions,
            Q_comp : Q_min + Q*(Q_max-Q_min)/Q_divisions,
            Data_export[line] : [n_comp, Q_comp, parametric_total_creep(data, n_comp, Q_comp)],
            line : line + 1
        )
    ),
    Data_export
) $

/* test: compute_parametric_n_Q_creep(Data_cleaned) $ */

/* write_data(test, "./org_cleaned_creep_para_lower.csv", 'semicolon); */

/* Create different creep-rate/time and creep/time plots. */
n_expo : 4.8 $
Creep_coefficient : 38.8 $
Creep_rate_data : addcol(Data_cleaned, compute_creep_rate(Data_cleaned, Creep_coefficient*
    εdotsimple(σ, T, n_expo))) $
Creep_data : addcol(Creep_rate_data, compute_creep(Creep_rate_data)) $
write_data(Creep_data, "./org_cleaned_creep_n_4.8_38.8.csv", 'semicolon);

/* plot2d([[discrete, time, creep_rate], [discrete, time, accumulated_creep]], [title, concat("
    Creep and creep rate for element 61571 with stress exponent of ", n_expo)],
    [xlabel, "Time [s]"], logx, logy, [legend, "creep rate", "creep"],
    [gnuplot_term, tikz], [gnuplot_preamble, "set key ceter bottom"]); */;

/* plot2d([[discrete, time, creep_rate], [discrete, time, accumulated_creep]], [title, concat("
    Creep and creep rate for element 61571 with stress exponent of ", n_expo)],
    [xlabel, "Time [s]"], logx, [legend, "creep rate", "creep"]) $ */;

/* write_data(Creep_computed, "creep_modified.csv"); */;

/* args([transpose(col(Creep_computed, 1)),transpose(col(Creep_computed, 4))]); */;

/* x:makelist(col(Creep_computed, 1)); */;
```

Appendix D

Sustainable Development Goals (SDGs)

The UN created a list of 17 goals [44] in which it describes the objectives needed to have a fully sustainable and fair society. This project relates to the following goals:

Goal 7: Affordable and clean energy While still in development, fusion energy presents a complete change of paradigm in energy generation. Fusion energy has the possibility to become a large producer of energy that can be controlled and scaled to meet an ever changing demand, while generating minimal amounts of radiation. As it stands today, it could become one source of energy to transition away from carbon based fuels.

In the past few years, the investment in fusion energy has grown exponentially. This is mainly driven by investments in private ventures, which hope to capitalize from this emerging market. New fusion designs and techniques are also being proposed, further increasing innovation. Projects such as ITER hope to start producing net energy output at the plasma level starting in 2035. However, there is still a long road ahead before fusion energy becomes a stable and common method of energy generation. The final design for a reliable and efficient fusion reactor is still a topic under discussion, however, Tokamak-style reactors are the most promising ones.

The present project has helped to gain a better understanding of relevant material behavior for the fusion industry. Sources:

- FIA (Fusion Industry Association): *FIA 2022 report.* URL: `https://www.fusionindustryassociation.org/about-fusion-industry`
- MIT: *SPARC.* URL: `https://www.psfc.mit.edu/sparc`
- ITER: *Goals.* URL: `https://www.iter.org/sci/Goals`

Goal 9: Industry, innovation and infrastructure Fusion energy is one of the largest collaborative projects in human history since it started being researched in the middle of the 20th century. Since then, several reactors have been created and have pushed the limits of what prior models were capable of. Today, the largest reactor is being built in southern France, ITER. ITER is not only the reactor but also

the collaboration and organization between several countries, mainly: China, the European Union, India, Japan, Korea, Russia and the United States of America. It also includes several industry conglomerates and the top research centers in the world. To further enhance collaboration, knowledge dissemination and innovation, several research institutions are now following the Open Access model for publishing new information; such as EUROfusiona and the Max-Planck Institute für Plasmaphysik.

As indicated above, the private fusion industry is growing rapidly. This further enhances the collaboration between research centers and new startups while also providing more infrastructure for the development of new devices.

The present project has also been made possible by the collaboration of several institutions, such as EUROfusion, Max-Planck Institute für Plasmaphysik, ENEA, University of Surrey and commercial partners, such as A.L.M.T® and AT&M®.

Goal 13: Climate action One of the main goals of climate action is to reduce the emission of green house gases, a large sum of which, tend to be generated during the production of electric energy. Fusion energy does not emit green house gases and it is expected to generate electric energy by the year 2050, which is the goal of the DEMO project. This would help reduce the emissions produced by the ever growing demand of electric energy while maintaining control of the energy production. This last property, control over generation, has been one of the biggest issues of renewable sources of energy, as their production is subject to nature and cannot be scaled when there is more demand. Fusion energy could supplement renewable sources when they become unavailable.